

**THE EFFECT OF GRAVITY CONVECTION  
ON SEGREGATION AND  
MICROSTRUCTURE IN BINARY ALLOYS**

by

**Fariba Saadat**


A thesis submitted to the faculty of Graduate studies in partial fulfilment of the  
requirement for the degree of Master of Science

**Department of Mechanical Engineering**

**Metallurgical Science Laboratory**

Winnipeg, Manitoba

1990

 National Library  
of Canada

Bibliothèque nationale  
du Canada

Canadian Theses Service    Service des thèses canadiennes

Ottawa, Canada  
K1A 0N4

The author has granted an irrevocable non-exclusive licence allowing the National Library of Canada to reproduce, loan, distribute or sell copies of his/her thesis by any means and in any form or format, making this thesis available to interested persons.

L'auteur a accordé une licence irrévocable et non exclusive permettant à la Bibliothèque nationale du Canada de reproduire, prêter, distribuer ou vendre des copies de sa thèse de quelque manière et sous quelque forme que ce soit pour mettre des exemplaires de cette thèse à la disposition des personnes intéressées.

The author retains ownership of the copyright in his/her thesis. Neither the thesis nor substantial extracts from it may be printed or otherwise reproduced without his/her permission.

L'auteur conserve la propriété du droit d'auteur qui protège sa thèse. Ni la thèse ni des extraits substantiels de celle-ci ne doivent être imprimés ou autrement reproduits sans son autorisation.

ISBN 0-315-71869-2

Canada

THE EFFECT OF GRAVITY CONVECTION ON SEGREGATION  
AND MICROSTRUCTURE IN BINARY ALLOYS

BY

FARIBA SAADAT

A thesis submitted to the Faculty of Graduate Studies of  
the University of Manitoba in partial fulfillment of the requirements  
of the degree of

MASTER OF SCIENCE

© 1990

Permission has been granted to the LIBRARY OF THE UNIVERSITY OF MANITOBA to lend or sell copies of this thesis, to the NATIONAL LIBRARY OF CANADA to microfilm this thesis and to lend or sell copies of the film, and UNIVERSITY MICROFILMS to publish an abstract of this thesis.

The author reserves other publication rights, and neither the thesis nor extensive extracts from it may be printed or otherwise reproduced without the author's written permission.

## ACKNOWLEDGEMENT

At this time I would like to express my thanks to Dr. M. C. Chaturvedi, Dr. K. N. Tandon and Dr. J. R. Cahoon for their guidance and support throughout the course of this work. I wish to express my thanks for the invaluable technical assistance of Mr. John Van Dorp, Mr. Lincoln M. Oree, and Mr. Don Mardis. Also I would like to thank Mr. Horst Weiss for drafting of figures.

Special thanks to all my friends particularly Miss Xiao Huang for their contribution towards the completion of this work. Finally, I would like to thank my family for their encouragement and support.

## ABSTRACT

The effect of gravity convection on macrosegregation, microsegregation, dendrite arm spacing, and microstructure of binary alloys has been investigated by using a specially designed apparatus which can develop a directional solidification. Energy Dispersive Spectrum technique on Scanning Electron Microscope was used to chemically analyse large areas on cross sections of ingots (to determine macrosegregation). Various spots across the primary dendrite arm were also analysed for microsegregation. Primary and secondary arm spacings were determined by using image analyser. It was observed that changing the direction of gravity vector did not affect inverse segregation, microsegregation and microstructure of the Al-4%Cu alloy. High gravity affects the dendrite arm spacing but not macro and microsegregation. It also affects the interlamellar spacing of the eutectic particles in Al-4% Cu alloy. The ingots solidified in KC-135 flight did not show any inverse segregation, or any change in microsegregation and dendrite arm spacing by changing gravity, probably because of the small size and high cooling rate. However these ingots show a change of interphase spacing of the eutectic particles in high and low gravity.

# TABLE OF CONTENT

ACKNOWLEDGEMENT.....	ii
ABSTRACT.....	iii
TABLE OF CONTENT.....	iv
LIST OF FIGURES.....	vi
LIST OF TABLES.....	xii
CHAPTER 1 INTRODUCTION.....	1
CHAPTER II LITERATURE REVIEW.....	4
2-1 SOLIDIFICATION AND CRYSTAL GROWTH.....	4
2-1-1 BASIC CONCEPTS.....	4
2-1-2 SOLIDIFICATION OF ALLOYS.....	7
2-1-3 DENDRITIC GROWTH.....	11
2-2 SEGREGATION.....	13
2-2-1 MICROSEGREGATION.....	15
2-2-2 MACROSEGREGATION.....	22
2-2-2-1 NORMAL SEGREGATION.....	22
2-2-2-2 INVERSE SEGREGATION.....	23
2-2-2-3 GRAVITY SEGREGATION.....	27
2-2-3 OTHER TYPES OF SEGREGATION.....	28
2-3 EFFECT OF CONVECTION ON SEGREGATION.....	31
2-3-1 LOW GRAVITY EXPERIMENTS.....	34
2-4 DENDRITE SPACING.....	36
2-4-1 PRIMARY ARMS.....	40
2-4-2 SECONDARY ARM.....	41
2-4-3 EFFECT OF CONVECTION ON PRIMARY AND SECONDARY ARM SPACING OF DENDRITES.....	42
2-5 SCOPE OF THE WORK.....	42

CHAPTER III	EXPERIMENTAL TECHNIQUES AND PROCEDURE .....	47
3-1	PREPARATION OF ALLOYS .....	47
3-2	APPARATUS USED .....	47
3-3	TEST SPECIMENS.....	52
3-4	MACROSEGREGATION ANALYSIS .....	52
3-5	MICROSEGREGATION ANALYSIS OF AL-4%CU .....	53
3-6	MEASUREMENT OF PRIMARY AND SECONDARY ARM SPACINGS .....	54
3-7	KC-135 SAMPLES .....	54
CHAPTER IV	RESULTS .....	60
4-1	DENDRITIC STRUCTURE OF SOLIDIFIED ALLOYS.....	60
4-2	TEMPERATURE GRADIENTS AND COOLING RATES.....	67
4-3	MACROSEGREGATION ALONG SOLIDIFIED INGOT .....	67
4-3-1	AL-4%CU ALLOY .....	72
4-3-2	PB-15%SN ALLOY.....	77
4-3-3	SN-15%PB ALLOY.....	78
4-4	MICROSEGREGATION IN AL-4%CU ALLOY .....	85
4-5	PRIMARY AND SECONDARY ARM SPACINGS .....	85
4-6	KC-135 EXPERIMENTS.....	91
4-6-1	MACRO AND MICROSTRUCTURES .....	91
4-6-2	COOLING CURVE.....	98
4-6-3	MACROSEGREGATION.....	98
4-6-4	MICROSEGREGATION .....	99
4-6-5	DENDRITIC SPACINGS .....	103
CHAPTER V	DISCUSSION.....	106
5-1	INVERSE SEGREGATION ALONG INGOTS.....	106
5-2	PARAMETERS AFFECTING MICROSEGREGATION.....	107
5-3	THE EFFECT OF GRAVITY ON DENDRITIC ARM SPACINGS .....	117

5-4 VARIATION OF INTERLAMELLAR SPACING OF EUTECTIC PHASE .....	119
CHAPTER VI CONCLUSIONS.....	122
REFERENCE .....	124



## LIST OF FIGURES

Figure 2-1:	A single-phase region of a phase diagram showing the liquidus and the solidus lines [1].	9
Figure 2-2:	Constitutional supercooling diagram. The solute concentration profile in the liquid gives rise to the variation in the equilibrium freezing temperature, $T_f$ , of liquid near the interface. The actual temperature in liquid is given by line 1, and the slope of $T_f$ at the interface is given by line 2. A supercooled liquid exists in the shaded region [1].	9
Figure 2-3:	Basic solidification model for dendritic growth, in a binary alloy, under an imposed position thermal gradient in the liquid [12].	14
Figure 2-4:	Phase diagram for a binary alloy indicative the various components of the total tip undercooling and solute build-up [12].	14
Figure 2-5:	Weight percent nonequilibrium eutectic formed as a function of $\eta$ for several Al-Cu alloys with less copper than the solubility limit. Linear growth [14].	17
Figure 2-6:	Weight percent nonequilibrium eutectic formed as a function of $\eta$ for several Al-Cu alloys with less copper than the solubility limit. Parabolic growth [14].	17
Figure 2-7:	Effect of solid diffusion during solidification on composition distribution across dendrite arms. Al-4.5% Cu alloy, finite difference method [14].	18
Figure 2-8:	Schematic representation of a cellular array in a positive temperature gradient and of transverse concentration gradients in liquid behind the tip [19].	20
Figure 2-9:	Solid composition at the growing interface, $C_s^*$ , as a function of $f_s$ according to the present model [19].	20
Figure 2-10:	Parameters for calculating inverse segregation.	25
Figure 2-11:	Experimental values for chill-face segregation in the Al (rich)-Cu system.	29

Figure 2-12: Macrosegregation in unidirectional ingot, constant cross section, (a) movement of liquidus and solidus (eutectic) isotherms; (b) experimental and calculated composition  $\overline{C}_S$ , along the ingot length; (c) sketch of ingot [30]. 30

Figure 2-13: Situation analyzed: flat, parallel isotherms at an angle to the vertical [36]. 33

Figure 2-14: The effect of gravity on the velocity of interdendritic liquid in Al-4.5 wt percent Cu alloy [36].....35

Figure 2-15: The effect of gravity force on macrosegregation in Al-4.5 wt percent Cu alloy [36].....35

Figure 2-16: Copper concentration along the axis of the SPLAV samples [45]. .....37

Figure 2-17: Schematic representation of Model I for isothermal coarsening [48].....39

Figure 2-18: Schematic representation of Model II for isothermal coarsening [48].....39

Figure 2-19: Relationship between secondary dendrite arm spacing and local solidification time [15].....43

Figure 2-20: Directionally solidified PWA 1480 superalloy (growth rate: 8 mm / min) average primary dendrite spacing vs distance from melt interface (during lo-g KC-135 flight parabolas) [52]. .....46

Figure 3-1: Schematic of the apparatus made. ....48

Figure 3-2: Crucible assembly. ....49

Figure 3-3: Schematic of the centrifuge.....51

Figure 3-4: Typical spot analysis of each arm.....55

Figure 3-5: Typical cross section of ingot, etched by Keller's solution.....55

Figure 3-6: Front and top view of the test equipment used in KC-135 flight. ....57

Figure 3-7: Crucible assembly for KC-135 samples.....58

Figure 3-8: Cross section of KC-135 samples. It shows hexagonal array of primary arm centres.....59

Figure 4-1: longitudinal cross section of ingots solidified opposite to gravity; (a) Al-4%Cu, (b)Sn-15%Pb, (c) Pb-15%Sn. ....61

Figure 4-2: Microstructure of Al-4%Cu ingot, solidified opposite to gravity. Backscattered electron picture under SEM.....	62
Figure 4-3: Microstructure of Al-4%Cu ingot, solidified parallel to gravity. Backscattered electron picture under SEM.....	63
Figure 4-4: Microstructure of Al-4%Cu ingot, solidified in 15 times gravity. Backscattered electron picture under SEM.....	64
Figure 4-5: Microstructure of Pb-15%Sn ingots. (a) Dendritic structure in transverse cross section, (b) lead particles (dark) in the eutectic matrix. Sample is chemically polished by 75% acetic acid and 25% H <sub>2</sub> O <sub>2</sub> . ....	65
Figure 4-6: Microstructure of Sn-15%Pb ingots. Tin cells (lighter phase) surrounded by eutectic. ....	66
Figure 4-7: Cooling curves of Al-4% Cu samples solidified opposite to gravity, (OG), and parallel to gravity, (PG). ....	68
Figure 4-8: Cooling curve of Sn-15% Pb ingots, solidified opposite and parallel to gravity.....	69
Figure 4-9: Cooling curve of Pb-15% Sn ingots, solidified opposite and parallel to gravity.....	70
Figure 4-10: Cooling curve of Al 4%Cu ingot, solidified in 15 times gravity.....	71
Figure 4-11: Macroseggregation data for Al-4% Cu solidified opposite to gravity.....	74
Figure 4-12: Macroseggregation data for Al-4% Cu solidified parallel to gravity. ....	75
Figure 4-13: Macroseggregation data for Al-4% Cu solidified in high gravity.....	76
Figure 4-14: Macroseggregation data for Pb-15%Sn solidified opposite, (OG), and parallel, (PG), to gravity.....	79
Figure 4-15: Chill face segregation in Pb-15%Sn. Ingot is directionally solidified after mechanical mixing.....	80
Figure 4-16: Macroseggregation data for Sn-15%Pb solidified opposite, (OG), and parallel, (PG), to gravity.....	82

Figure 4-17: Inverse segregation in Pb-15%Sn. Ingot is directionally solidified after mechanical mixing.....	83
Figure 4-18: Gravity segregation in Sn-15%Pb. The molten ingot is quenched in iced brine.....	84
Figure 4-19: Microsegregation data of AC-OG ingot in three cross sections of 4, 12, and 18 mm from chill face.....	86
Figure 4-20: Microsegregation data of AC-PG ingot in three cross sections of 4, 12, and 18 mm from chill face.....	87
Figure 4-21: Microsegregation data of AC-15G ingot in three cross sections of 4, 12, and 18 mm from chill face.....	88
Figure 4-22: Longitudinal cross section of ingots solidified in, (a) zero,(b) unit and (c) 1.8 times gravity.....	92
Figure 4-23 :Microstructure of unit gravity ingot. Eutectic particles in the matrix of aluminium phase (dark phase). ....	93
Figure 4-24: Microstructure of high gravity ingot. Larger interlamellar spacing for eutectic particles is evident. ....	94
Figure 4-25: Microstructure of zero gravity ingot. Large interlamellar spacing in eutectic particles and some noneutectic $\theta$ phase is evident. ....	95
Figure 4-26: Eutectic particles with fine lamellar spacings in zero gravity ingot. Only a few percent of eutectic particles with fine spacing are present in this ingot.....	96
Figure 4-27: Cooling curve of KC-135 sample solidified in unit gravity. ....	97
Figure 4-28: Macrosegregation in the ingot solidified in zero gravity. ....	100
Figure 4-29: Macrosegregation in the ingot solidified in unit gravity.....	101
Figure 4-30: Macrosegregation in the ingot solidified in 1.8 times gravity. ....	102
Figure 4-31: Microsegregation in the ingots solidified in zero, 1.8, and unit gravity....	104
Figure 5-1: Observed inverse segregation in Al-4%Cu solidified parallel to gravity compared to theoretically calculated data.....	108

Figure 5-2: observed segregation of Sn-15% Pb compared to theoretically calculated data. Sample solidified (a) opposite to gravity, (b) parallel to gravity..... 109

Figure 5-3: Porosity and holes caused by fast cooling..... 111

Figure 5-4: Variation of calculated solute content with fraction of solid. .... 115

Figure 5-5: The minimum solute content of the solid phase calculated as a function of  $\eta$  for an Al-4.5% Cu alloy cooled to just above the eutectic, to just below the eutectic, and to room temperature. Finite difference method [14]. .... 116

## LIST OF TABLES

Table 2-1	Constants for the empirical Equation $\lambda_1 = kG_L^a R^{-b}$ , where $\lambda$ is expressed in $\mu\text{m}$ , $G_L$ in $^\circ\text{C}.\text{mm}^{-1}$ and $R$ in $\mu\text{m} / \text{S}^{-1}$ [49].....	40
Table 2-2:	The effect of low gravity on dendrite spacing [52].....	42
Table 4-1:	Cooling characteristics of ingots.....	72
Table 4-2:	Macrosegregation in Al-4% Cu ingots.....	73
Table 4-3:	Macrosegregation in Pb-15%Sn ingots.....	78
Table 4-4	Macrosegregation in Sn-15%Pb ingots.....	81
Table 4-5:	Minimum composition of dendrites. ....	89
Table 4-6:	Primary arm spacings.....	90
Table 4-7:	Secondary arm spacings.....	91
Table 4-8:	Macrosegregation data of KC-135 ingots. ....	99
Table 4-9:	Minimum composition of dendrites for KC-135 samples.....	103
Table 4-10:	Primary arm spacings of KC-135 ingots. ....	105
Table 4-11:	Secondary arm spacings in KC-135 ingots. ....	105
Table 5-1	Microsegregation, comparison of experimental and calculated values. ...	114
Table 5-2	Comparison of primary and secondary arm spacings.....	119

# CHAPTER I

## INTRODUCTION

It has been suggested that experiments dealing with the solidification of metallic alloys and composites under low gravity has a particular importance with respect to industrial applications, and it may lead to better understanding of solidification processes on earth and possible space manufacturing of materials with improved or new properties.

The main purpose of solidification experiments in microgravity is to increase the understanding of interactions between fluid mechanics and the liquid-solid phase transition. In order to study the contribution of single mechanisms to the overall heat and mass transport, separating gravity-induced transport mechanisms such as buoyancy, sedimentation and natural convection from gravity independent processes such as diffusion can be very helpful.

Since experiments under microgravity became possible, different research areas such as the effect of convection on the stability of solidification front and segregation, separation processes specially in the alloys with miscibility gap, containerless solidification to study nucleation phenomena have been established. Number of alloys have been studied to quantify macro- and micro-segregation.

In directional solidification the thermal gradient at the chill face decreases with higher convection. This results from the convective flow of hot liquid toward the solid- liquid interface that is compensated for by the flow of cold liquid away from the solidification interface. During alloy solidification at the growing interface solute of different intensity from the bulk liquid is often rejected. Under a gravitational field, this results in solutal convection when the solute has different density. So the buoyancy driven convection flow in the liquid perturbs the metal alloy solute concentration profile that controls the

segregation, microstructure and properties. This is specially important in the process of dendritic growth because macrosegregation and interdendritic microsegregation cause nonhomogeneous casting properties. The interdendritic mass transport also affects the primary and secondary arm spacings, since the concentration gradient in interdendritic liquid drives coarsening of dendrites.

The primary objective of this research was to study the effect of gravity driven convection on:

- Macrosegregation - inverse segregation of solute,
- Microsegregation - interdendritic segregation of solute,
- Microstructure - dendritic arm spacing.

To study the effect of gravity on the above parameters some ground based experiments were also performed. Ingots were solidified with the solidification direction parallel as well as antiparallel to (against) the gravity vector. Similar ingot were solidified in 15 times gravity in a centrifuge.

The Binary alloy systems chosen for evaluation were Al-4%Cu, Pb-15%Sn and Sn-15%Pb. The physical metallurgy of these alloys has been studied extensively in the past and some ground based data are also available.

Based on the scientific informations generated in this work, the apparatus and the system can be modified for experiments in a sounding rocket. The comparison of the ground based data and microgravity data should give very valuable information regarding the effect of gravity on segregation.

Similar comparison has been done in this work on the smaller ingots (with faster cooling rate) solidified in zero, 1.8 and unit gravity in KC-135 flight at Houston, Texas with the help of NASA and NRC. Approximately 20 seconds of zero gravity and 20



seconds of 1.8 gravity were available during each cycle. Since segregation increases with decreasing cooling rate, the experiments in sounding rocket can be more valuable to investigate the effect of gravity convection on the above parameters.

# CHAPTER II

## LITERATURE REVIEW

### 2-1 SOLIDIFICATION AND CRYSTAL GROWTH

Solidification is the transformation of molten liquid to solid and as in any other phase transformation involves crystallization. In alloys the uniformity of composition of the crystallizing solid differs from that of the liquid, so macro and micro-segregation accompany solidification.

#### 2-1-1 BASIC CONCEPTS

Principles of solidification have been extensively discussed in the literature by Perepezko, Loesoult, Trivedi and Kurz [1], Minkoff [2], Chalmers [3], Flemings [4] and Winegard [5]. Therefore, this section will cover only important basic concepts.

Solidification is a process that occurs by the nucleation and growth of a new solid phase. Thermodynamics predicts that at equilibrium, solidification is not possible. A temperature difference,  $\Delta T$ , from equilibrium must be present to have sufficient driving energy,  $\Delta G$ , to start solidification:

$$\Delta G = \frac{\Delta T \cdot \Delta H_f}{T_E} \quad (1)$$

where  $\Delta H_f$  is the enthalpy of fusion and  $T_E$  is the equilibrium temperature.

Nucleation during solidification is a thermally activated process involving a fluctuational growth in the sizes of clusters of solids. In homogeneous nucleation, in pure metals solid formation occurs without the involvement of any extraneous impurity atoms or

other surface sites in contact with the melt, and the critical size of nuclei,  $r^*$ , at which the activation energy barrier for nuclei is reached, is given by:

$$r^* = \frac{2\sigma T_{mp}}{\Delta H_f \Delta T} \quad (2)$$

where  $\sigma$  is the surface energy per unit area and  $T_{mp}$  is the melting point.

Large undercooling values are required for homogeneous nucleation. In most liquid metal systems, the liquid-solid transformation is generally nucleated heterogeneously. In heterogeneous nucleation foreign bodies such as impurity inclusions, oxide films or crucible walls act to promote crystallization by lowering the activation energy barrier for nucleation,  $\Delta G^*$ . The evaluation of  $\Delta G^*$  for heterogeneous nucleation yields [1]:

$$\begin{aligned} \Delta G^* (\text{het}) &= \frac{16\pi\sigma_{LS}^3}{3\Delta G_v^2} \left[ \frac{2-3\cos\theta+\cos^3\theta}{4} \right] = \\ &= \Delta G^* (\text{hom}) [f(\theta)] \end{aligned} \quad (3)$$

where  $\sigma_{LS}$  is surface energy between solid and liquid,  $\Delta G_v$  is the free energy change due to the formation of a volume of solid,  $\theta$  is the contact angle between the nucleus and the heterogeneous nucleation site. The barrier for homogeneous nucleation is modified by  $f(\theta)$ , the shape factor, during heterogeneous nucleation.

The solid/liquid interface is a region between two condensed phases in which interatomic cohesive energies are comparable. Physicists successfully correlate the sharpness of the solid/liquid interfaces of pure substances to a faceting factor  $F$ , which is defined as follows:

$$F = \frac{Z^*}{1-Z^*} \cdot \frac{A_m \sigma}{R \cdot T_f} \quad (4)$$

where  $z^*$  is the ratio between the number of near neighbour atoms in the plane of the interface and the total number of near neighbour atoms in the bulk,  $A_m$  is the area occupied by 1 mole at the interface,  $\sigma$  is the solid/liquid interfacial tension and  $T_f$  is the melting temperature.

Solidification can be described as a succession of atomic events that occur in series. The kinetics of continuous growth leads to the following estimate for the kinetic undercooling  $\Delta T_k$  in the case of pure substances[1]:

$$\Delta T_k = T_{fk} - T^* = \left(\frac{a}{D_L}\right) \left(\frac{RT_f}{\Delta S_f}\right) v \quad (5)$$

where  $T_{fk}$  is the equilibrium temperature,  $T^*$  is the actual temperature of the moving interface,  $D_L$  is the liquid diffusivity,  $a$  is the atomic distance between the crystallographic planes parallel to the interface, and  $v$  is the velocity of the interface.

Although the mean value of the kinetic undercooling is often negligible, the anisotropy of the faceting factor and the related anisotropy of the kinetic of the growth of metallic crystals from the melt are observable. For a given driving force, the growth velocity of the interfaces parallel to an atomically dense plane is smaller than any other growth velocity. For an FCC crystal, for example, the dense {111} planes will tend to spread laterally more or less rapidly and form pyramids that have four fold symmetry axes, that is <100> axes. The vertex of each pyramid will then move along a <100> axis during growth. Therefore, the well known fact that dendrite of cubic metals exhibit <100> axes, and branches is probably related to their slight growth anisotropies.

Departure from interface equilibrium during growth results not only in kinetic undercooling but also a dependence of the partition coefficient on velocity. The following functional form has been proposed to describe the effect of velocity on  $k_v$  where  $k < 1$ .

$$k_v = \frac{C_S^*}{C_L^*} = \frac{k + \left(\frac{a_0}{D_L}\right) \cdot v}{1 + \left(\frac{a_0}{D_L}\right) \cdot v} \quad (6)$$

where  $a_0$  is a length scale related to the interatomic distance, has an estimated value of 0.5-5.0 nm [1].

### 2-1-2 SOLIDIFICATION OF ALLOYS

In alloys, the solidification microstructure is controlled by two important factors, composition of the alloy and the heat flow condition. When the heterogeneous thermodynamic equilibrium between liquid and solid is achieved, most crystalline solid solutions contain a smaller amount of each solute than the related liquid solutions. Many of the most significant effects of solidification in alloys are related to the fact that the composition of the solid that is formed is different from that of the liquid immediately in contact and at or close to equilibrium with it. A convenient way of describing this difference is by means of the ratio of concentration of solute in the solid to that in the liquid in equilibrium with it. This is called the equilibrium distribution coefficient (or equilibrium partition ratio),  $k$ , and is illustrated in figure (2-1). It is defined as follows:

$$K = \frac{C_S}{C_L} \quad (7)$$

where  $C_S$  and  $C_L$  are the solid and liquid concentration, respectively, in mutual equilibrium across a plane solid/liquid interface. Consider a single phase binary alloy, when an alloy of uniform composition,  $C_0$ , in figure (2-1) is cooled, solidification starts at the liquidus temperature  $T_L$ , if nucleation occurs readily. The first solid that forms at  $T_L$  has a composition,  $kC_0$ , which is lower than the liquid composition,  $C_0$ . Therefore, a solute rich layer will form at the interface. Further cooling results in an increase in liquid composition.

If the solute diffusion in the solid is not very rapid, solute segregation patterns will form in the solid.

The heat flow during solidification is very important in determining the microstructure of the cast alloy. For given temperature gradients and composition, four different interface morphologies can exist, depending on the growth velocity. Below a certain critical velocity,  $v_{cr}$ , a planar solid/liquid interface will be present. However, above,  $v_{cr}$ , the planar interface becomes unstable and forms a cellular, a cellular dendritic, or a dendritic interface.

Under steady state growth conditions, the interface temperature corresponds to the solidus temperature,  $T_S$ , in Figure (2-1). At this temperature, the interface composition in the liquid is  $C_0/k$ , which is larger (for  $k < 1$ ) than the liquid composition,  $C_0$ , far from the interface so that a solute-rich layer exists in the liquid ahead of the interface (Figure (2-2)). This liquid composition profile gives rise to a variation in the liquidus temperature with distance, as indicated by,  $T_L$ , in Figure(2-2). If the actual liquid temperature lies below the liquidus profile a region of supercooled liquid is present ahead of the interface. For a planar interface to be stable, the actual temperature gradient in the liquid must be equal to or larger than the gradient of the liquidus profile at the interface. This is called the constitutional supercooling criterion and requires

$$G_L \geq \frac{v\Delta T_0}{D} \quad (8)$$

where  $G_L$  is the thermal gradient,  $v$  is the interface velocity,  $D$  is the diffusion coefficient of solute in the liquid and  $\Delta T_0$  is the freezing range of the alloy, i.e.  $\Delta T_0 = T_L - T_S$ .

If the thermal gradient,  $G_L$ , is less than the value given by the criterion above, the planar interface becomes unstable. The temperature in the liquid falls below the liquidus temperatures in the solute enriched layer. Small perturbations at the planar interface will

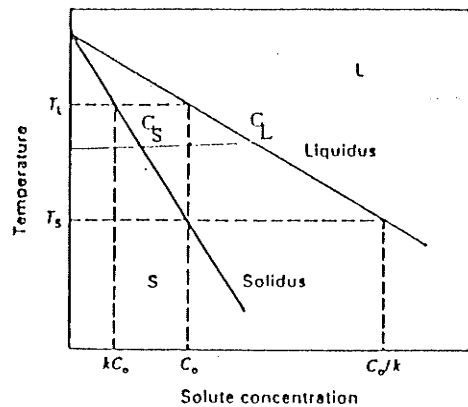


Figure 2-1: A single-phase region of a phase diagram showing the liquidus and the solidus lines [1].

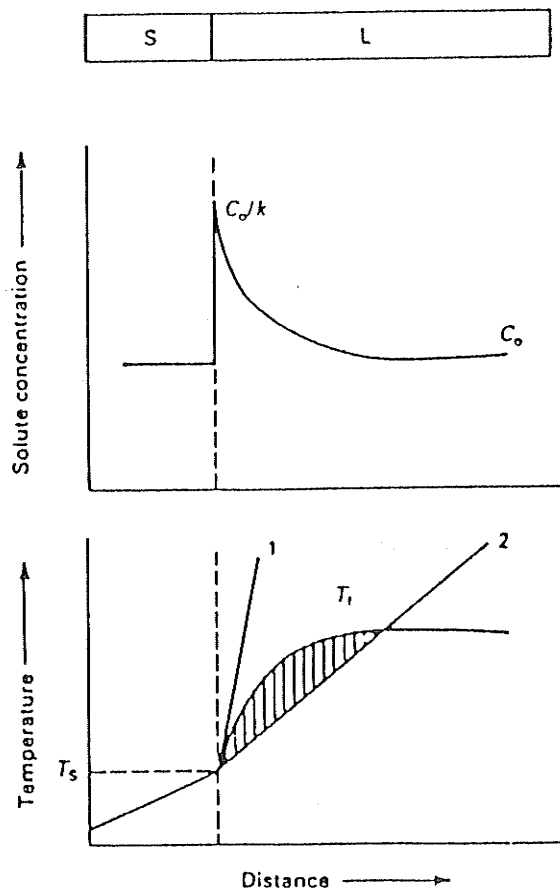


Figure 2-2: Constitutional supercooling diagram. The solute concentration profile in the liquid gives rise to the variation in the equilibrium freezing temperature,  $T_f$ , of liquid near the interface. The actual temperature in liquid is given by line 1, and the slope of  $T_f$  at the interface is given by line 2. A supercooled liquid exists in the shaded region [1].

now find themselves in a supercooled liquid and can grow in a stable fashion. As the thermal gradient,  $G_L$ , is decreased progressively, these perturbations or undulations give rise to cells and at high supercooling, the cells themselves become unstable and develop side branches thus becoming fully grown dendrites.

The formation of a cellular structure gives rise to solute segregation in the solid. The tip of the cell is at a higher temperature than the base of the cell. Thus, for  $k < 1$  the solid that forms at the cell tip will have a lower composition than the solid that forms at the cell base. This microsegregation profile is approximately characterized by the normal freezing or Scheil equation [6],

$$C_S = kC_0(1-f_S)^{k-1} \quad (9)$$

where,  $f_S$ , is the volume fraction of solid. Equation (9) is useful for nonequilibrium solidification when the phase diagram shows the presence of a higher composition second phase that can nucleate in the intercellular region. For example, for systems with eutectic phase diagrams, the maximum composition in the single phase corresponds to  $kC_E$ , where  $C_E$  is the eutectic composition. Thus once this composition is achieved the intercellular liquid will freeze with a eutectic structure. For this case equation (9) can be used to predict the volume fraction of the eutectic phase,  $f_E$ , where

$$f_E = \left(\frac{C_E}{C_0}\right)^{1/k-1} \quad (10)$$

In polyphase systems, because of simultaneous solidification of different phases, analysis of the solidification process is more complex. The principles that govern polyphase solidification have been investigated almost extensively with binary systems.

In alloys of eutectic composition both phases grow simultaneously, and each lamella has its own solid-liquid interface. The liquid in front of each lamella becomes enriched in



the major component of the neighbouring lamella and transverse diffusion of both components must take place. If the liquid is exactly at the eutectic composition, there might be no diffusion of either component forward into the liquid.

In off-eutectic alloys, a single phase instability, i.e. solidification of one of the phases in the form of primary dendrites plus interdendritic eutectic, occurs. In this case one phase, for example  $\alpha$  phase, becomes more constitutionally undercooled because the liquidus temperature at that composition is much higher than the eutectic temperature.

### 2-1-3 DENDRITIC GROWTH

Dendritic solidification is characterized by a morphology resulting from the growth of long, thin spikes in specific crystallographic directions with regular branches in other equivalent directions. Branching occurs at a roughly regular spacing, smaller for each successive order of branching.

In pure metals, even a small positive temperature gradient in the liquid gives rise to directional solidification and results dendrite formation. In an alloy melt, on the other hand, dendritic growth occurs readily even with fairly steep positive temperature gradients in the liquid ahead of the tips. For heat flow conditions in which the solid grows in an undercooled melt, a dendritic structure is present.

Different theories on dendritic growth have been proposed and several reviews on the subject are available [7-13]. A great deal of effort has been devoted to experimental measurements on a low melting transparent, "plastic crystal", succinonitrile. Thus, morphological details such as dendritic tip radius and time dependent phenomenon such as side-branch formation, remelting of dendrite arms and coarsening kinetics have been studied by direct observation [8,9].

Figure (2-3) [12, 13] illustrates schematically the basic solidification model for dendritic growth under an imposed positive thermal gradient,  $G_L$ , for an alloy of composition,  $C_0$ . The dendrite tips are located at  $x=x_t$  and the tip temperature is  $T_L$ . The total undercooling at the tip is thus  $\Delta T=(T_L-T_0)$ . It should be noted that the liquid composition in equilibrium with the dendrite tip is  $C_t > C_0$ . The composition of the solid forming at the tips is  $kC_t > kC_0$ . The liquid plus solid region extends from  $x=x_E$  to  $x=x_t$ , (figure 2-3(b)). The temperature within the two phase region increases from  $T_E$  at the isotherm located at  $x=x_E$  (the dendrite root) to  $T_t$  at the isotherm located at  $x=x_t$  (the dendrite tip). In the fully solid region, the temperature decreases from  $T_E$ , the eutectic temperature, to some low temperature. Corresponding to the temperature gradient  $G_L$ . There is also a concentration gradient,  $G_L/m_L$  present in the interdendritic liquid, Figure 3(c), where  $m_L$  is the slope of the liquidus line. The composition of interdendritic liquid decreases from  $C_E$  at the dendrite root to  $C_t$  at the tips. The unknowns now are the exact values of  $T_t$  and  $C_t$  as a function of growth rate  $R$  and the imposed thermal gradient  $G_L$ . In other words, the total undercooling  $\Delta T$  at the dendrite tip should be calculated.

Figure (2-3) also shows that the total undercooling at the dendrite tip is composed of four separate undercoolings:

$$\Delta T = \Delta T_G + \Delta T_D + \Delta T_r = T_k \quad (11)$$

As discussed by Laxmanan [12],  $\Delta T_G$  arises because of the interdendritic concentration gradient,  $\Delta T_D$  and  $\Delta T_r$  arise from diffusional effects and the tip curvature effect respectively.  $\Delta T_k$  is the kinetic undercooling which is usually negligible.

The basic equation for tip undercooling,  $\Delta T$  obtained by Burden and Hunt [14] is:

$$\Delta T = \frac{D_L G_L}{R} + \frac{R m_L C_0 (k-1)}{D_L} r_t + \frac{2\gamma T_L}{\rho_s H r_t} \quad (12)$$

In Figure (2-4) the various degrees undercooling have been superimposed on a phase diagram. The liquid composition in equilibrium with the dendrite tip,  $C_t$  is located on the dotted liquidus line corresponding to a radius  $r_t$ .

This model essentially relates the growth of a single dendrite under the conditions of supercooling due to solute rejection by the solid into the liquid and the imposed positive temperature gradient. It also assumes a planar solid-liquid interface moving under a steady state condition. No fluid flow due to convection buoyancy or thermal gradients has been assumed. However, it has been partly successful in explaining microsegregation and macrosegregation in cast binary alloys.

## 2-2 SEGREGATION

Segregation is the result of the rejection of solute (or of solvent) at the interface during solidification. In alloys, the solidus and liquidus lines do not coincide except at congruent melting points and eutectics; so if an amount of liquid of uniform composition is solidified the composition of the solid is not uniform and the solid formed from a liquid is necessarily of different composition. Uniform composition results if the solidification occurs very slowly so that the equilibrium establishes between the solid and liquid at all times and the diffusion occurs in the solid. However, this is not the case in ordinary solidification and casting processes. The different types of segregation differ only in the direction, distance and extent of the motion of the solute.

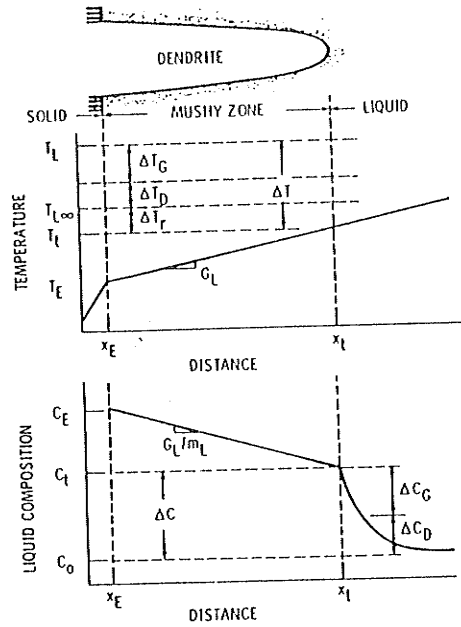


Figure 2-3: Basic solidification model for dendritic growth , in a binary alloy, under an imposed position thermal gradient in the liquid [12].

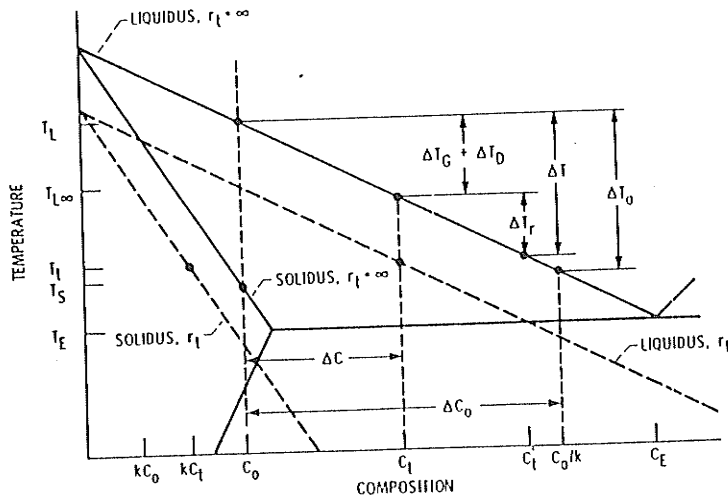


Figure 2-4: Phase diagram for a binary alloy indicative the various components of the total tip undercooling and solute build-up [12].

### 2-2-1 MICROSEGREGATION

The variable distribution of chemical composition on the microscopic level in a microstructure, such as dendrites and grains is referred to as microsegregation. The microsegregation is such that minimum solute concentration occurs at the centre of dendrite arms and maximum concentration occurs between dendrite arms. Equation (9) given in section 2-1-2 is a classical nonequilibrium solidification equation which is written for constant partition ratio. Assumptions used to derive this equation are: negligible undercooling before nucleation, no mass flow in or out of the volume element, complete diffusion in the liquid, no diffusion in the solid and constant  $k$ .

Brody and Flemings [15] considered the solid state diffusion (called "back diffusion") in the Scheil model and found the following expressions. For a linear rate of thickening of dendrite plates:

$$C_S^* = kC_0 \left(1 - \frac{f_S}{1 + \alpha k}\right)^{k-1} \quad (13)$$

and for parabolic thickening:

$$C_S^* = kC_0 [1 - (1 - 2\alpha k)f_S]^{[(k-1)/(1-2\alpha k)]} \quad (14)$$

where:  $\alpha = 4D_S\theta_f/\lambda^2$  and  $D_S$  is the solute diffusion coefficient in the solid,  $\theta_f$  is the local solidification time, and  $\lambda$  is the interdendritic spacing.

Equations (13) and (14) were used to compute the weight fraction of second phase formed in several Al-Cu alloys [15]. Results are plotted in Figures (2-5) and (2-6).  $\eta$  is solidification time and is defined by  $\theta_f / \lambda^2$ . Solute distribution is also obtained by Brody and Flemings [15] by using Fick's second law. Figure (2-7) shows the solute distribution in a Al-4.5 percent Cu alloy computed by them for a value of  $\eta=3.3 \times 10^8$  sec / cm<sup>2</sup>. The minimum copper concentration should increase during solidification from 0.61 (the value calculated from the phase diagram) to 1.4 percent. These analyses were compared with experiment in another paper by Bower, Brody and Flemings [15]. Minimum solute content at the centres of dendrite arms in Al-4.5 percent Cu alloy was found to vary from 1.3 to 2.2% depending on local solidification time and dendrite arm spacings. A correcting factor of 0.32 was used to match these minima with the theory.

The above equations, however, are not suitable for describing microsegregation with significant back diffusion; this is because they imply that  $C_S^*$  approaches  $kC_0$  as  $\alpha$  becomes large at any fraction solid  $f_S$ .

Clyne and Kurz [17] presented a modification to equation (13) and (14), in which the term  $\alpha$  is replaced by  $\alpha'$  given by the following expression for parabolic advance of the dendrite:

$$\alpha' = \alpha \left\{ 1 - \exp\left(-\frac{1}{\alpha}\right) \right\} - \frac{1}{2} \exp\left(-\frac{1}{2\alpha}\right) \quad (15)$$

Sarreal and Abbaschian [18] proposed a model for the calculation of eutectic fraction in rapidly solidified alloys. In this model the Burden and Hunt analysis [14] is combined with a model for eutectic growth undercooling. Based on the experimental data presented, Sarreal and Abbaschian offered a general analysis to interpret the results. Solid state back diffusion and in particular the analysis of Brody and Flemings and Clyne and Kurz [17] were quantitatively applied in order to explain the behaviour at relatively low cooling rates

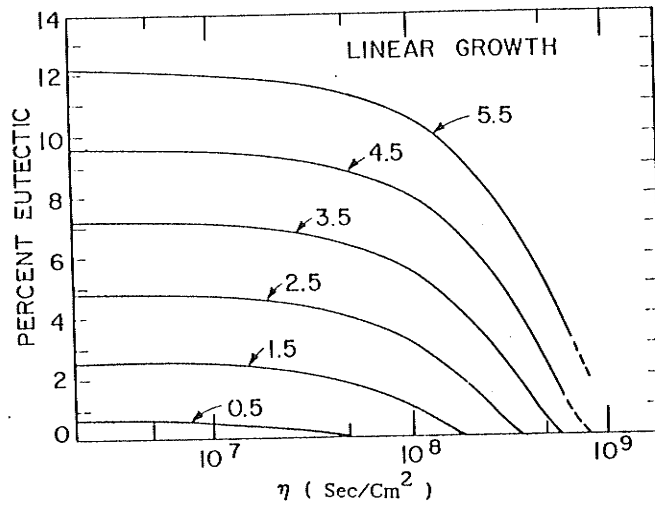


Figure 2-5: Weight percent nonequilibrium eutectic formed as a function of  $\eta$  for several Al-Cu alloys with less copper than the solubility limit. Linear growth [14].

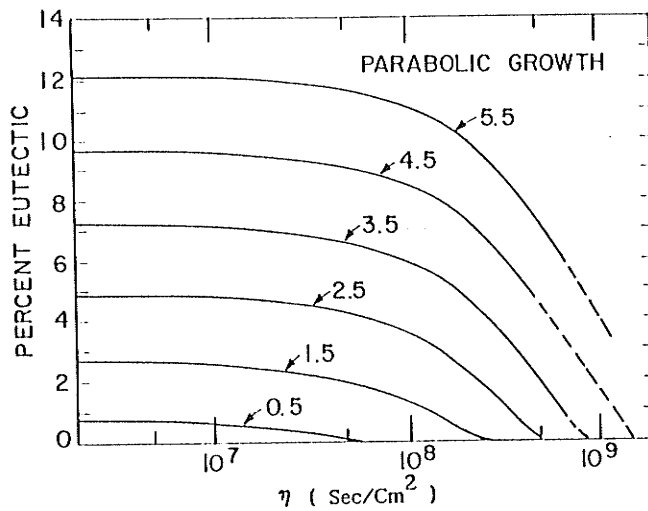


Figure 2-6: Weight percent nonequilibrium eutectic formed as a function of  $\eta$  for several Al-Cu alloys with less copper than the solubility limit. Parabolic growth [14].

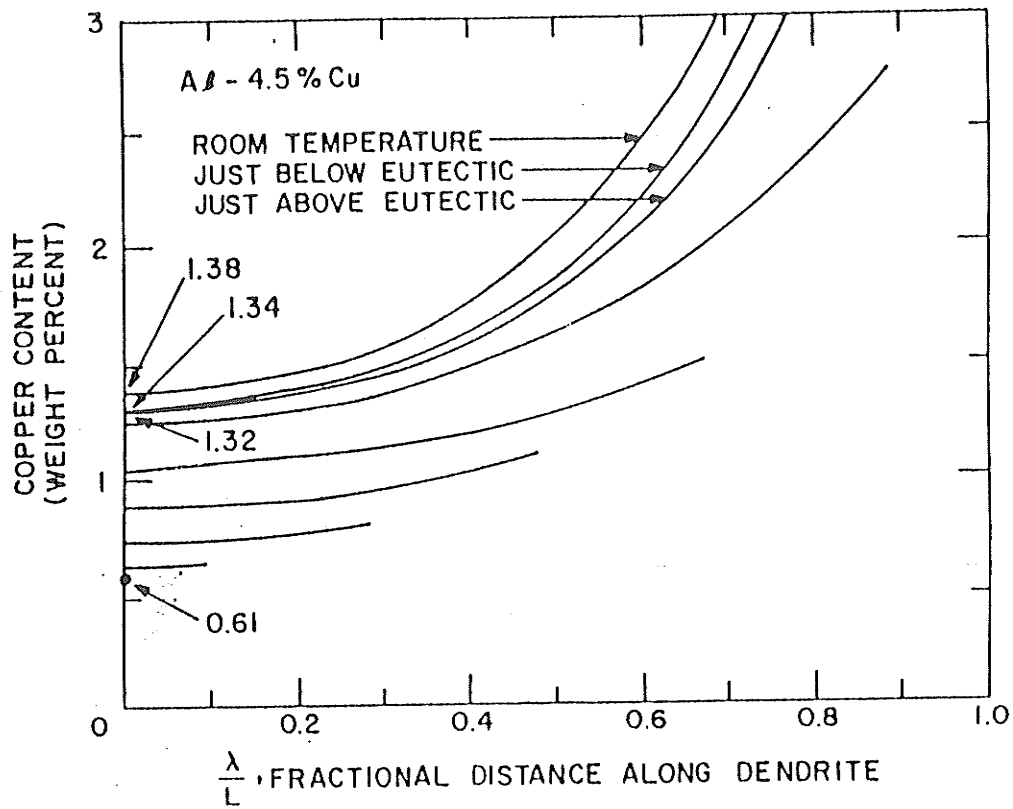


Figure 2-7: Effect of solid diffusion during solidification on composition distribution across dendrite arms. Al-4.5% Cu alloy, finite difference method [15].



(up to about 200K / s). At higher cooling rates, both dendrite tip undercooling and eutectic temperature depression were considered to describe the decrease in the severity of segregation with increasing cooling rates. The following equation was given which combines the effects of back diffusion, tip and eutectic temperature depressions at all cooling rates.

$$f_E^C = (1-f_S^0) \left[ \frac{C_{Sm}^{new} - 1}{kC_t} \right] \frac{2\alpha'k}{1-2\alpha'k} + \frac{1}{1-2\alpha'k} \left[ \frac{C_S^{max}}{kC_0} \right]^{\frac{1-2\alpha'k}{k-1}} - \left[ \frac{C_{sm}}{kC_0} \right]^{\frac{1}{k-1}} \quad (16)$$

where  $f_E^C$  is the eutectic fraction due to the combined effects,  $f_S^0 = (C_t - C_0) / C_t(1-k)$ ,  $\alpha'$  is given by equation 14, and  $C_{Sm}^{new} = ckC_t[f_E / (1-f_S^0)]$ .

Recently Giovanola and Kurz[19] proposed a model for the calculation of solid composition,  $C_S^*$ , at a growing interface. As shown in Figure (2-8), large concentration gradients exist in the tip region of the cellular or dendritic array [19, 20]. In the transient regime, the common assumption made in most of the above microsegregation models, complete mixing of liquid, is far from correct. However, the transverse concentration gradient, which can not be neglected near the tip, decreases when the diffusion fields of neighbouring cells or dendrites overlap extensively. Above a certain solid fraction,  $f_x$ , the assumption of complete mixing becomes reasonable.

The model is therefore composed of two parts (figure (2-9)). For solid fraction less than  $f_x$ , the relationship  $f_S(C_S^*)$  has been chosen so as to match at both ends; from  $f_S=0$  to  $f_S=f_x$ , the generally observed smooth increase in concentration with  $f_S$ , and for  $f_S > f_x$ , Scheil's equation. The simplest form satisfying these conditions is

$$f_S = aC_S^{*2} + a_2C_S^* + a_3 \quad (0 \leq f_S \leq f_x) \quad (17)$$

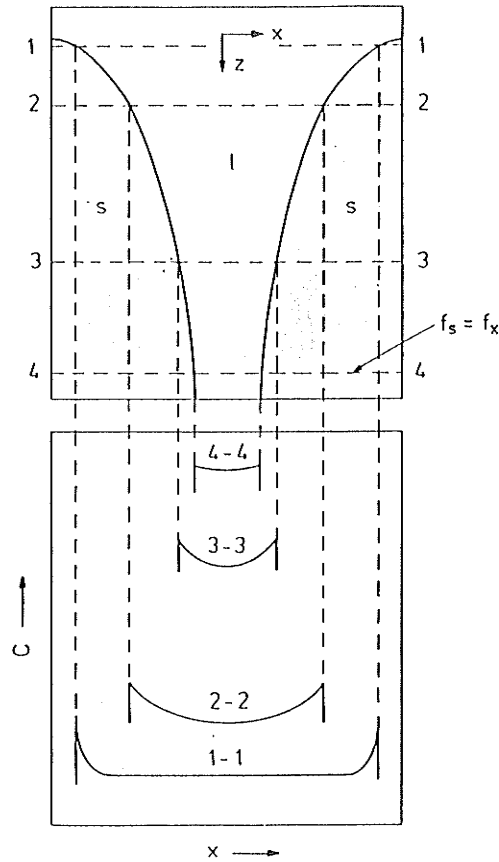


Figure 2-8: Schematic representation of a cellular array in a positive temperature gradient and of transverse concentration gradients in liquid behind the tip [19].

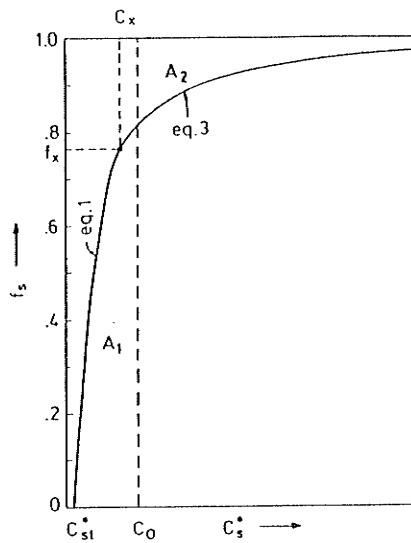


Figure 2-9: Solid composition at the growing interface,  $C_s^*$ , as a function of  $f_s$  according to the present model [19].

or

$$C_S^* = \frac{-a_2 + [a_2^2 + 4a_1(f_S - a_3)]^{1/2}}{2a_1} \quad (18)$$

where  $a_1$ ,  $a_2$  and  $a_3$  are unknown coefficients which have to be determined.

At large solid volume fraction, complete mixing exists. Since at high solidification rates, the concentration gradients in the solid decrease and back diffusion becomes less important, the Scheil equation can be used:

$$f_S = 1 + (f_x - 1) \left[ \frac{C_S^*}{C_x} \right]^{k-1} \quad (f_x \leq f_S \leq 1) \quad (19)$$

or

$$C_S^* = C_x \left[ \frac{1 - f_S}{1 - f_x} \right]^{k-1} \quad (20)$$

Now, there are two equations and five unknowns,  $C_x$ ,  $f_x$ ,  $a_1$ ,  $a_2$  and  $a_3$ . Calculation of these unknowns has been done by equating the concentration values and the slopes of both functions (17 and 19).

According to Giovanola and Kurz model [19] the concentration of the first solid to form is high; it undergoes little change up to high solid fractions and it increases in the last stage of solidification. Since in high velocities the concentration in the solid at the dendrite tip is larger (for  $k < 1$ ) than the equilibrium value  $kC_0$ , the last liquid to transform must have a reduced solute content in order to satisfy the mass balance. This is not considered by Schiel's or Brody and Flemings analysis, so the microscopic concentration profile in Giovanola and Kurz model is different from theirs and seems to agree more with experimental results.

## 2-2-2 MACROSEGREGATION

Macroseggregation is caused by the movement of liquid or solid, the chemical composition of which is different from the mean composition . The driving forces of the movement are: solidification contraction, effect of gravity or density differences caused by phase or compositional variations, external centrifugal or electromagnetic forces, formation of gas bubbles, deformation of solid phase due to thermal stress and static pressure and Capillary forces [1].

### 2-2-2-1 NORMAL SEGREGATION

The normal segregation of a solute can be represented by a single curve, relating the concentration of solute to the distance from the start of solidification. The form of this curve depends upon the equilibrium partition ratio  $k$ , the rate of solidification and the amount of mixing by fluid motion. When plane front solidification occurs, the solid composition of the initially solidified portion is low and has an approximate value of  $kC_0$ . As the solute is pushed ahead, because of diffusion, the solid composition gradually increases, resulting in a higher concentration at the finally solidified portion.

Considering a planar interface maintained at a low velocity ( $R$ ) of 1 or 2 centimetre per hour, and unidirectional solidification when  $k < 1$  and assuming no diffusion in solid. The solute distribution can be calculated from:

$$C_S = k_e C_0 (1 - f_S)^{k_e - 1} \quad (21)$$

where  $f_S$  is the fraction of volume solidified,  $C_S$  is the solute concentration in the solid at the solid-liquid interface, and  $k_e$  is the effective distribution coefficient which can be calculated from:

$$k_e = \frac{k_0}{k_0 + (1 - k_0)e^{-\Delta}} \quad (22)$$

where  $\Delta = R\delta / D$  is the thickness of the stagnant layer, and  $D$  is the diffusion coefficient in the liquid. For small values of growth rate,  $\delta$  depends on certain physical properties of the liquid phase [20].

### 2-2-2-2 INVERSE SEGREGATION

Inverse segregation occurs when a solute that is rejected during solidification is present at a higher concentration in regions that solidified earlier than those that solidified later. In other words, solute moves in a direction opposite to that of normal segregation.

For most alloys an overall contraction occurs on solidification, and this results in a positive segregation at the chill face of the ingot, i.e. the solute concentration is above the mean alloy concentration.

Scheil [6] was the first to describe precise analytical expressions. He developed an expression for the maximum segregation at the chill face as function of alloy composition and reported good order of magnitude agreement with experiments. This work was extended by Kirkaldy and Youdelis [22], Youdelis et al [23] and Flemings and Nereo [24].

For a typical binary eutectic alloy system, the solute concentration,  $C$ , is given by:

$$C = \frac{\frac{m_{LE}C_{LE}}{a_E} + m_{SE}C_{SE}}{\frac{m_{LE}}{a_E} + m_{SE}} \quad (23)$$

where  $m_{LE}$  and  $m_{SE}$  are the liquid and solid masses respectively in a representative volume just at the eutectic temperature,  $C_{LE}$  and  $C_{SE}$  are the mean solute concentrations in the liquid and cored crystal respectively,  $a_E$  is the eutectic contraction coefficient, defined as the specific volume ratio of eutectic liquid, i.e.

$$a_E = \frac{V_{SE}}{V_{LE}} \quad (24)$$

At concentrations other than eutectic,  $a$  is defined by:

$$a = \frac{V_S}{V_L} + \frac{C_L - C_S}{V_L} \cdot \frac{dV_L}{dC_L} \quad (25)$$

where  $C_S$  refers to the equilibrium solute concentration in the solid. The fundamental equation for calculation of the mass terms in equation (23) is:

$$\int_1^{m_B} \frac{dm_L}{m_L} = \int_{c_0}^{c_B} -\frac{K}{A} \frac{dC_L}{C_L} \quad (26)$$

where  $A$  is defined by  $C_L - C_S = AC_S$ . It is clear that  $A = 1 - k_0$ , where  $k_0$  is the equilibrium distribution coefficient. The value of  $K$  is calculated from:

$$K = a \left\{ 1 - \frac{1}{V_L m_L} \int_{m_L}^{m_L^* - m_{LE}} V'_L \left( \frac{1 - a'}{a'} \right) \frac{dm''_L}{dm'_L} dm'_L \right\} \quad (27)$$

$m_L^*$  is the composition of the liquid at the base of the dendrites and  $dm''_L / dm'_L$  is a contraction factor calculated from solidification parameters as illustrated in figure 2-10.

$$\int_0^{n_{SE}} \frac{dm_S}{m_S} = \int_1^{m_B} \frac{dm_L}{a} \quad (28)$$

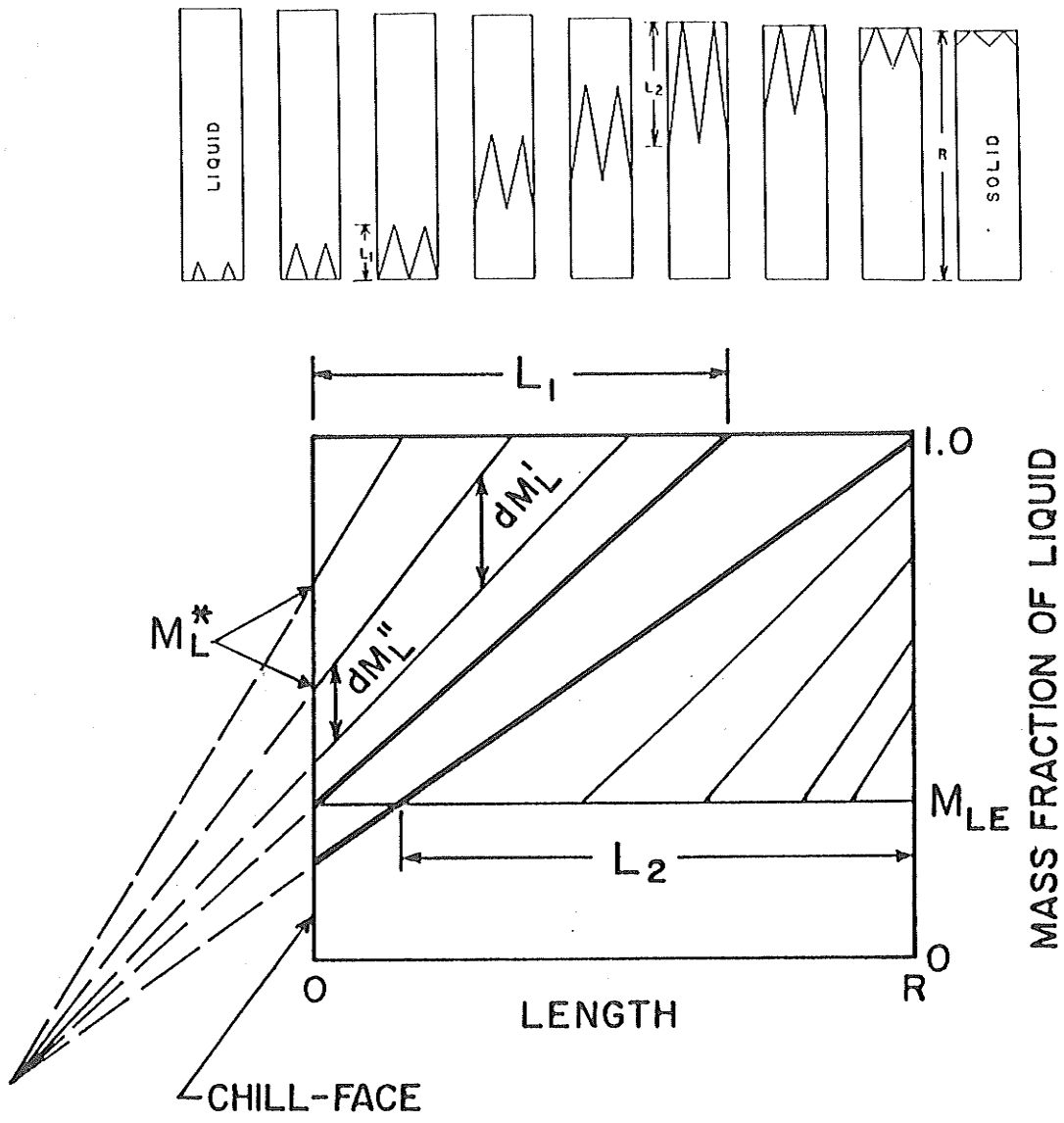


Figure 2-10: Parameters for calculating inverse segregation.

$$\int_1^{m_{SE}} CSdmS_S = \frac{K}{a} \left( \frac{1-A}{A} \right) \int_{c_0}^{c_{EB}} m_L C_L \quad (29)$$

The parameters  $a$ ,  $A$  and  $K$  are in general functions of  $C_L$ , and temperature so that a step-wise integration process must be performed.

The assumptions made in calculating the amount of segregation from equation (23) are: No surface exudation, no shrinkage porosity, no supercooling at solid/liquid interface, no mass transport in liquid (convective, diffusional, etc.) in the direction of solidification, no diffusion in solid and no concentration gradient in the liquid in the direction transverse to the direction of solidification.

The maximum segregation calculated as a function of alloy composition for different alloys shows a good agreement with experiments [22, 26]. Figure (2-11) shows experimental and theoretical curves of maximum segregation for Al-Cu system [27].

Another analytical expression was developed by Flemings et al [24, 29] to predict the effects of solidification variables on macrosegregation. This expression relates fraction liquid,  $g_L$ , to liquid composition,  $C_L$ , at a given position  $x, y, z$ , in a solidifying ingot, via the equation:

$$\frac{\partial g_L}{\partial C_L} = \left( \frac{1-\beta}{1-k} \right) \left( 1 + \frac{VVT}{\epsilon} \right) \frac{g_L}{C_L} \quad (30)$$

where  $\beta$  is the solidification shrinkage,  $k$  is the equilibrium distribution coefficient,  $V$  is the interdendritic flow velocity (vertical quantity),  $T$  is the temperature, and  $E$  is the rate of temperature change.

For unidirectional heat flow:



$$\frac{\partial g_L}{g_L} = \left(\frac{1-\beta}{1-k}\right) \left(1 + \frac{V_x G}{\epsilon}\right) \frac{\partial C_L}{C_L} \quad (31)$$

Equation (29) is written for the case of a planar isotherm moving perpendicular to the X-axis where  $x$  is the distance from the mold wall,  $\partial T / \partial y = \partial T / \partial z = 0$ ,  $\partial T / \partial x = G$  and  $V_x$  is the component of flow in the  $x$  direction.

Flemings and Nereo [30] have shown quantitative agreement of theory with experiment for a number of different types of ingot, using Al-4.75 Percent Cu. Figure (2-12) shows their experimental and calculated results for an ingot with a constant cross section.

The latter expression for macrosegregation was compared to the calculations done by Kirkaldy and Youdelis in a paper by Cahoon and Youdelis [31]. Computer programs have been developed by Cahoon and Youdelis [32] providing quick and accurate methods for the determination of theoretical maximum segregation in any binary-alloy systems, and also for the segregation distribution in any unidirectionally solidified binary alloy ingot.

### 2-2-2-3 GRAVITY SEGREGATION

Gravity segregation is caused by the settling or floating up of solid and liquid phases having a chemical composition difference (and therefore a density difference) from the mean value. For

example, the initially solidified phase of melted off dendrites could settle in the bottom of the casting if they are of higher density than the liquid.

During melting of an alloy containing a eutectic, the eutectic will melt first and run down to the bottom of the ingot. This segregation will persist after the entire alloy is molten.

To study the macrosegregation resulting from density differences in the liquid, a number of experiments have been done on lead-Tin alloys [23, 24].

In a recent work, Wang et al [34] have shown that in Pb-15%Sn the amount of gravity induced macrosegregation increases with decreasing dendrite growth rates and increasing thermal gradients. As the growth rates decrease, the local solidification time increases, which makes the dendrites coarse with higher permeability, so gravity induced convection takes place more easily and increases the macrosegregation.

Experiments done on Tin(rich)- lead ingot [34, 35] solidified (with a growth rate of 5.8-33  $\mu\text{m}/\text{sec}$ ) did not show significant macrosegregation.

### 2-2-3 OTHER TYPES OF SEGREGATION

Segregation may occur at grain boundaries during the process of solidification. When two crystals grow side by side, the boundary between them forms a groove which extends a distance of the order of  $10^{-3}$  cm behind the main interface.

Exudations are another type of segregation. If an alloy is solidifying and the solid metal contracts away from the chill, the latent heat of solidification may be sufficient to remelt some of the interdendritic eutectic. This eutectic is drawn via capillary action into the space between the metal and the chill resulting in a layer of eutectic on the surface.

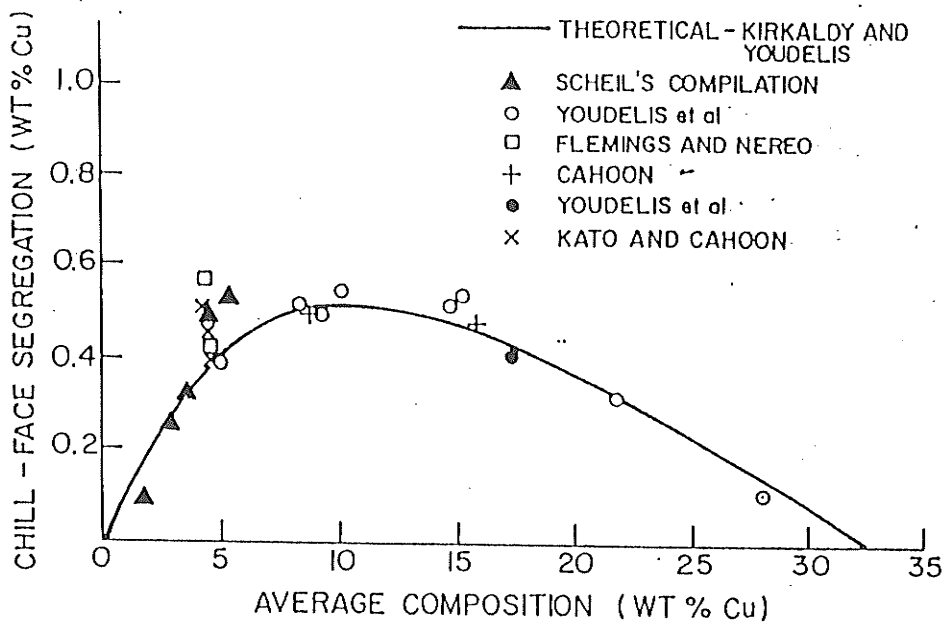


Figure 2-11: Experimental values for chill-face segregation in the Al (rich)-Cu system.

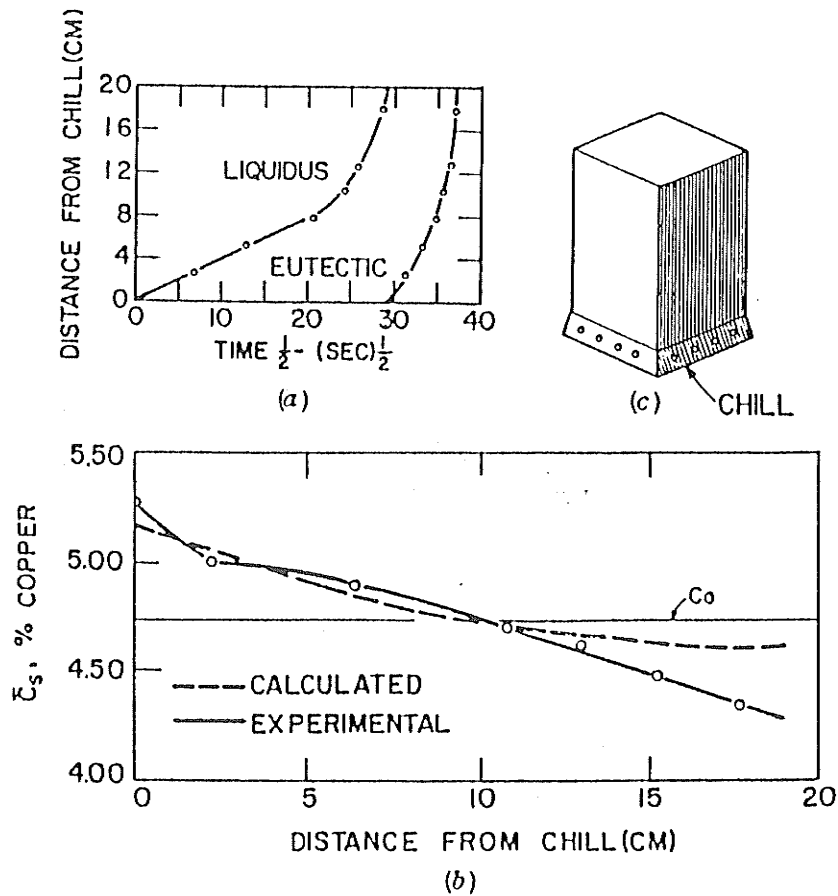


Figure 2-12: Macrosegregation in unidirectional ingot, constant cross section, (a) movement of liquidus and solidus (eutectic) isotherms; (b) experimental and calculated composition  $\bar{C}_S$ , along the ingot length; (c) sketch of ingot [30].

### 2-3 EFFECT OF CONVECTION ON SEGREGATION

During solidification, thermal gradients in the melt cause density gradients that under a gravitational field result in buoyancy driven convective flow.

The sensitivity of the melt thermal profile to convection is a function of the properties of the liquid. To determine this sensitivity, the Prandtl number,  $Pr$ , is used and is defined by:

$$Pr = \frac{\mu c_p}{k} \quad (32)$$

where  $\mu$  is viscosity,  $c_p$  is specific heat and  $k$  is thermal conductivity. At low values of  $Pr$ , thermal convection has less influence on the temperature field.

During alloy solidification, solute of different density from the bulk liquid is often rejected. If the solute is less dense than the liquid, solute convection results due to the gravitational field. For metallic systems, the contribution to the fluid flow by solute convection is normally large compared to the contribution by thermal convection. Gravity, therefore, has a strong effect on microsegregation, and macrosegregation.

In all of the models mentioned in section 2, the effects of convective flow have been ignored. Gravity-dependent interdendritic fluid flow has been modelled analytically and numerically by Mehrabian et al [35]. In this analysis they considered the hydrodynamics of interdendritic fluid flow as influenced by solidification contraction, liquid contraction during solidification, and gravity acting on a fluid of variable density. Principles of flow through porous media have been applied to the calculation. By considering a small volume element and applying the local solute redistribution equation (Eq (30), section 2-2-2-2), macrosegregation was calculated. They also presented the numerical solutions for horizontal, unidirectional, and steady state solidification. Simpson and Flemings [36] used

this analysis to illustrate the gravitational influence on interdendritic flow for a simple case shown in figure (2-13). Semi-infinite mushy zones whose isotherms were flat, parallel, and inclined at an angle to the force of gravity, were considered. Equations presented by Mehrabian et al [35] were simplified for this situation to:

$$\frac{\partial}{\partial t} [(\rho_L - \rho_S)f_L] = \frac{\partial}{\partial x_{\perp}} (\rho_L f_L v_{\perp}) \quad (33)$$

$$\frac{\partial f_L}{\partial t} = - \left( \frac{1-\beta}{1-k} \right) \frac{f_L}{C_L} \cdot \frac{\partial C_L}{\partial T} \left[ \frac{\partial T}{\partial t} + v_{\perp} \cdot \frac{\partial T}{\partial x_{\perp}} \right] \quad (34)$$

$$v = - \left( \frac{K}{\mu f_L} \right) [\nabla P - \rho_L g] \quad (35)$$

with the boundary condition

$$P = P_0 - \rho_L \cdot g \cdot x \quad (36)$$

where  $x_{\parallel}$  and  $x_{\perp}$  are the coordinate axes respectively parallel and perpendicular to isotherms.  $\rho_L$  and  $\rho_S$  are densities of liquid and solid,  $\mu$  is the liquid viscosity,  $\beta$  is the solidification shrinkage,  $C_L$  is the liquid composition,  $k$  is the partition ratio for the solute,  $g$  is the acceleration due to gravity,  $T$  is the temperature and  $K$  is the permeability. The unknowns are the volume fraction of liquid,  $f_L$ , the components  $v_{\parallel}$  and  $v_{\perp}$  of interdendritic velocity, and the pressure  $P$ . From equations (34) and (35),  $v_{\parallel}$  can be calculated as:

$$v_{\parallel} = \left( \frac{K g_{\parallel}}{\mu f_L} \right) [\rho_L(T) - \rho_L(T_L)] \quad (37)$$

where  $T_L$  is the liquidus temperature.

Equation(37) indicates that there are two ways to reduce flow parallel to isotherms and hence reduce segregation. First, if the isotherms are more nearly horizontal,  $g_{\parallel}$  and so  $v_{\parallel}$  will be reduced. Second, if the cooling rate on the thermal gradient in the mushy zone is

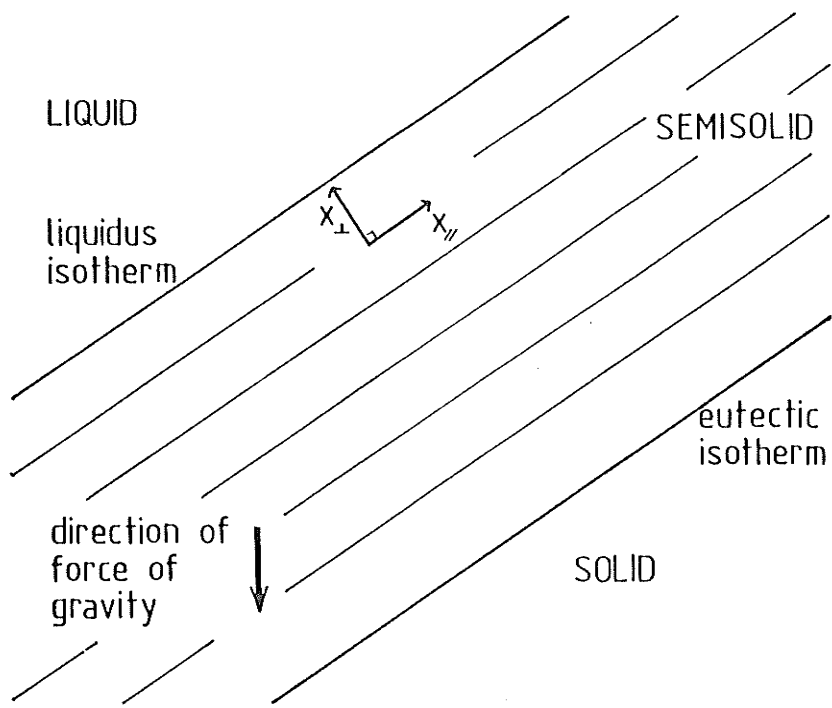


Figure 2-13: Situation analyzed: flat, parallel isotherms at an angle to the vertical [36].

increased the total flux of solute will be decreased. Since  $v_{11}$  is independent of the thermal gradient, increasing the thermal gradient will reduce the width of the mushy zone and thus the total flow parallel to isotherms (although the flow of solute per unit area normal to the isotherms will be the same). Increasing the cooling rate will reduce the time available for solute flow to occur and hence reduce the segregation [36].

The fact that macrosegregation increases with decreasing cooling rate has also been observed experimentally by other workers [35,37].

Based on the mathematical formulation given by Mehrabian et al [35], Maples and Poirier [36] described a model of a binary alloy solidifying horizontally by analysing the transients of the solid/liquid zone. They predicted the macrosegregation and flow field for Tin-lead, Aluminium-copper and Tin-Bismuth alloys. The effect of the gravity force on the solid/liquid zone of an Al-4.5 weight percent copper alloy is given in figures (2-14) and (2-15), With zero gravity, flow of the interdendritic liquid is due solely to solidification shrinkage and flow is exactly normal to the isotherms. Also, since the ingot solidified under steady state conditions, the composition from top to bottom is uniform and equal to the melt composition.

### 2-3-1 LOW GRAVITY EXPERIMENTS

Solidification on earth is always linked to complex interactions of gravity-induced and gravity-independent heat and mass transport processes. Under microgravity, buoyancy, sedimentation and natural convection do not exist or are strongly reduced. A microgravity environment, therefore, can be a helpful tool for experimental investigation of the effect of single transport mechanism on the growth morphology and for a better understanding of the role of fluid mechanics in solidification processes [38]. Some of the alloys solidified in



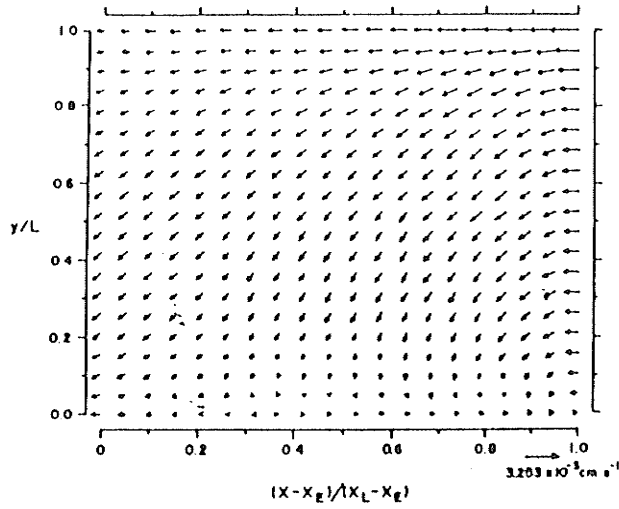


Figure 2-14: The effect of gravity on the velocity of interdendritic liquid in Al-4.5 wt percent Cu alloy [36].

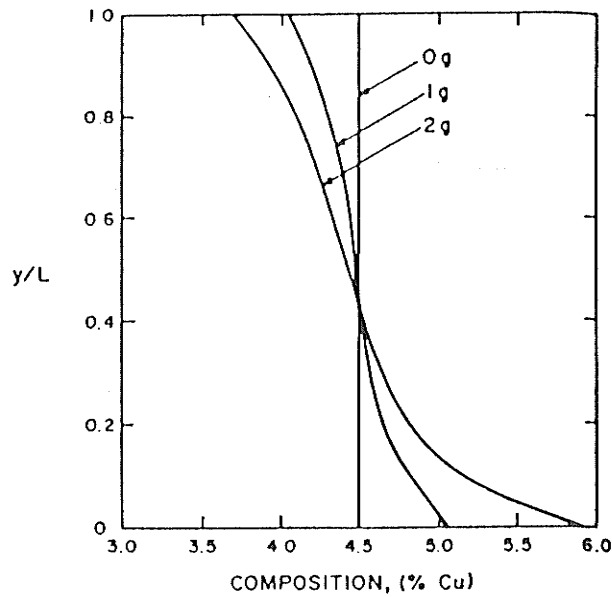


Figure 2-15: The effect of gravity force on macrosegregation in Al-4.5 wt percent Cu alloy [36].

low gravity environment have formed unique and often desirable microstructures [39-44], and number of alloys have been studied to quantify macro and microsegregation.

In a series of experiments performed by Favier et al [45] tin-lead and aluminium - copper alloys of different compositions were solidified aboard Salyout 6. Experiments in unit gravity on Al-0.4%Cu showed that the horizontally grown sample is cellular and the vertical one is dendritic, with the classical  $\langle 100 \rangle$  orientation of dendrites. The space grown sample exhibited three dendrites corresponding to the  $\langle 110 \rangle$  direction. Figure (2-16) illustrates the copper concentration measured along the axis of the Al-200 ppm Cu samples as a function of the length solidified. After the initial transient (1-2 cm) a constant concentration profile has been obtained, thus confirming the possibility of obtaining a pure, diffusion controlled region in space.

Al-0.3 weight percent copper and Al-7.0 percent silicon have been used by Tensi and Schmidt [46] to study diffusion in the melt ahead of the solidification front and the stability of a smooth solidification front. Results show that the thickness of diffusion layer in a microgravity sample is more than twice the layer thickness described in the unit gravity experiment. They also show that the criterion  $G/v$  for a smooth solidification front seems to have a term for thermal convection not considered in the past.

## 2-4 DENDRITE SPACING

Under directional solidification, if the supercooling ahead of the interface increases with distance, then any bump will see a larger supercooling and may grow. When the interface velocity exceeds the critical ( $v$  in equation 8, section 2-1-2) for the planar interface growth, depending on velocity a cellular or a dendritic structure forms. Dendritic structures are characterized by the formation of sidebranches. These sidebranches, as well as the

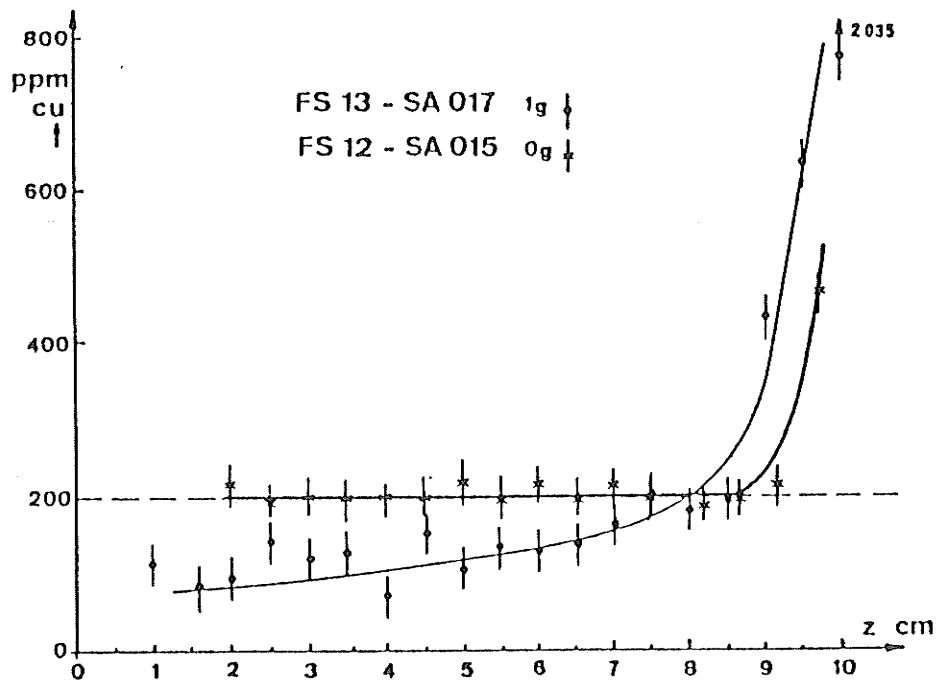


Figure 2-16: Copper concentration along the axis of the SPLAV samples [45].

primary dendrites, grow in a preferred crystallographic direction. The formation of secondary dendrite arms is clearly seen for a dendrite structure in a transparent alloy. A three dimensional view of dendrites in metals is difficult to observe because only parts of dendrites that intersect the plane of polish are visible.

Experiments performed on development of side-branches in succinonitrile [47] show that branching arises primarily from the slight anisotropy in the solid-liquid interfacial energy. The tip region, initially a body of revolution, bulges in the four longitudinal {100} planes and then distorts into branching sheets.

A convenient and widely used measure of the effects of solidification conditions on dendrite structure is dendrite arm spacing, i.e. the spacings between primary, secondary or higher order branches.

The dendritic structure which forms at the start of solidification is highly unstable. "Coarsening"(disappearance of small dendrite arms and growth of large dendrite arms) occurs rapidly both during isothermal holding and during solidification [48].

Two idealized models for coarsening have been suggested [48]. In the first model (Figure (2-17)) the radius of dendrite arms is considered to be constant (radius  $a$ ) except for one arm which is  $r_0$ , where  $r_0 < a$ . The melting point of the smaller arm is therefore less than that of the remaining arms, so it will disappear by transport of material from the smaller to the larger arm. In the second model (Figure (2-18)) a dendrite arm of radius  $a$  is considered. The root of the dendrite arm is of radius  $r_0$  where  $r_0 < a$ . This arm tends to melt off by transport of solid from the region of radius  $r_0$  to that of radius  $a$ . The driving force for the coarsening observed is the reduction of liquid-solid surface area.

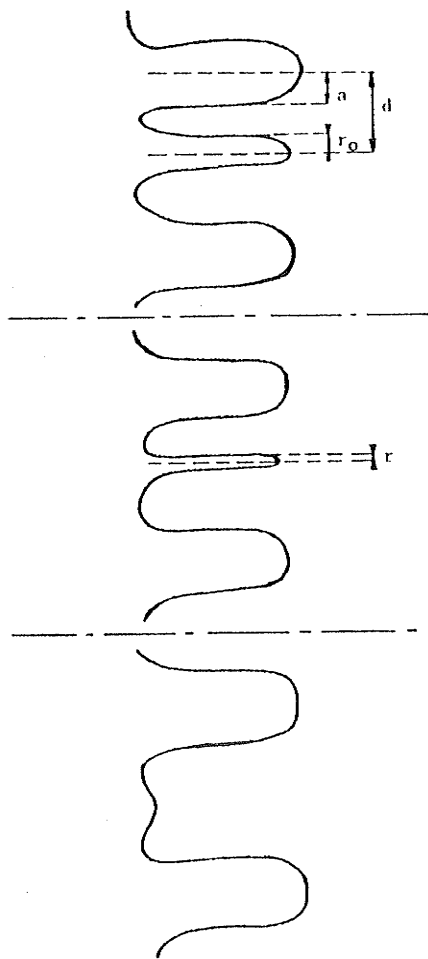


Figure 2-17: Schematic representation of Model I for isothermal coarsening [48].

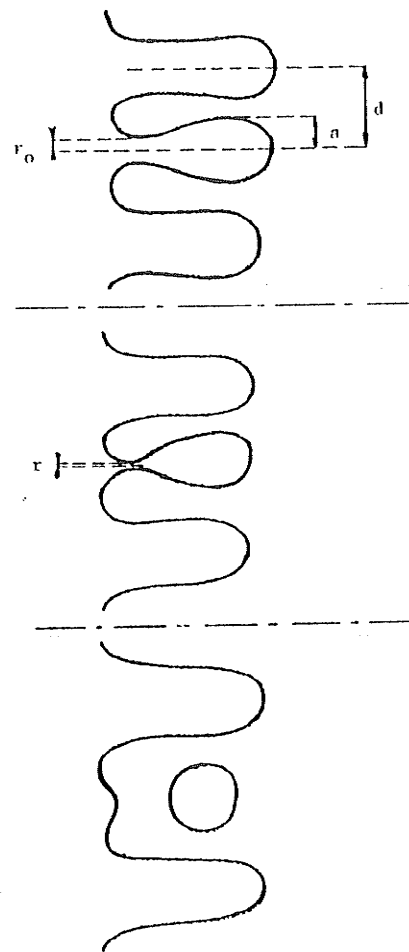


Figure 2-18: Schematic representation of Model II for isothermal coarsening [48].

### 2-4-1 PRIMARY ARMS

The primary arm spacing,  $\lambda_1$ , is described for each alloy by the empirical relation:

$$\lambda_1 = kG_L^{-a} R^{-b} \quad (38)$$

where  $G_L$  is temperature gradient,  $R$  is growth rate,  $k$  is a constant, and both  $a$  and  $b$  are close to  $1/2$ . This has been shown by Young and Kirkwood[49]. They have evaluated the constants for aluminium-copper alloys of 2.4, 4.4 and 10.1 percent copper, as listed in table 2-1. Young and Kirkwood also showed the invalidity of the Rohatgi and Adams [49] model which says the solidification rate is proportional to the cooling rate.

Table 2-1 Constants for the empirical Equation  $\lambda_1 = kG_L^{-a} R^{-b}$ , where  $\lambda$  is expressed in  $\mu\text{m}$ ,  $G_L$  in  $^{\circ}\text{C}.\text{mm}^{-1}$  and  $R$  in  $\mu\text{m} / \text{S}^{-1}$  [49]

wt percent Cu	a	b	k
2.4	0.50	0.50	$5.65 \times 10^3$
4.4	0.50	0.36	$3.05 \times 10^3$
10.1	0.50	0.43	$4.65 \times 10^3$

Increasing the solute content results a decrease in primary arm spacing [49, 50, 51].

Mc Cartney and Hunt [50] have shown that for dendrites in the Al-Mg-Si system:

$$\lambda = 272G_L^{-0.55} R^{-0.28} C_{\infty\text{Si}}^{+0.32} \quad (38)$$

where  $C_{\infty Si}$  is the atom fraction of Si in the alloy. They have also calculated the primary arm spacing relation for Al-6wt%Cu to be

$$\lambda = kG_L^{-0.55} R^{-0.28} \quad (39)$$

Experiments carried out by Klaren et al [51] on Pb-Sn and Pb-Au alloys have shown that the primary dendrite spacing follows equation(37) only at rates above  $45 \mu\text{m} / \text{s}$  in Pb-Sn alloys and above  $10 \mu\text{m} / \text{s}$  in Pb-Au alloys. Below these rates, the spacing becomes essentially constant with rate.

#### 2-4-2 SECONDARY ARM

Bower et al [15] gathered most of the data on secondary arm spacings available at the time for Al-4.5 wt percent Cu (figure (2-19)) and demonstrated that they could be represented by the relation:

$$\lambda_2 = \text{const.} \theta_f^{-0.39} \quad (40)$$

where  $\theta_f$  is the local solidification time in the ingot. It is evident from these data that the important solidification parameter affecting final secondary arm spacing is local solidification time.

Since coarsening of secondary arms occurs during solidification, it is found that the spacings obtained by quenching during solidification after time  $\theta$  from the onset of growth also fit the same equation if  $\theta$  is substituted for  $\theta_f$ .

### 2-4-3 EFFECT OF CONVECTION ON PRIMARY AND SECONDARY ARM SPACING OF DENDRITES

The results of low-gravity solidification studies on dendrite spacings are listed in Table 2-2 [52]. The effect of low gravity on secondary dendrite spacing was studied on sounding rockets (5min at 0.0001g) for ammonium chloride/water metal model material and for lead-tin binary alloy, and on parabolic aircraft manoeuvres for iron-carbon and MAR-M246 superalloy. Primary dendrite spacings have been studied by solidification in orbital laboratories for aluminium-copper and during parabolic aircraft manoeuvres for iron-carbon and PWA-1480 superalloy. In all studies, regardless of alloy complexity, low gravity solidification has resulted in coarser dendritic spacing compare to solidification in normal gravity.

Table 2-2: The effect of low gravity on dendrite spacing [52].

Composition	$g$ - $g_{low}$	Low gravity solidification Relative dendrite spacings
NH <sub>4</sub> Cl - 4%H <sub>2</sub> O	1-0.0001	+30pct sec., +10 pct tert
Al-Cu	1-0.00001	+150 pct. prim
Pb-Sn	1.8-0.01	+50 pct sec.
MAR-M246	1.8-0.01	+50 pct sec.
Fe-C- Si-P	1.8-0.01	+20 pct sec.
PWA-1480	1.8-0.01	+20 pct. prim.
Al-Cu	1-0.001	+500 pct prim.



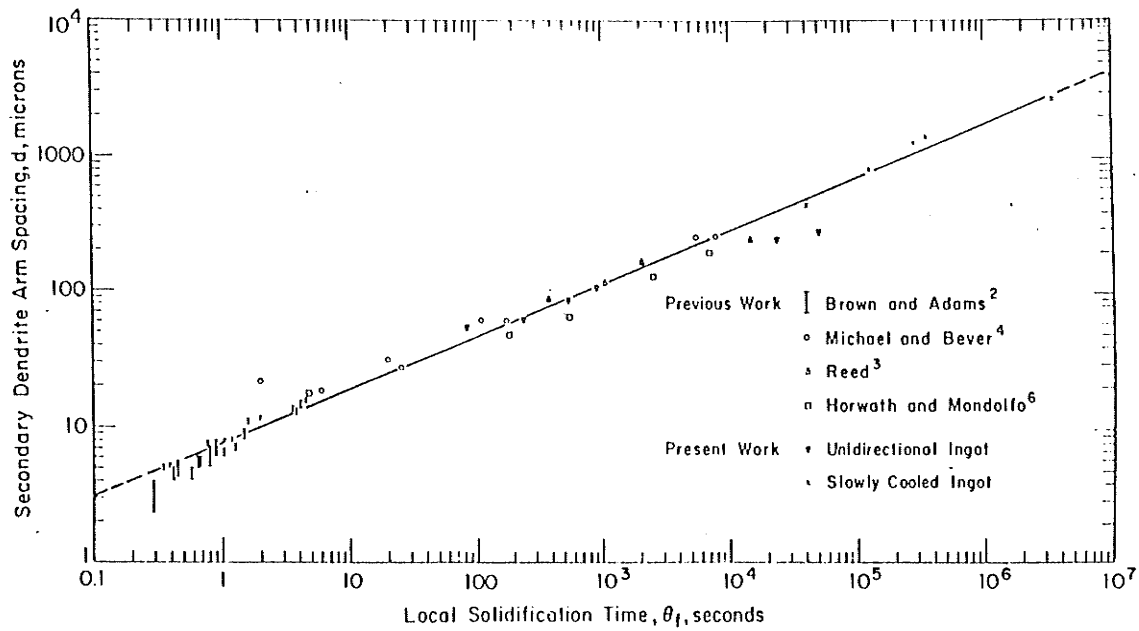


Figure 2-19: Relationship between secondary dendrite arm spacing and local solidification time [15].

Figure (2-20) gives the variation of primary arm spacing in a PWA 1480 superalloy during low gravity and high gravity KC-135 flight parabolas [54]. The arm spacings fluctuate with gravity force, increasing as the gravity level decreases, then growing finer as gravity becomes greater.

Convective flow of interdendritic fluid becomes less significant as gravity decreases; thus concentration gradients which drive coarsening (49, 50, 52) are increased. This produces larger arm spacings in low gravity in direct contrast to the lower gradients, slower coarsening rates, and therefore, smaller spacing in high gravity [54].

The dependence of dendrite coarsening rate on gravity level is dependent on the predominant coarsening mechanism. Zero gravity eliminates convective transport of interdendritic rejected solute. Increased average solute concentration, reduces dendrite curvature and therefore reduces dendrite coarsening by the arm coalescence model. However, thinning dendrite arms will cause increased coarsening with increase solute concentration for the arm melting model. Dendrite arm coarsening for Al-Cu alloy has been measured by interface quenching experiments in a orbital low gravity laboratory. Initial results show lower dendrite coarsening rate in low gravity. This indicates that arm coarsening for Al-Cu is primarily by coalescence.

## 2-5 SCOPE OF THE WORK

The review presented here shows that macro and micro-segregation occurs when an ingot solidifies unidirectionally and forms a dendritic structure also, the effect of buoyancy driven convective flow in the liquid on the alloy solute concentration profile is considered. Some analytical and experimental works have been done on the effect of low gravity on

macrosegregation as well as dendrite arm spacings, but not much work has been reported on microsegregation.

Most of the directional solidification experiments on the ground as well as in space have been conducted with a slow solidification rate for a thin long sample. Slow solidification rate results in appreciable diffusion in the solid which affects the concentration profile and makes it difficult to interpret the results of the experiment.

In this work an apparatus has been designed and built which is able to solidify the sample in a few minutes to minimize diffusion in the solid, and can be operated on inexpensive rocket flights for low gravity experiments. Structure, macro and micro-segregation have been studied for the case of solidification parallel to the direction of gravity as well as opposite to gravity and also in high gravity. The high gravity experiments were conducted on a simple centrifuge capable of generating 18 times gravity. This was also necessary to test the integrity of the crucible and chill block assembly against the 12-14 times gravity acceleration experienced by the sounding rockets.

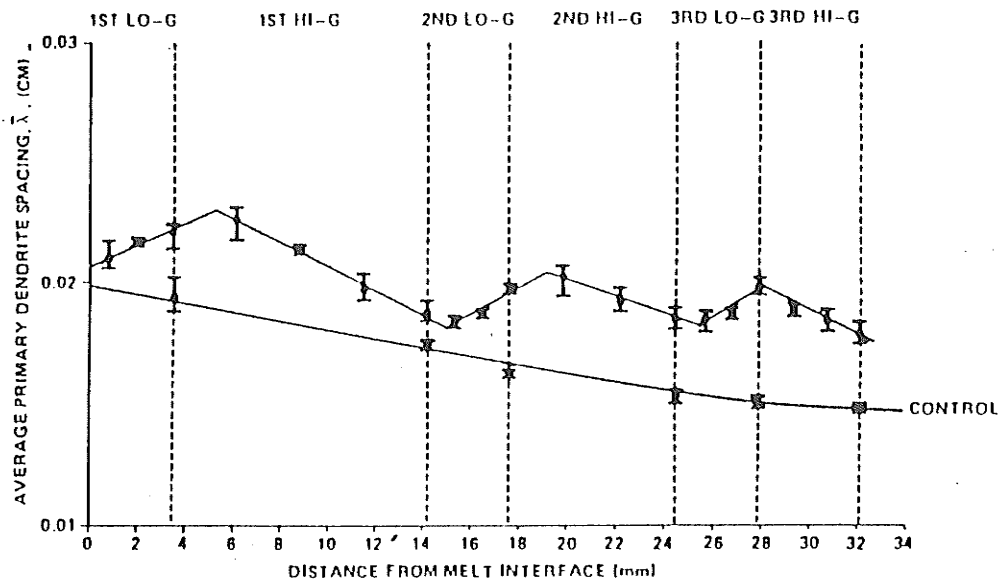


Figure 2-20: Directionally solidified PWA 1480 superalloy (growth rate: 8 mm / min) average primary dendrite spacing vs distance from melt interface (during log KC-135 flight parabolas) [52].

# CHAPTER III

## EXPERIMENTAL TECHNIQUES AND PROCEDURE

### 3-1 PREPARATION OF THE ALLOYS

Three master alloys of Al-4%Cu, Pb-15%Sn and Sn-15%Pb were prepared, The purity of alloying elements were:

Al-99.99%

Cu-99.95%

Pb-99.9995%

Sn-99.99%

The molten alloy was mechanically mixed by pouring the melt back and forth between the crucibles for a total of twelve times. Immediately prior to pouring, the alloy melt was degassed by bubbling with dry argon for one minute. Cylindrical specimens of 28 mm height and 15.9 mm diameter were machined from the master ingot.

### 3-2 APPARATUS USED

A special apparatus was designed which can be used for both ground based as well as microgravity based experimental work. It essentially consists of a crucible assembly enclosed in a stainless steel housing (Figure 3-1) suspended in a furnace, and a chill block located 2.5 centimetre from the end of the furnace, the melt is completely enclosed in a graphite crucible (Figure 3-2) which has a very thin bottom(0.5mm). One end of the melt is in contact with the thin graphite base where as the other end of the melt is in contact with a free moving graphite plug which applies a slight pressure from the graphite wool (due to

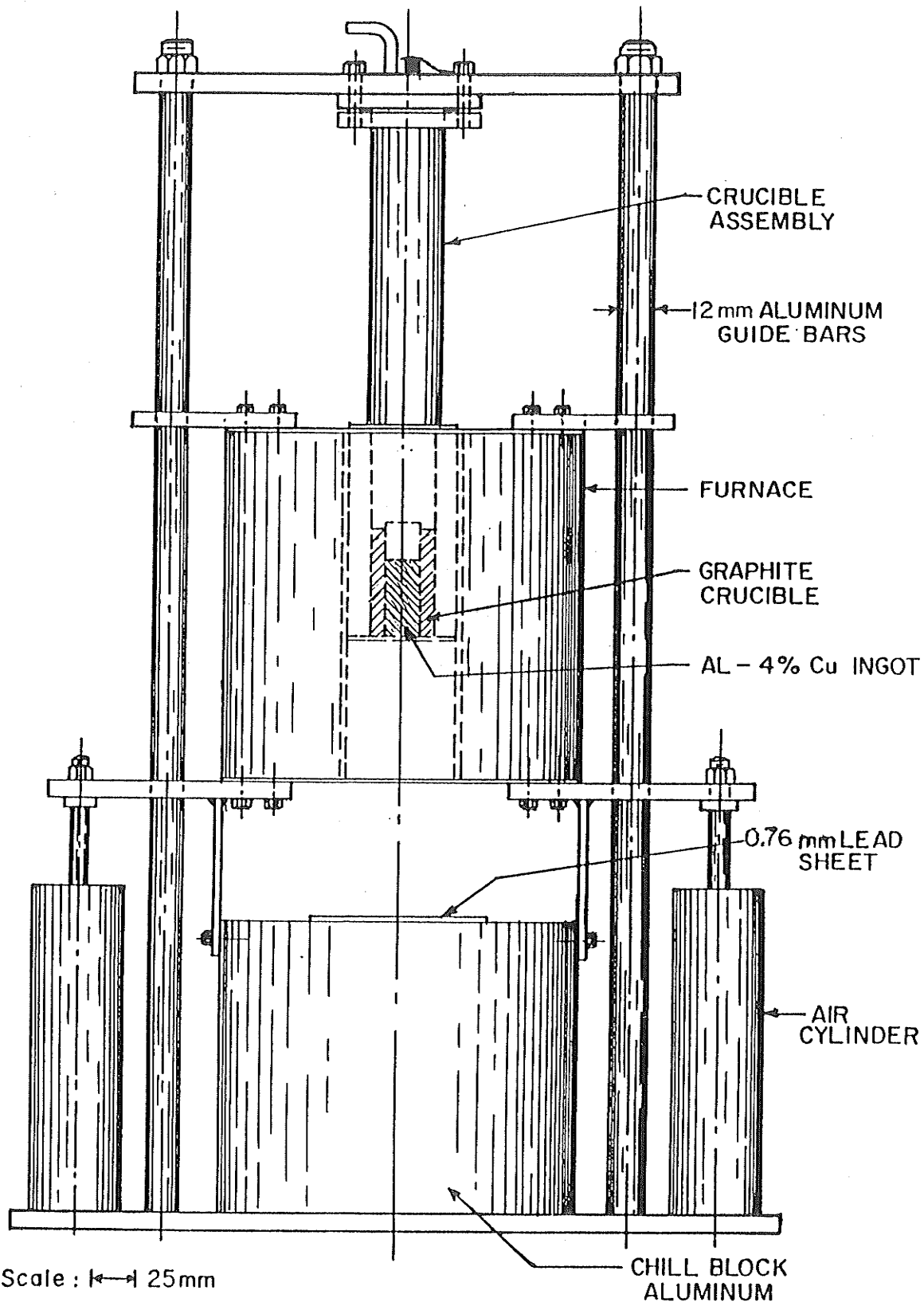


Figure 3-1: Schematic of the apparatus made.

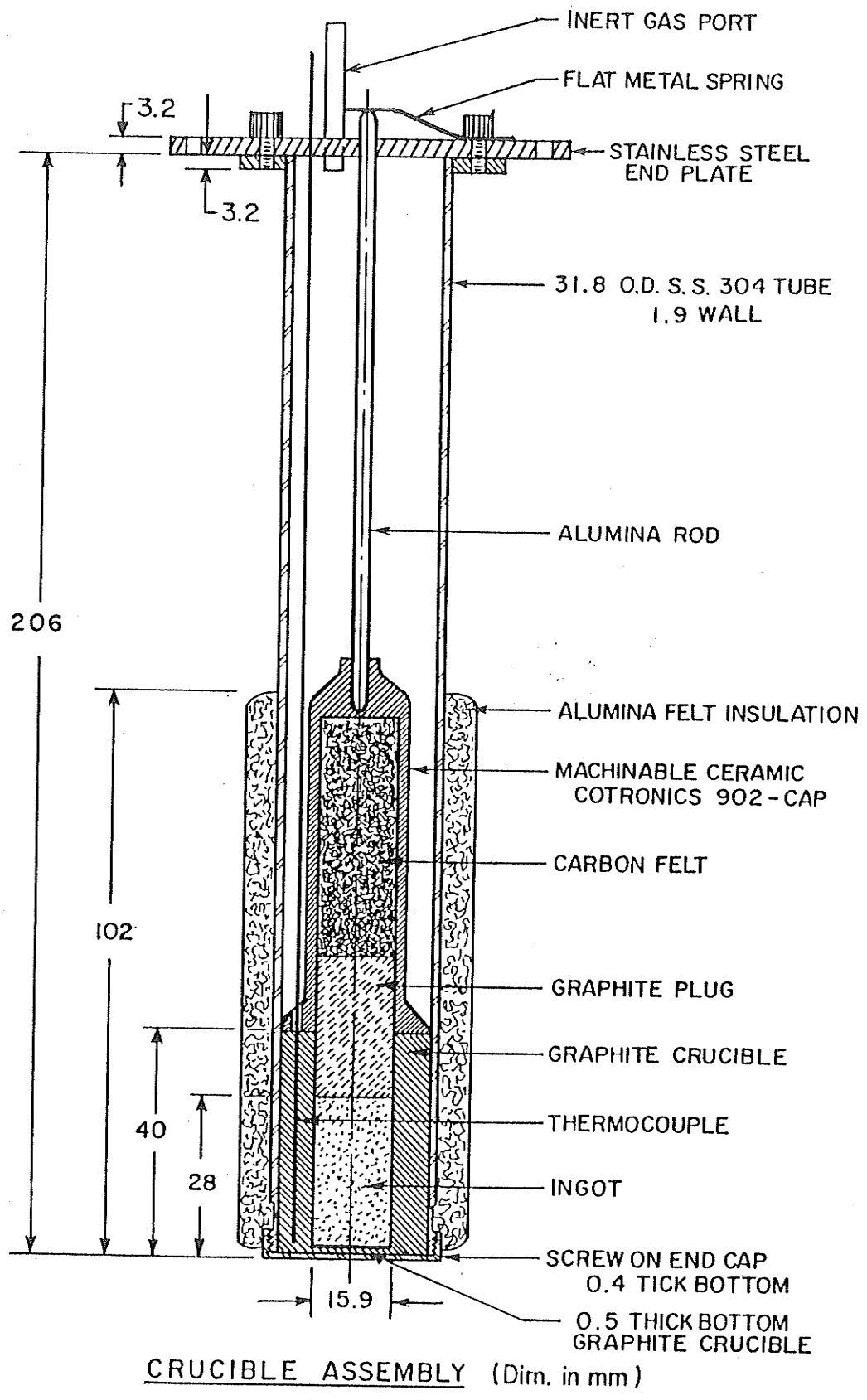


Figure 3-2: Crucible assembly.

its spring action). Four thermocouples are inserted at various heights in the graphite crucible to record the temperature of the melt. The graphite crucible is held in place against the bottom of the stainless steel housing with a ceramic cap and a rod under the spring load mechanism located on top of the cap.

The aluminium chill block assembly was mounted with the furnace (standard resistance wire with a temperature controller) which has sealing caps at the bottom opening. A thin layer (0.35 mm ) of solder (50 Pb-50Sn) sheet was fastened on top of the chill block. The solder sheet essentially provides chilling as well as an excellent contact between the crucible assembly and the aluminium block. In this case, the solidification front is moving against the gravity vector.

The whole assembly can also be inverted so that the chill block is on top and the chilling contact was made by moving the block furnace assembly down. Since the melt is completely enclosed and under pressure through the plug/wool, a good contact is always present between the melt and thin top of the crucible. In the inverted position the solidification front is moving parallel to the gravity vector.

For high gravity tests a simple centrifuge with an arm diameter of approximately 1.0 meter and capable of rotating at 200 rpm and generating close to 18g acceleration, has been fabricated (Figure 3-3). The crucible assembly containing the appropriate superheated molten alloy was placed into the centrifuge and then the unit was turned on. As soon as it reached its optimum velocity the chill block was moved into contact against the end of the crucible using a remote mechanism. This should produce directional solidification of the alloy in high gravity forces.



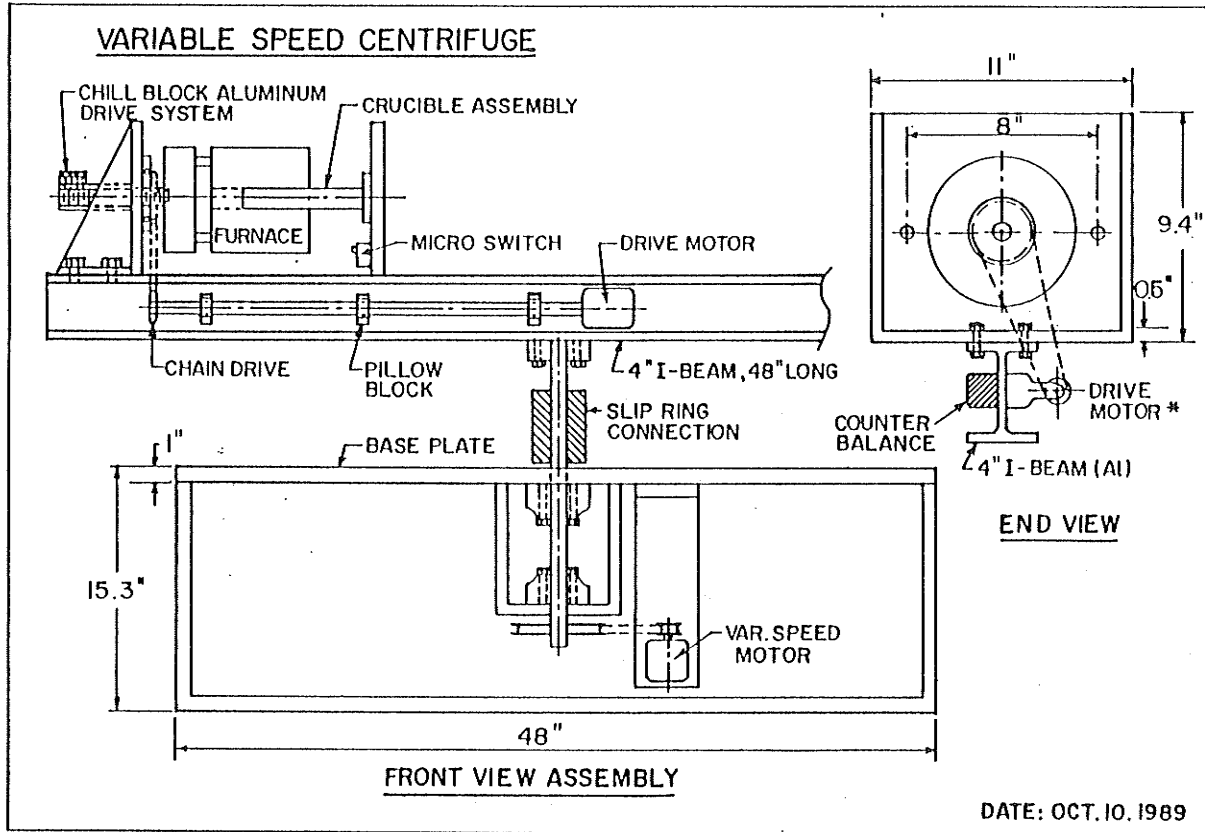


Figure 3-3: Schematic of the centrifuge.

### 3-3 TEST SPECIMENS

The following specimens have been prepared by using the above apparatus:

a) Al-4% Cu ingots solidified i) opposite to gravity ii) parallel to gravity and iii) in 15 times gravity.

b) Pb-15%Sn ingots solidified i) opposite to gravity ii) parallel to gravity and iii) after mechanical mixing.

The latter sample has been prepared by mechanical mixing of the melt in a graphite crucible separately from the present apparatus set up. After good mechanical mixing, The crucible was placed on top of the chill block and the sample solidified opposite to gravity.

c) Sn-15%Pb ingots solidified i) opposite to gravity ii) parallel to gravity , iii) after mechanical mixing, and iv)quenched after melting.

The latter sample has been prepared by using the apparatus set up. The melt was kept stationary for 30 minutes in a stainless steel crucible and then quenched in iced brine.

Longitudinal cross sections of all of the samples were examined for directional solidification.

### 3-4 MACROSEGREGATION ANALYSIS

Macrosegregation of solute elements (weight percentage) as a function of the distance from the chill face was determined using the energy dispersive spectrum (EDS) technique in a JEOL JXA-840 scanning microanalyser. Thin slices (2mm), sectioned from the Al-4%Cu ingots, using a diamond cut-off wheel were polished and subjected to EDS

analysis by exposing an area of 9.5 mmx7.5 mm on the disc. All analyses were carried out at 15KV with a fixed probe current of 600pA. A machine dead time of approximately 25% was maintained and the acquisition time was 480 seconds. Each slice was analysed six times and the results were averaged.

Pb-15%Sn and Sn-15%Pb samples were cut longitudinally. An area of 9.5mm x 2mm was exposed starting from the chill face and proceeding to the other end. The exposure time was 300 seconds and each area was analysed 3-5 times to get an accurate average concentration.

To confirm the data obtained by EDS analysis, two samples of the aluminium and lead alloys ingots were sliced and the copper or tin concentration in each slice was determined chemically using an inductively coupled plasma technique.

### 3-5 MICROSEGREGATION ANALYSIS OF AL-4%CU

Microsegregation of solute across a primary arm on the transverse cross section of the ingot was determined using EDS techniques in the scanning electron microscope.

The flat transverse faces of three slices from each ingot 4, 12, 18mm from the chill face were analysed. For each analysis, more than five spots (approximately 8 $\mu$ m from each other) between the two eutectic particles were analysed. Figure 3-4 shows typical spot analysis of each arm.

Microsegregation was determined for three Al-4%Cu samples solidified parallel to gravity, opposite to gravity and in the centrifuge under 15 times gravity.

### 3-6 MEASUREMENT OF PRIMARY AND SECONDARY ARM SPACINGS

In some metals, such as aluminium castings, it is difficult to measure dendrite arm spacings. In these metals, one can measure the dendrite cell size, which is the width of the individual cells or the dendrite cell interval, which is the centre to centre distance between adjacent cells [54].

Dendrite cell size for Al-4%Cu samples were determined by using a Leitz Tas Plus Image Analyser. Several micrographs (x50) were taken from the same slices used to measure microsegregation and have been traced on transparent sheets.

An area counting method was used to obtain a measure of the cell or dendrite primary spacings. A spacing parameter,  $\lambda$ , was calculated by counting the number of primary arm centres, N, and measuring the area, A, on all photographs of the same sample and setting.

$$\lambda = B \sqrt{\frac{A}{N}}$$

where B depends on the nature of primary arm centres array [49].

For Al-4%Cu ingots with dendritic structure as it is evident in Figure 3-5 the array is square, so B=1.

Longitudinal cross sections of samples were used to determine secondary arm spacings. Measurements were taken in up to 30 different fields for each sample.

### 3-7 KC-135 SAMPLES

Similar tests were done on special flights (KC-135) at Houston by using very small sample of Al-4%Cu, 6mm diameter and 5mm length.

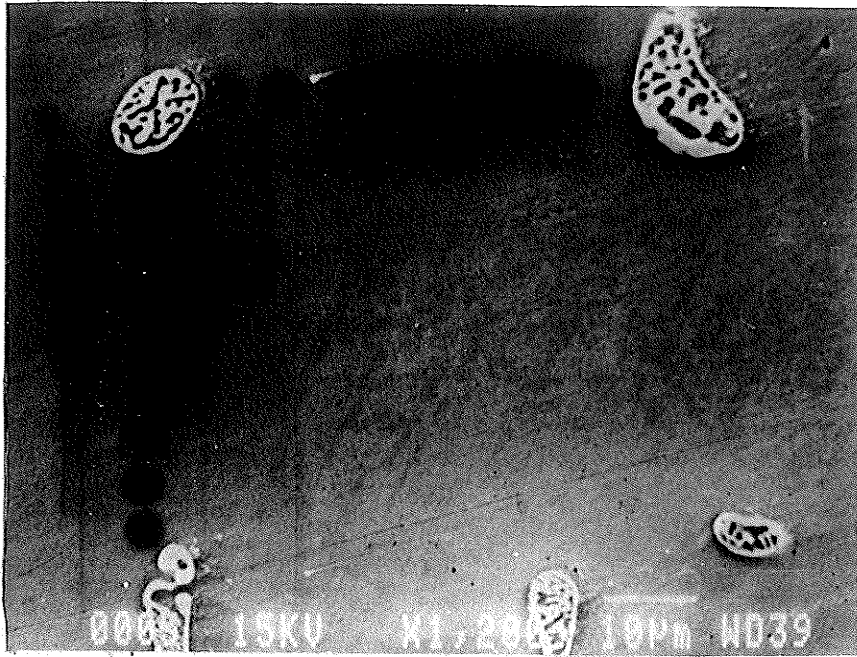


Figure 3-4: Typical spot analysis of each arm.

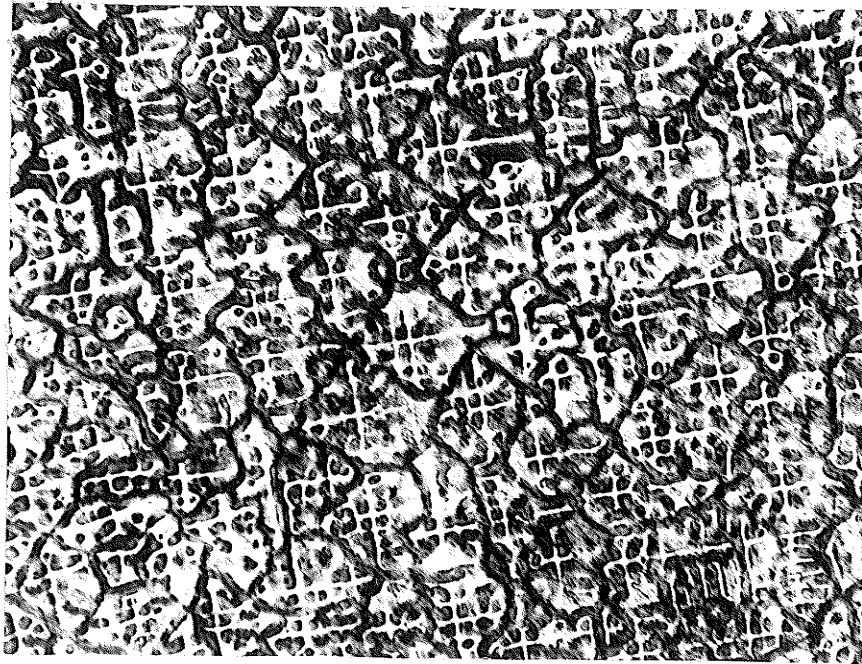


Figure 3-5: Typical cross section of ingot, etched by Keller's solution.

The top and front view of the test equipment and the crucible assembly are shown in Figures 3-6 and 3-7. The samples were placed inside a graphite crucible in the stainless steel container. The same system of carbon block and graphite wool was used to prevent the melt from floating away from the crucible during zero gravity and also to apply pressure to the fluid melt and attain a good contact with the chill block during solidification.

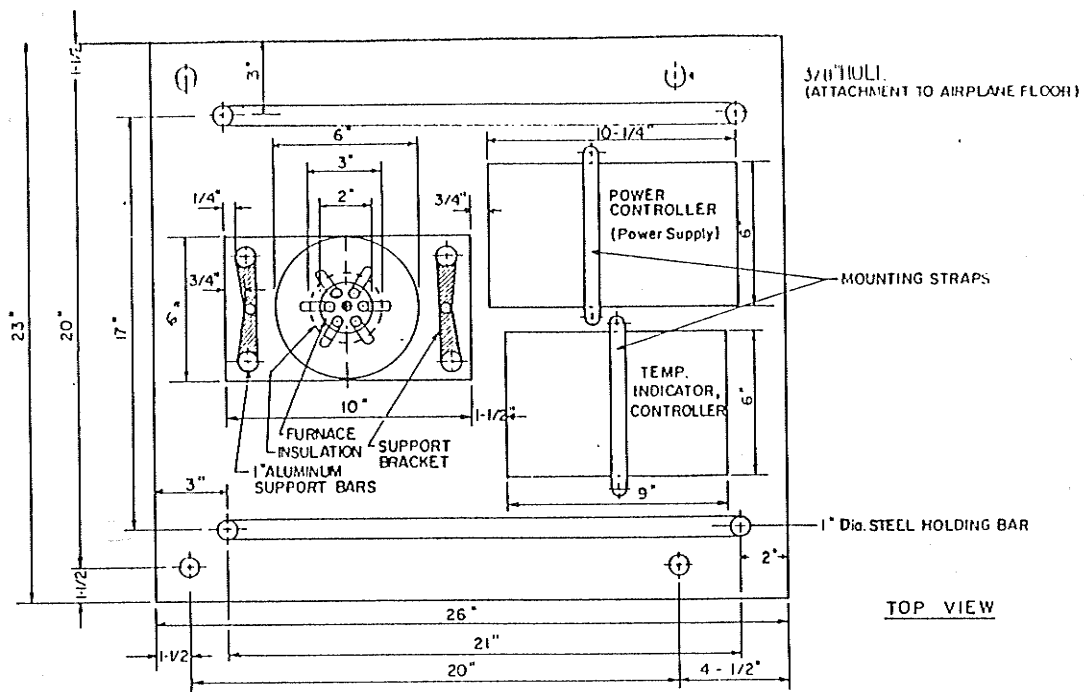
Approximately 20 seconds of zero gravity following by 20 seconds of 1.8 gravity were available during each cycle of KC-135 flight. Two set of samples were directionally solidified in low and high gravity periods. Similar tests were done on the ground in unit gravity.

Longitudinal cross sections of ingots were polished and analysed for macrosegregation. An area of 5mmx0.5mm was exposed starting from the chill face and proceeding to the other end. Other conditions for analysis were the same as the ones used for large samples.

Transverse faces of ingots were used for microsegregation analysis and primary arm spacing measurements, using the same techniques applied for large samples.

However to calculate the primary arm spacings by area counting method the factor B should be considered to be 1.075, because the primary arm centres array in this case is close to hexagonal (Figure 3-8).

Secondary arm spacings of dendrites in all three samples have been obtained on longitudinal cross sections by averaging the measurements for 20 fields.



FRONT VIEW

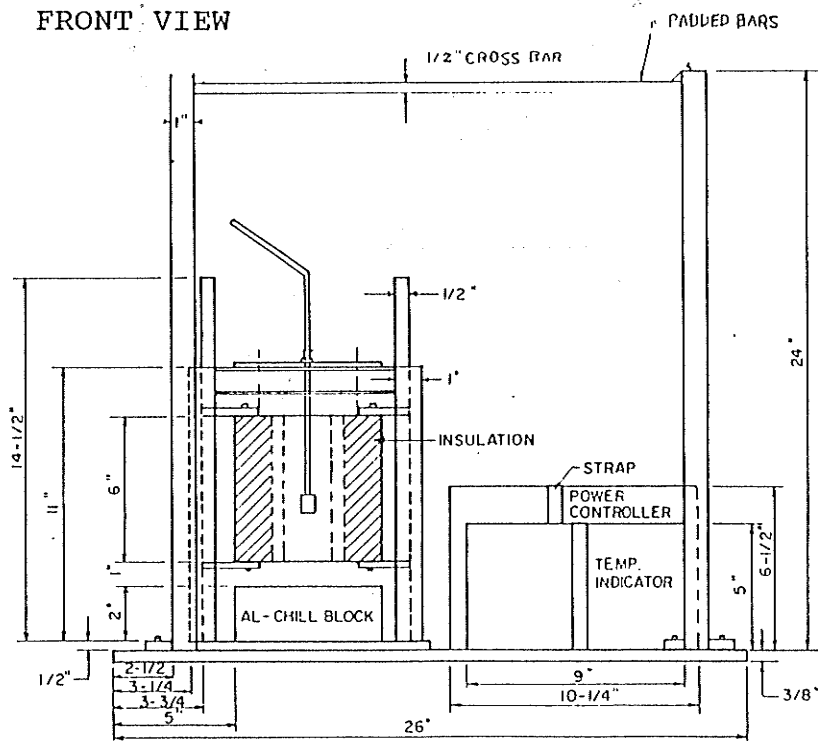


Figure 3-6: Front and top view of the test equipment used in KC-135 flight.

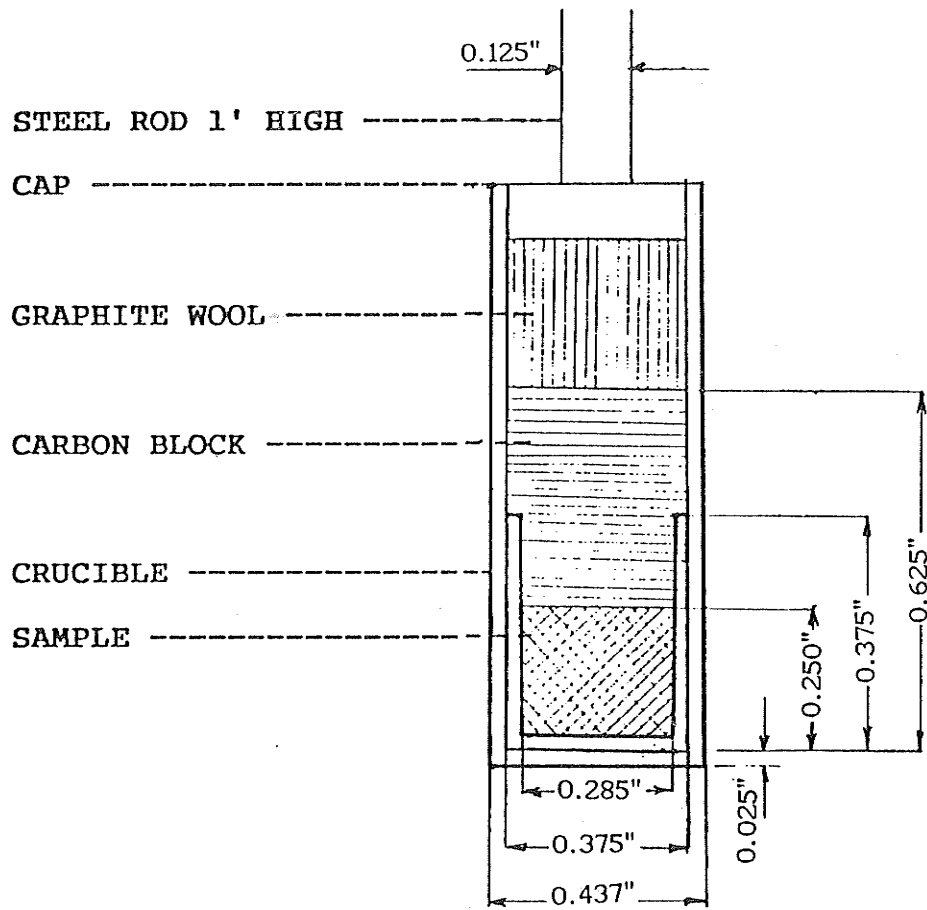


Figure 3-7: Crucible assembly for KC-135 samples.



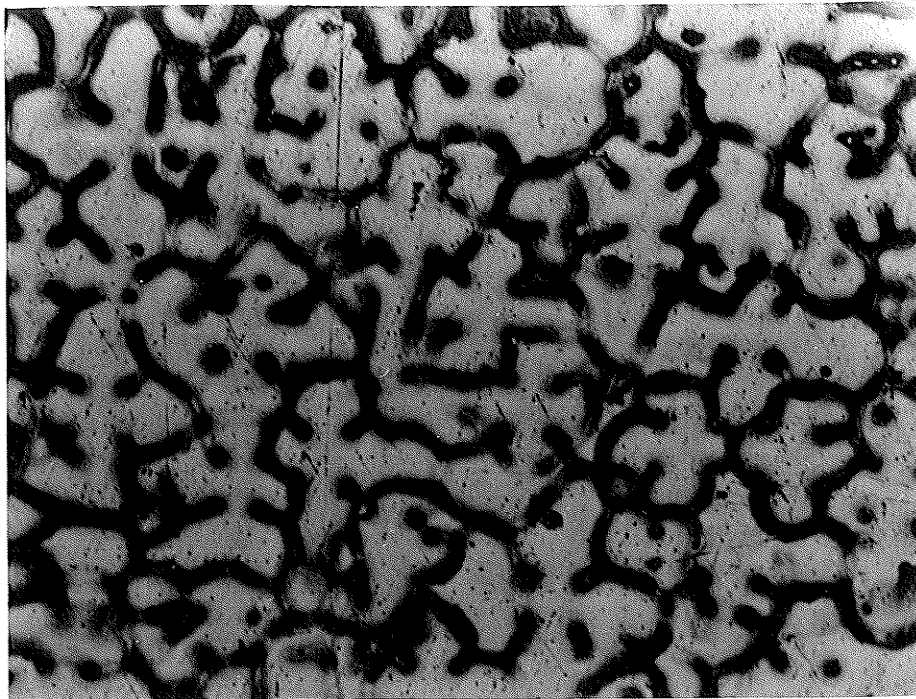


Figure 3-8: Cross section of KC-135 samples. It shows hexagonal array of primary arm centres.

# CHAPTER IV

## RESULTS

### 4-1 DENDRITIC STRUCTURE OF SOLIDIFIED ALLOYS

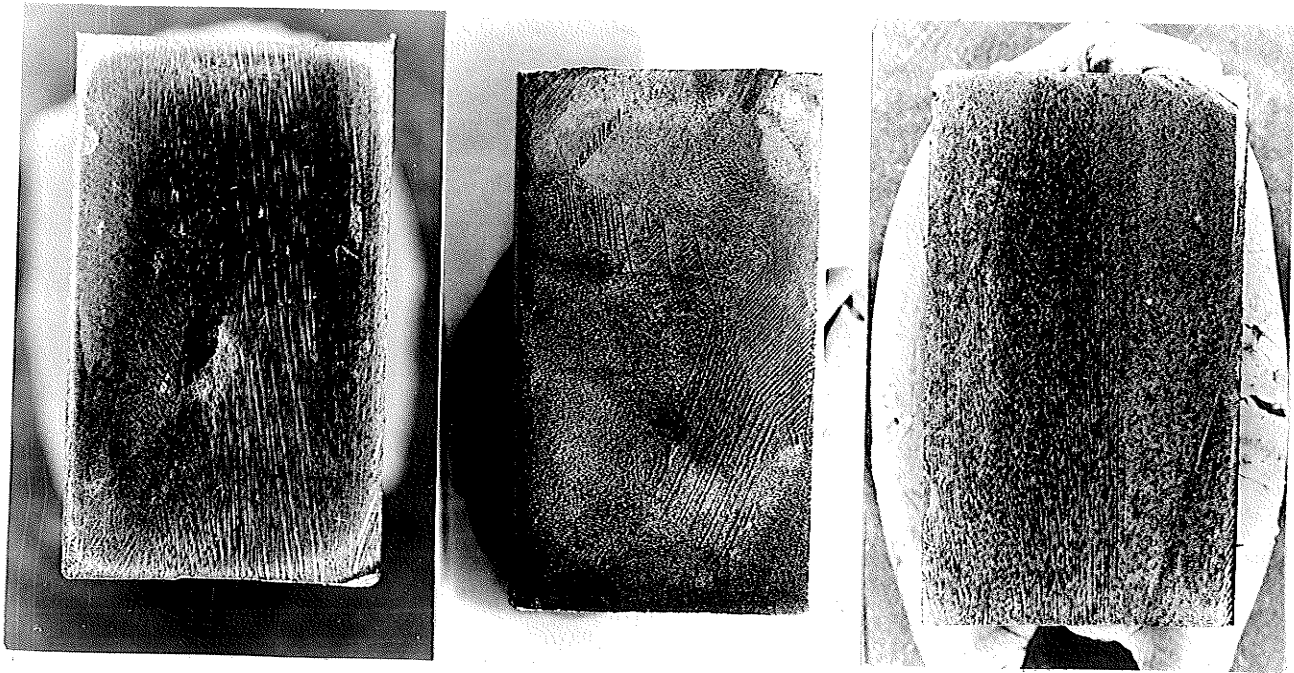
Longitudinal Cross Sections of the samples were examined for directional solidification before any analysis. Macrostructures showed dendritic solidification starting from chill face. Figure 4-1 illustrates the longitudinal cross-section of the three alloys, Al-4%Cu, Pb-15%Sn and Sn-15%Pb, solidified opposite to gravity.

Microstructure examination of Al-4%Cu ingots showed eutectic particles of  $\theta$ +Al in the matrix of Al for both AC-OG and AC-PG ingots as it is expected( Figures 4-2 and 4-3). However as shown in Figure 4-4,  $\theta$  phase in Al-15G ingot is not in the form of lamellar eutectic. In other words interphase spacing in eutectic has increased by increasing gravity.

Pb-15%Sn ingot had a good dendritic structure on the cross section perpendicular to the primary arms as is illustrated in figure 4-5. Microstructure of this alloy, chemically polished by a solution of 75% acetic acid and 25%  $H_2O_2$ , shows two phase eutectic of Pb+Sn between the lead particles.

Figure 4-6 shows the microstructure of Sn-15%Pb alloy. Eutectic structure around the cells of Sn phase can be observed in these cross sections. White particles are contamination resulting from polishing. Since the material is very soft, removing these particles without etching is very difficult.

All the pictures were taken in scanning electron microscope by using backscattered electron signals.



(a)

(b)

(c)

Figure 4-1: longitudinal cross section of ingots solidified opposite to gravity; (a) Al-4%Cu, (b) Sn-15%Pb, (c) Pb-15%Sn.

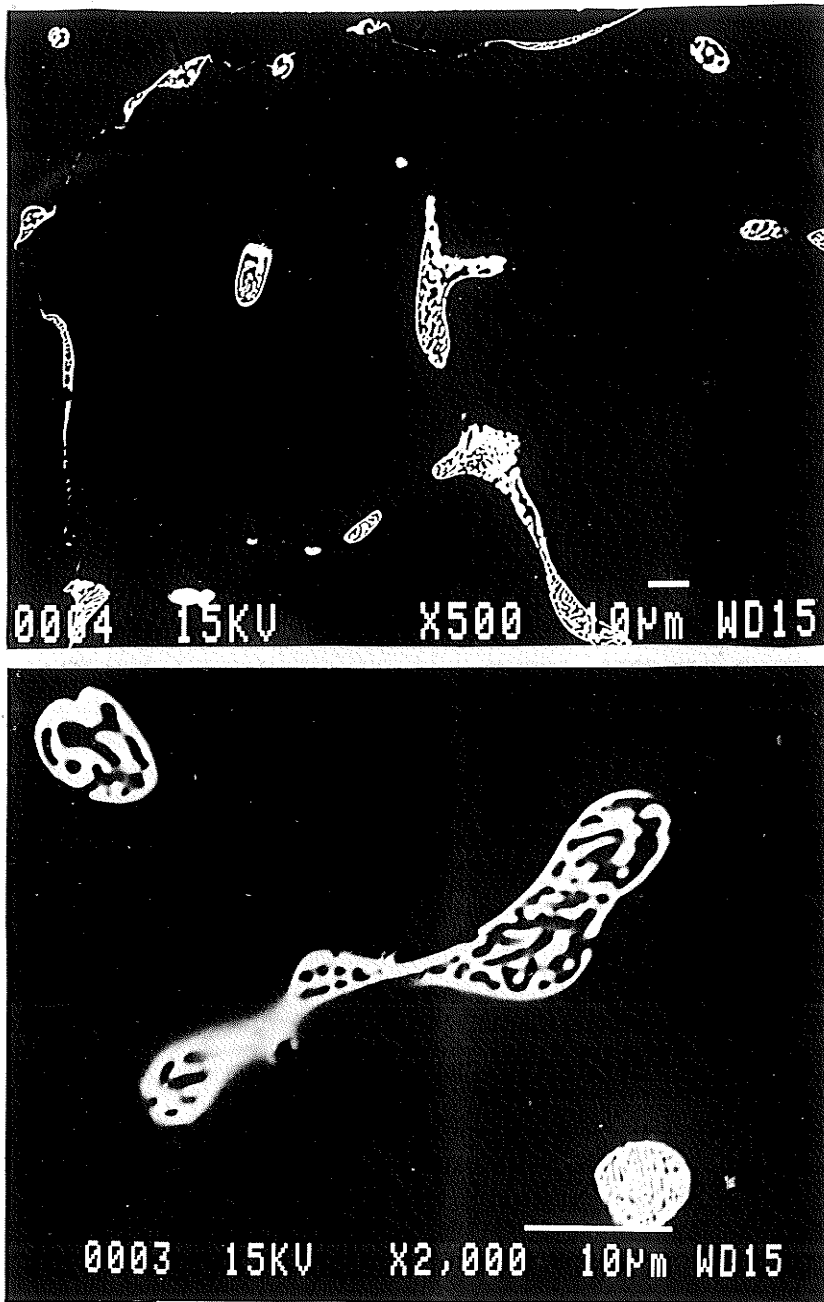


Figure 4-2: Microstructure of Al-4%Cu ingot, solidified opposite to gravity. Backscattered electron picture under SEM.

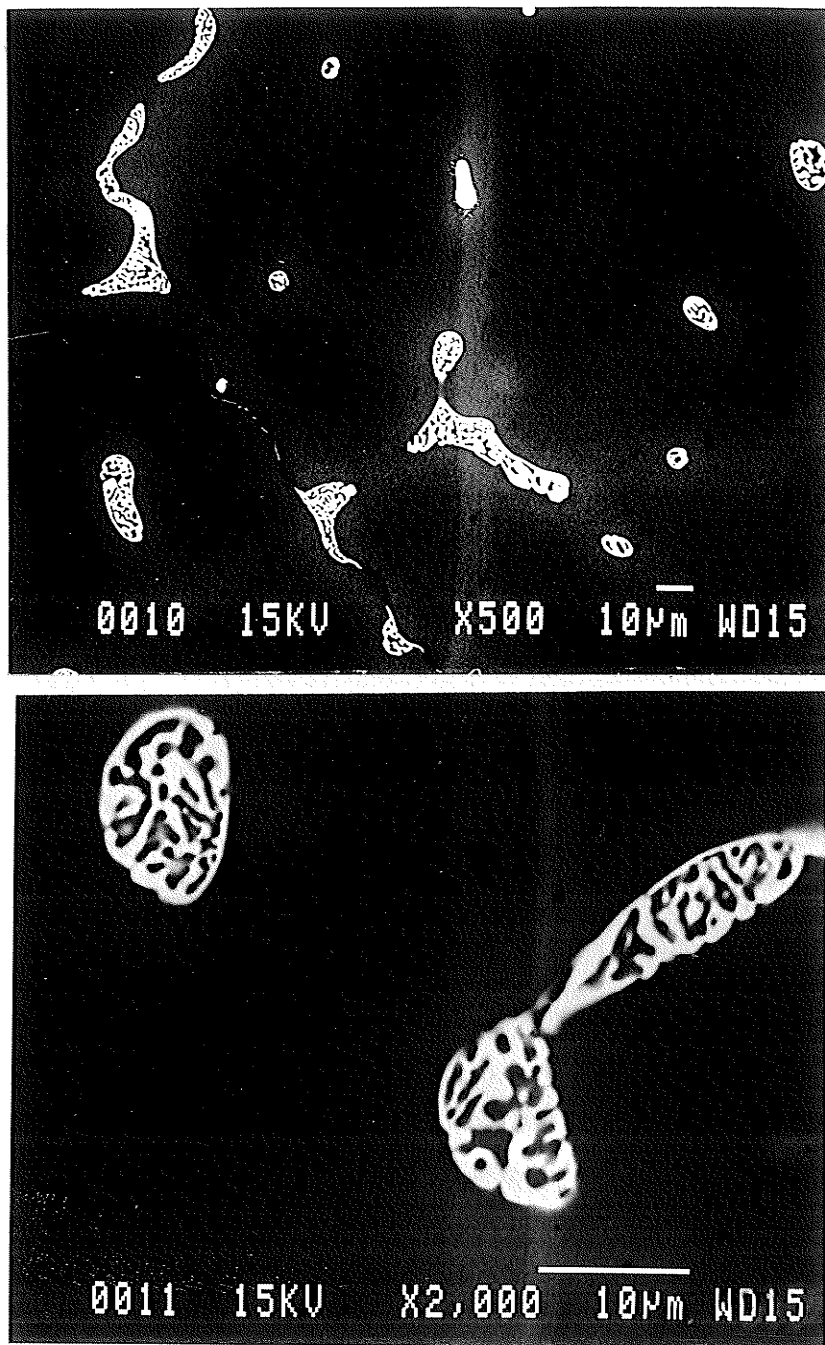


Figure 4-3: Microstructure of Al-4%Cu ingot, solidified parallel to gravity. Backscattered electron picture under SEM.

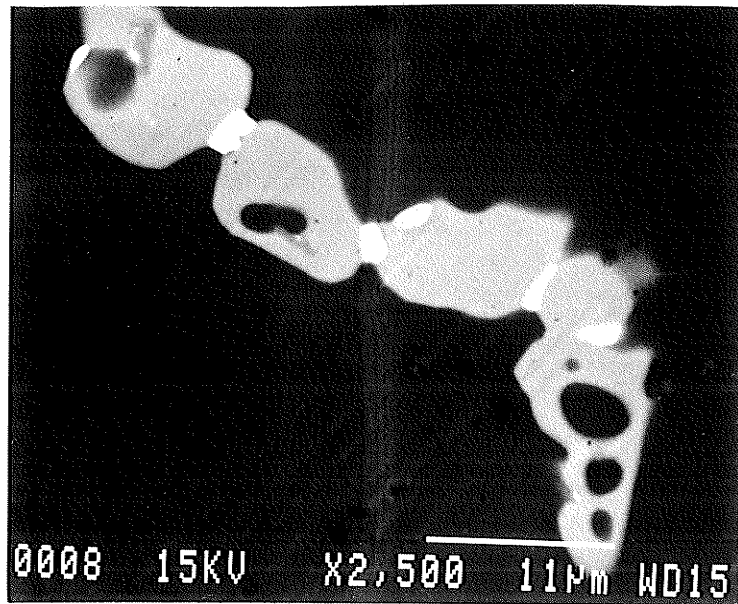
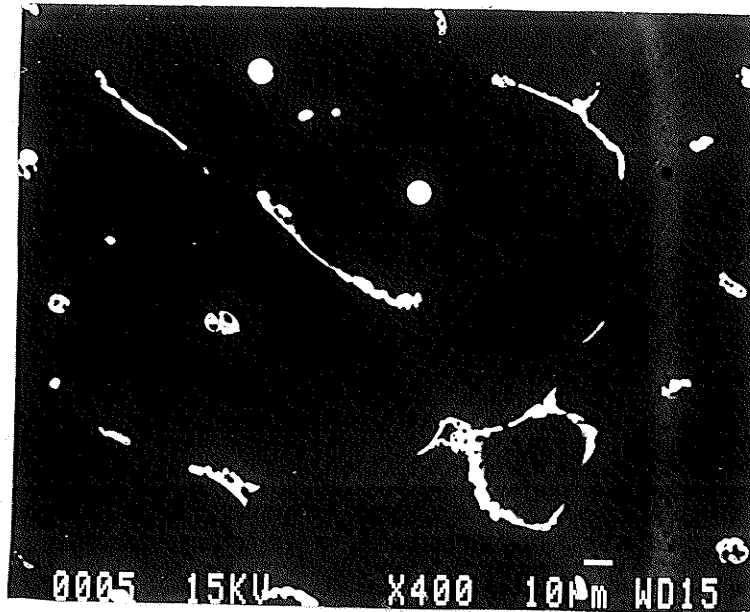
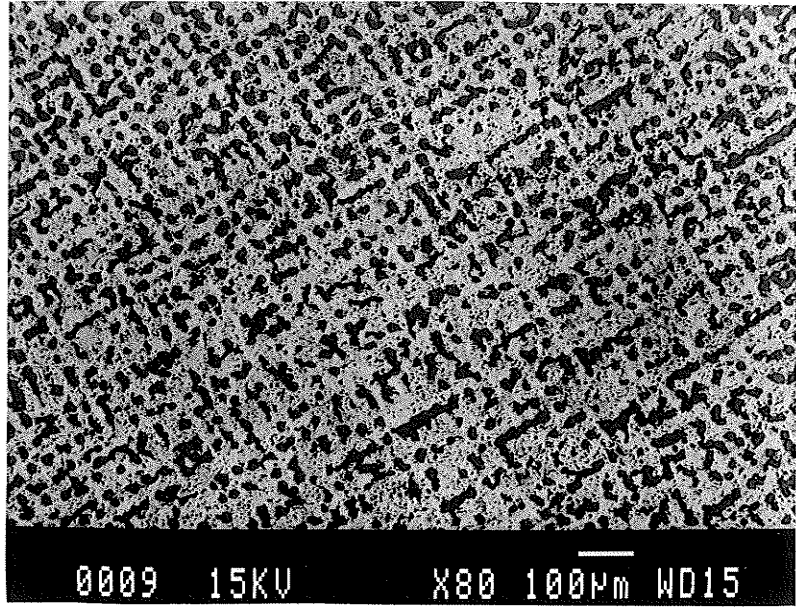


Figure 4-4: Microstructure of Al-4%Cu ingot, solidified in 15 times gravity.  
Backscattered electron picture under SEM.

(a)



(b)

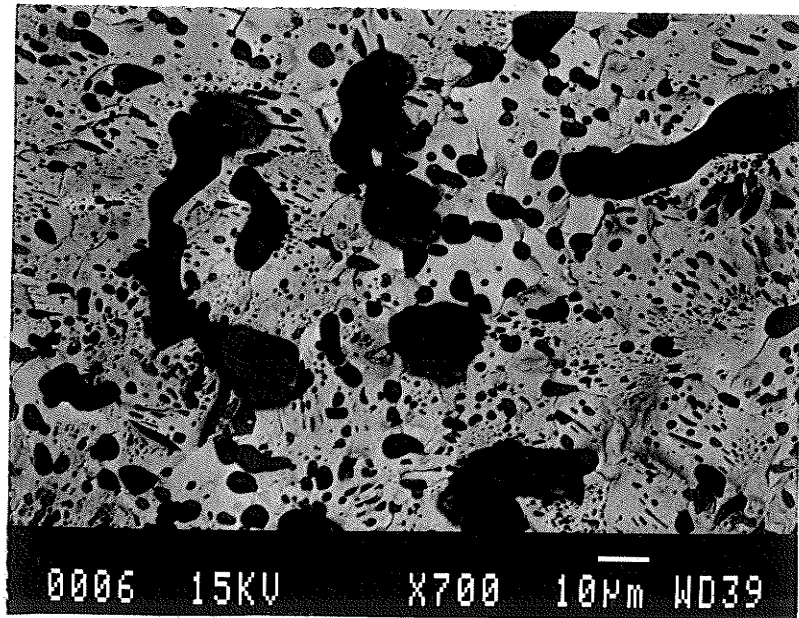


Figure 4-5: Microstructure of Pb-15%Sn ingots.(a) Dendritic structure in transverse cross section, (b) lead particles (dark) in the eutectic matrix. Sample is chemically polished by 75% acetic acid and 25%  $H_2O_2$

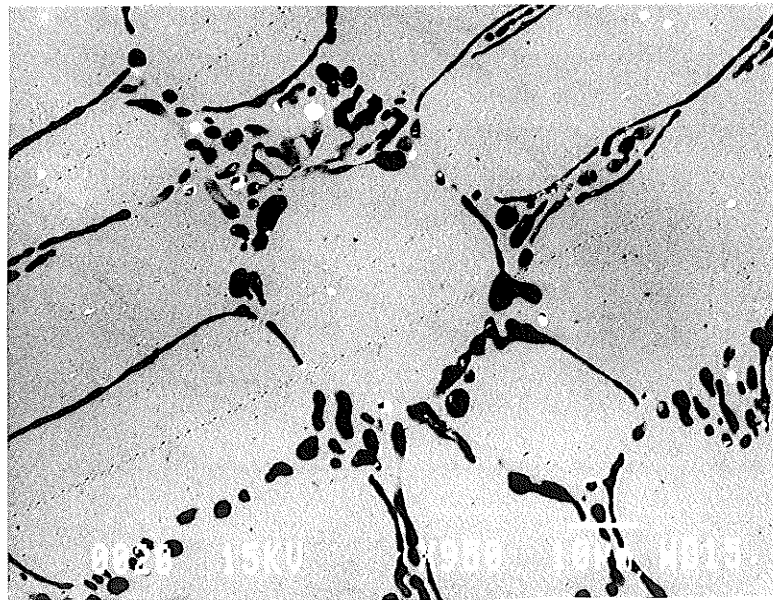
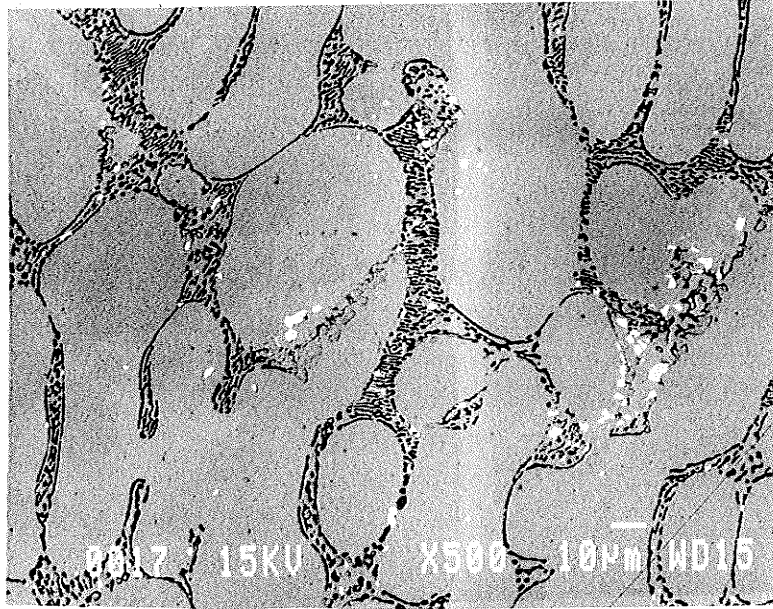


Figure 4-6: Microstructure of Sn-15%Pb ingots. Tin cells (lighter phase) surrounded by eutectic.



## 4-2 TEMPERATURE GRADIENTS AND COOLING RATES

The temperature of the melt during solidification was measured by four thermocouples located at various distances from the chill face in the graphite crucible. Cooling curves of the ingots solidified opposite to gravity as well as parallel to gravity are shown in Figures 4-7, 4-8 and 4-9 for Al-4%Cu, Sn-15%Pb and Pb-15%Sn respectively. The number on each curve indicates the distance of the thermocouple from the chill face. Figure 4-10 shows the cooling curve of Al-4% Cu ingot solidified in 15 times gravity. All ingots were superheated to 750°C, 350°C and 250°C for aluminium-copper, lead-tin and tin-lead respectively. In the freezing range the cooling is seen to occur with a nearly steady state rate in the melt close to chill face as well as the melt away from it. However the cooling rate near the chill face was found to be higher than that near the opposite end both before and during the freezing period.

Table 4-1 lists the average cooling rates, temperature gradients and growth velocities calculated from the cooling curve for Al-4%Cu(AC), Sn-15%Pb (SP) and Pb-15%Sn(PS). There are no apparent differences in the cooling characteristic of AC, SP and PS samples solidified parallel to or opposite to gravity.

## 4-3 MACROSEGREGATION ALONG SOLIDIFIED INGOT

Segregation of solute element along the directionally solidified ingot was determined for all ten ingots of three different composition.

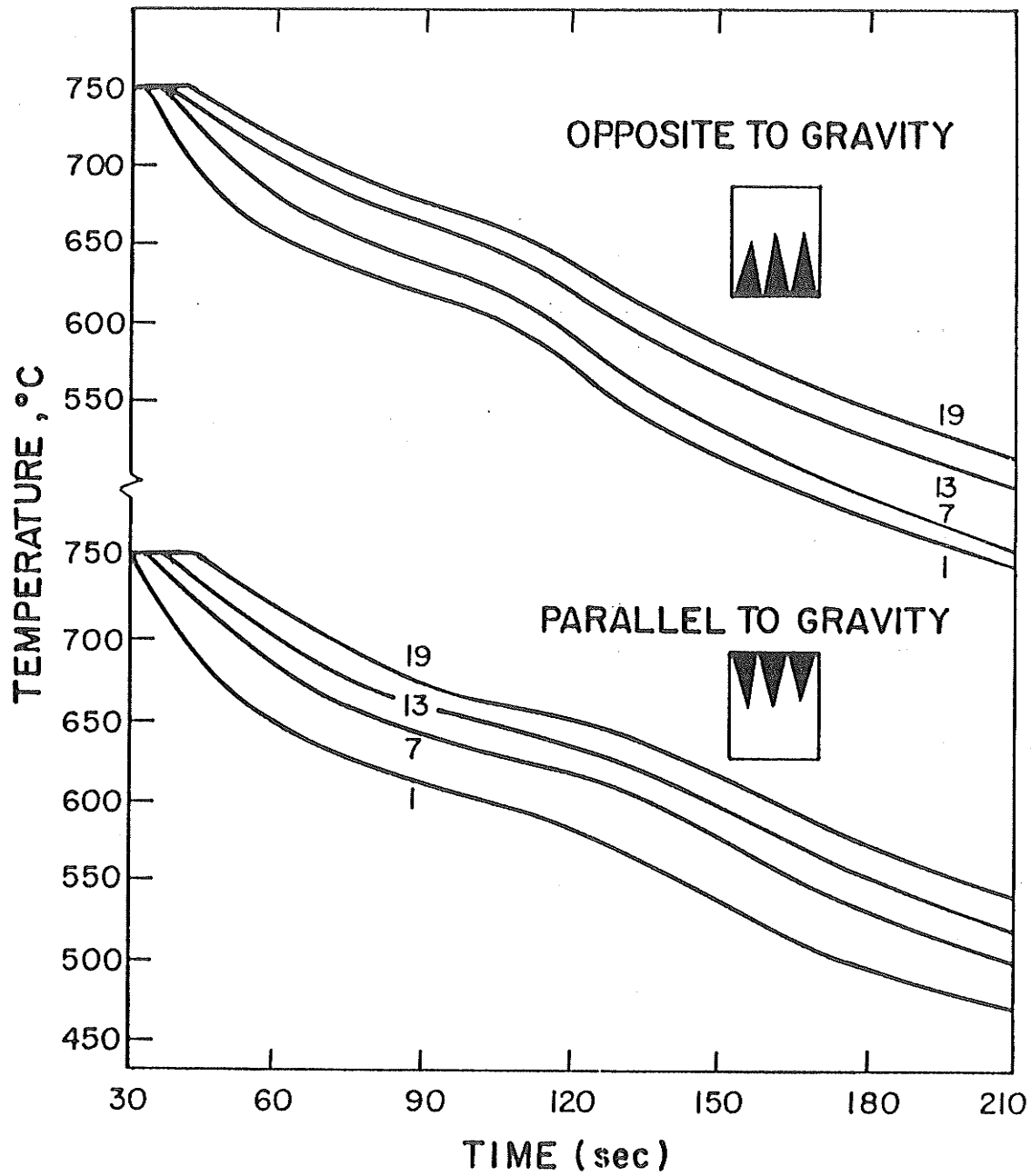


Figure 4-7: Cooling curves of Al-4% Cu samples solidified opposite to gravity, (OG), and parallel to gravity, (PG).

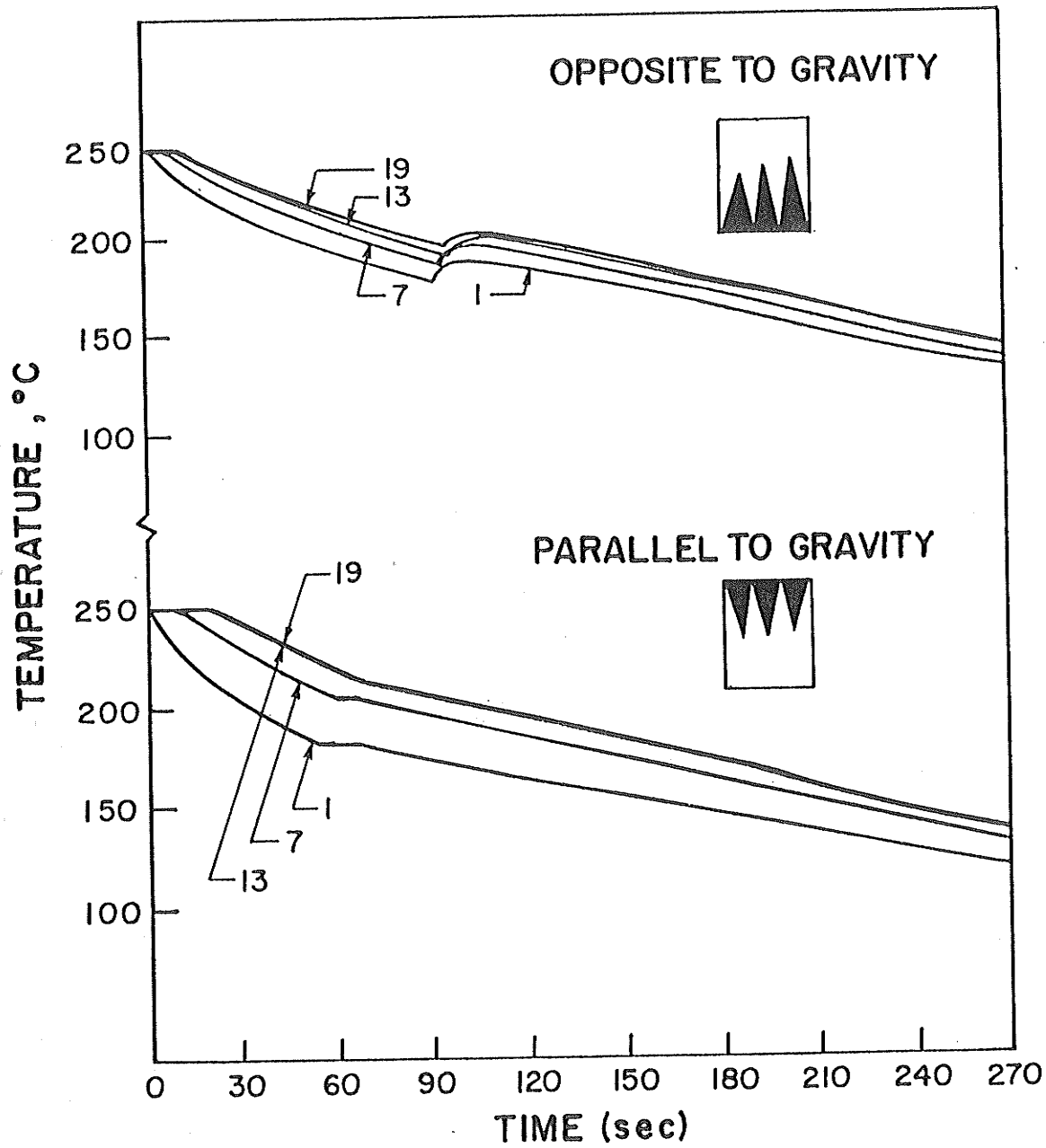


Figure 4-8: Cooling curve of Sn-15% Pb ingots, solidified opposite and parallel to gravity.

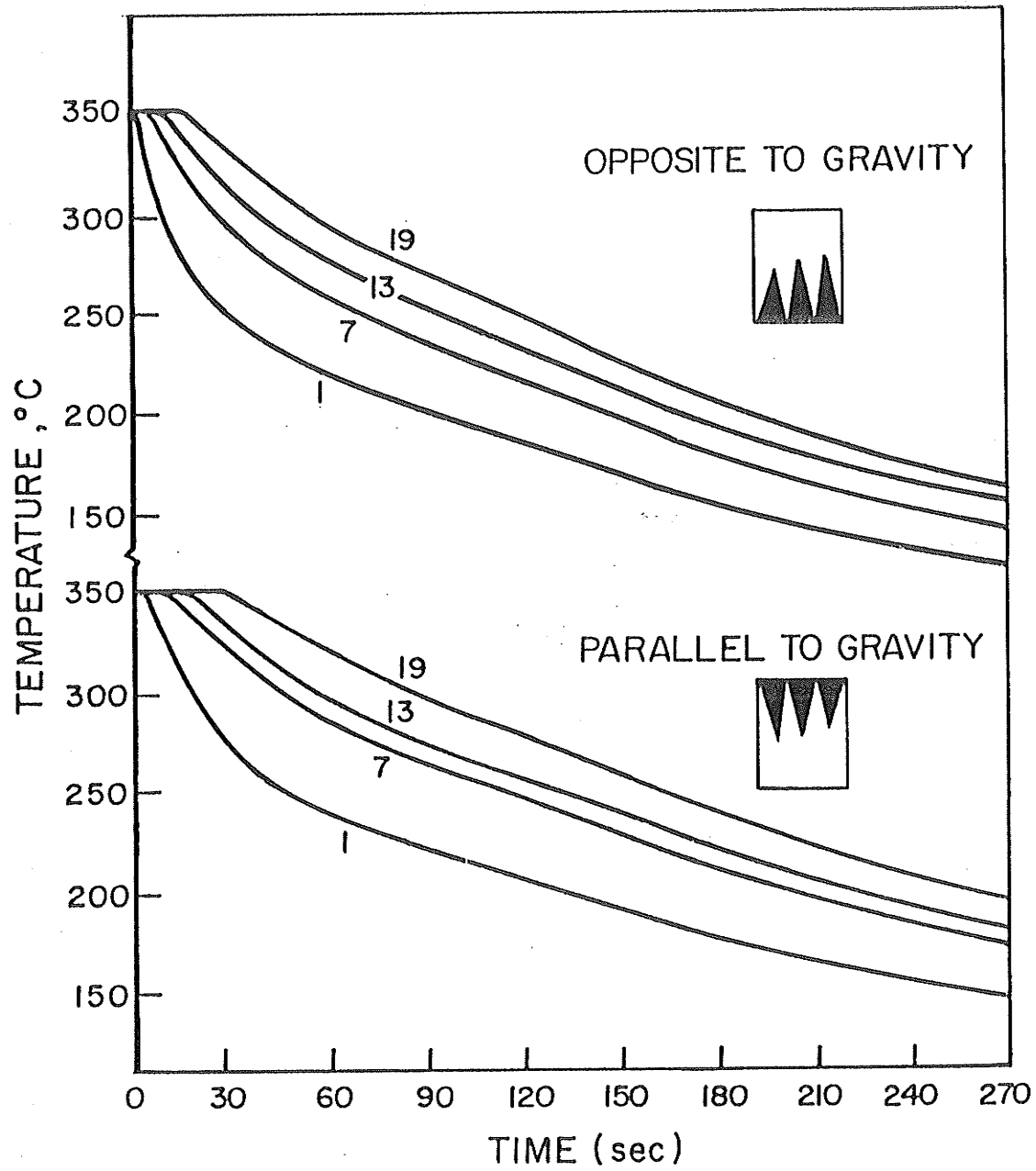


Figure 4-9: Cooling curve of Pb-15% Sn ingots, solidified opposite and parallel to gravity.

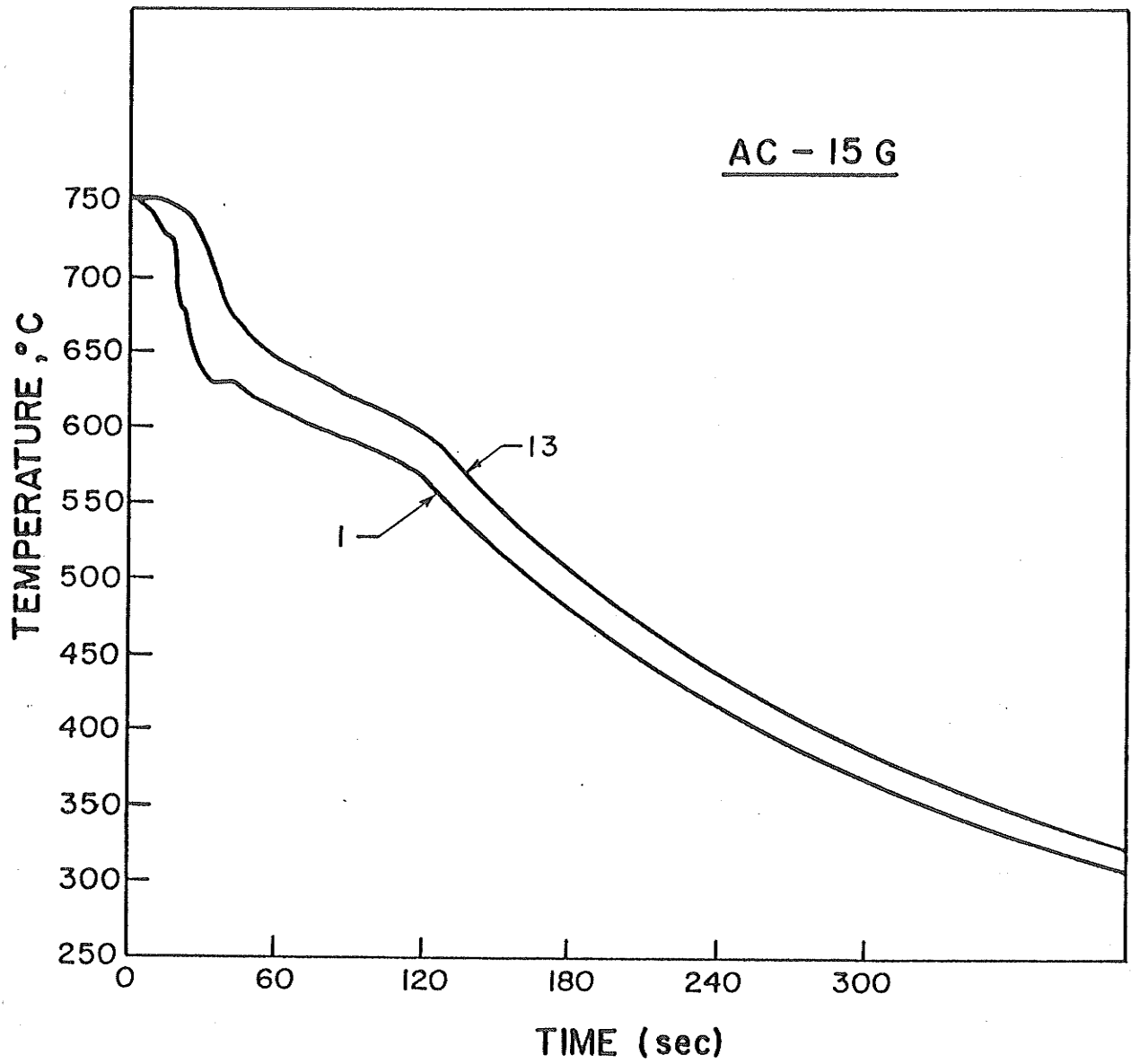


Figure 4-10: Cooling curve of Al 4%Cu ingot, solidified in 15 times gravity.

Table 4-1: Cooling characteristics of ingots

Ingot	Average Cooling rate $^{\circ}\text{K/Sec}$ $\left(\frac{\partial T}{\partial t}\right)$	Average Temperature gradient $,G, ^{\circ}\text{K/mm}$ $\left(\frac{\partial T}{\partial x}\right)$	Average growth velocity, R, mm/Sec
AC-OG	1.16	3.80	0.36
AC-PG	1.10	3.50	0.33
AC-15G	0.80	2.40	0.33
SP-OG	0.51	1.24	0.41
SP-PG	0.78	2.40	0.20
PS-OG	0.75	4.13	0.27
PS-PG	0.65	4.50	0.20

#### 4-3-1 AL-4%CU ALLOY

Macrosegregation data (Table 4-2) obtained by EDS analysis for Al-4%Cu indicates that inverse segregation occurs in all of the three ingots.

Figure 4-11 illustrates the copper contents as a function of the distance from the chill face in the sample solidified opposite to gravity(AC-OG). The macrosegregation data determined from the Inductively Coupled Plasma Techniques are also shown which agree quite well with EDS data.

The data for the ingot solidified parallel to gravity(AC-PG) is shown in Figure 4-12. The presence of inverse segregation in this sample is also evident. In AC-PG ingot, despite

solidification front moving downward (parallel to gravity) higher density liquid (rich in copper) has moved upward against the gravity to accommodate the shrinkage, and thus causing inverse segregation. Similar results were obtained for the sample solidified in 15G (Figure 4-13).

Table 4-2: Macrosegregation in Al-4% Cu ingots.

Distance from chill face (mm)	Percent copper		
	AC-OG	AC-PG	AC-15G
0	4.22±0.09	4.28±0.17	4.17±0.05
2	4.39±0.06	4.04±0.12	3.95±0.01
4	4.17±0.11	3.94±0.14	4.11±0.03
6	3.99±0.10	3.98±0.05	4.04±0.03
8	3.93±0.06	3.89±0.11	3.94±0.09
10	3.87±0.13	3.87±0.10	3.92±0.06
12	3.84±0.08	4.00±0.10	3.67±0.08
14	3.63±0.03	3.79±0.09	3.83±0.07
16	3.65±0.07	4.05±0.10	3.88±0.16
18	3.65±0.05	3.89±0.14	3.80±0.04
20	3.65±0.07	3.80±0.13	3.58±0.05
22	3.60±0.07	3.69±0.10	3.72±0.05
24		3.63±0.07	3.67±0.05
28		3.78±0.12	

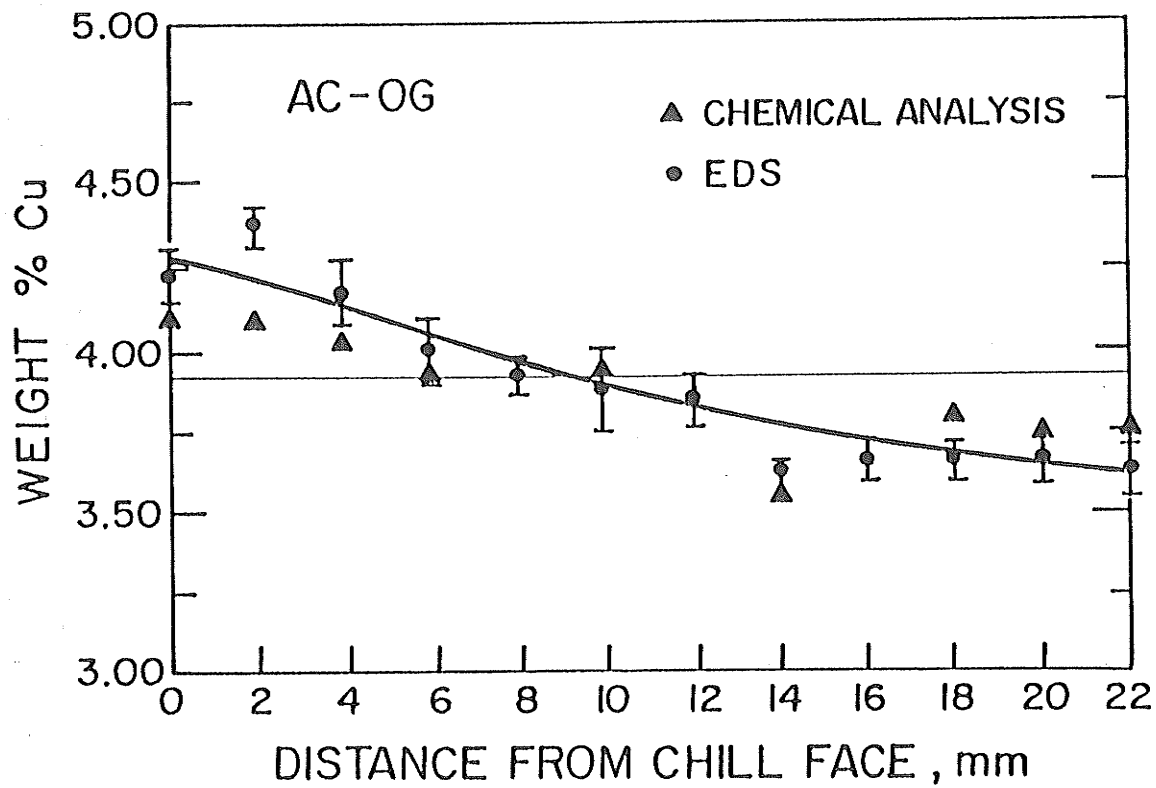


Figure 4-11: Macrosegregation data for Al-4% Cu solidified opposite to gravity.



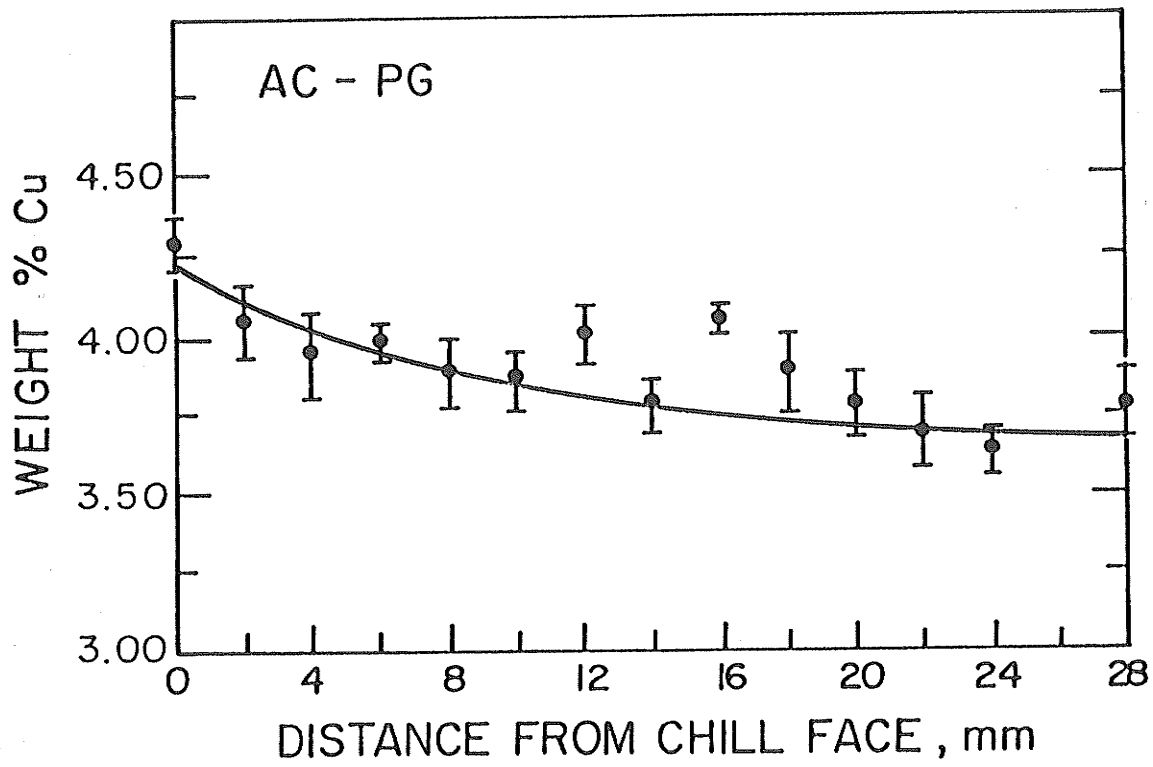


Figure 4-12: Macrosegregation data for Al-4% Cu solidified parallel to gravity.

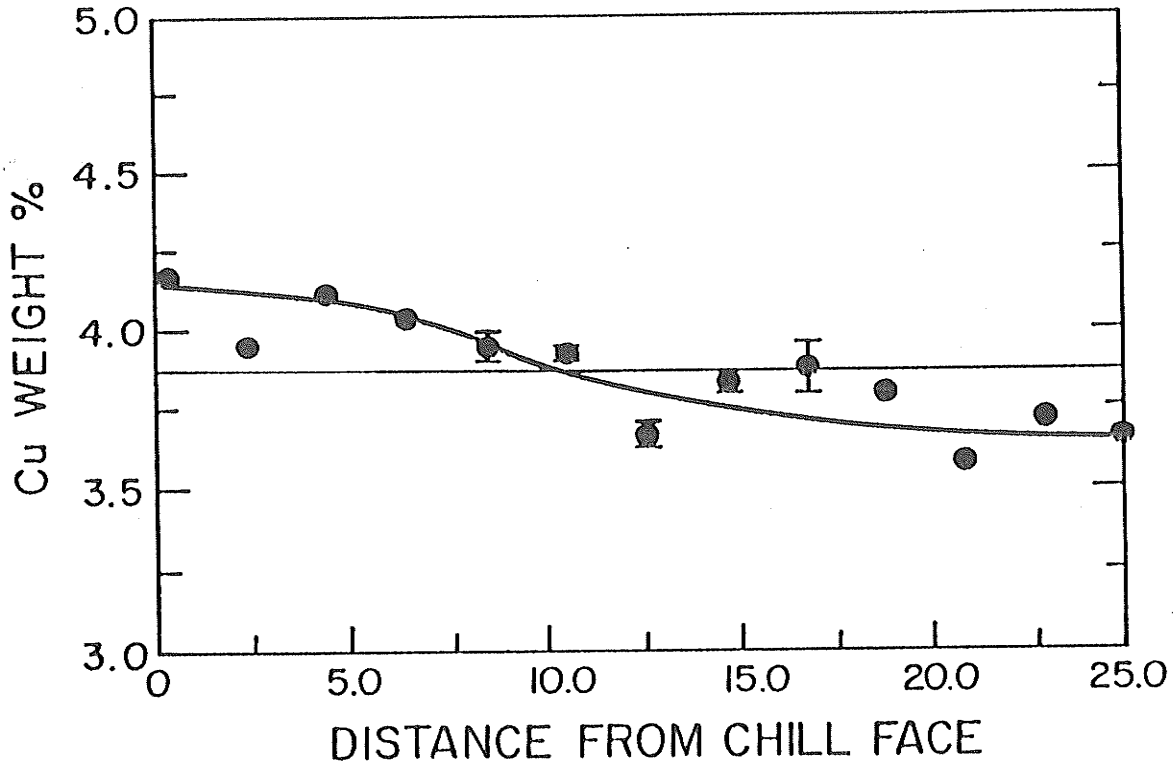


Figure 4-13: Macroseggregation data for Al-4% Cu solidified in high gravity.

For Al-4%Cu alloy, neither the direction of the gravity vector, nor high gravity, affected the inverse segregation within the accuracy of the analysis technique used.

#### 4-3-2 PB-15%SN ALLOY

Macrosegregation data from the EDS analysis for Pb-15%Sn ingots solidified opposite to gravity (PS-OG) and parallel to gravity (PS-PG) are shown in Figure 4-14. Gravitational segregation is evident in both graphs. During the melting of the sample lower density eutectic phase melts first. As the higher density lead phase melts, it settles down on the bottom of the crucible. Although the melt stays in crucible for 15-30 minutes after melting, thermal agitation is not able to homogenize the melt. Such gravitational segregation has also been noted in a previous investigation [34]. However the cooling rates used were much slower.

Figure 4-14 also illustrates the results of chemical analysis(Inductively Coupled Plasma Technique) for PS-OG sample which agrees fairly with the results of EDS analysis.

The results of the analysis for the sample which has been mechanically mixed (Figure 4-15) shows chill face segregation of about 2%. This is more than what can be expected for inverse segregation in this alloy. As a result there is still some gravity segregation during solidification of this alloy. Analysis could be carried out only for 2/3 of the sample due to some solidification starting from the other end.

All EDS data for Pb-15%Sn ingots are tabulated in Table 4-3.

Table 4-3: Macrosegregation in Pb-15%Sn ingots.

Distance from chill face (mm)	Percent tin		
	PS-OG	PS-PG	PS-Mixed
0-2	15.60±0.04	15.45±0.04	17.13±0.04
2-4	15.68±1.34	15.19±0.23	15.96±0.14
4-6	15.77±0.08	15.40±0.11	15.08±0.09
6-8	15.62±0.11	15.39±0.04	14.90±0.16
8-10	14.92±0.12	15.16±0.24	14.95±0.19
10-12	15.09±0.17	15.25±0.21	15.03±0.06
12-14	15.45±0.26	15.05±0.09	14.68±0.11
14-16	14.71±0.17	15.44±0.08	15.01±0.12
16-18	15.42±0.20	14.74±0.18	14.94±0.17
18-20	15.59±0.41	15.01±0.13	14.90±0.20
20-22	15.53±0.25	14.70±0.12	14.13±0.20
22-24	16.83±1.18	14.23±0.16	
24-26	16.60±0.13	14.06±0.08	

#### 4-3-3 SN-15%PB ALLOY

Macrosegregation analysis of Sn-15%Pb ingots showed the same results as Pb-15%Sn samples. Gravitational segregation in PS-OG and PS-PG ingots are illustrated in Figure 4-16 and inverse segregation in mixed ingot is evident in Figure 4-17. The 1%

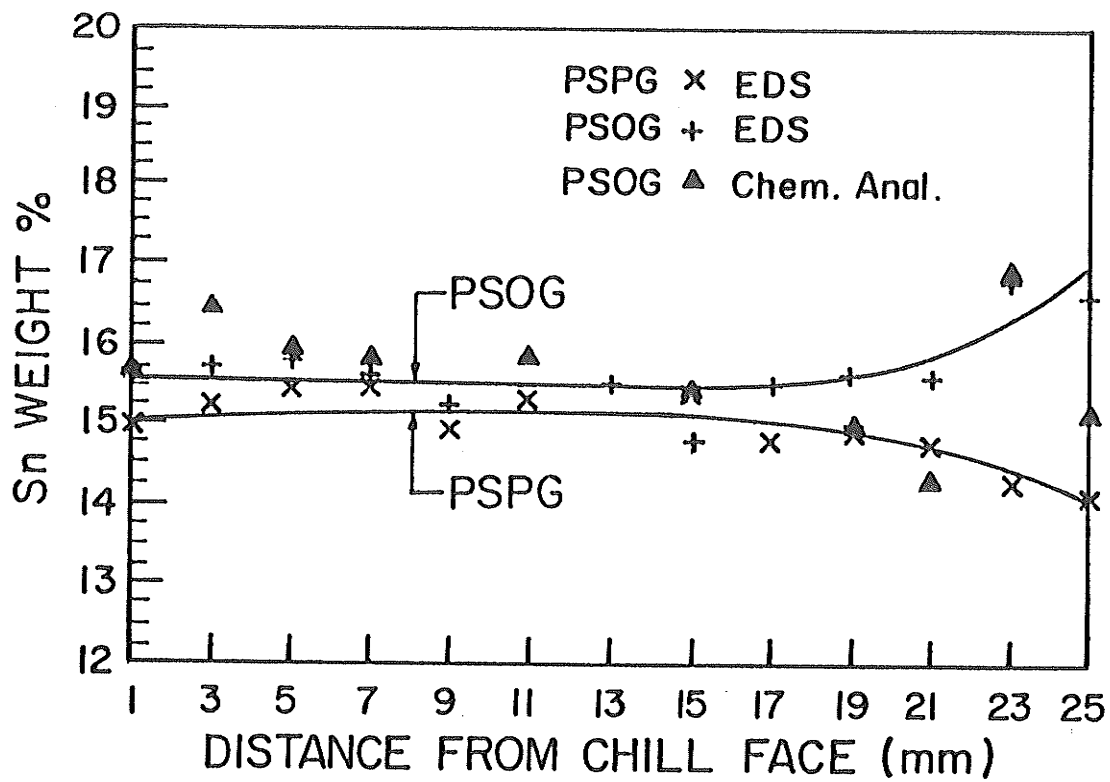


Figure 4-14: Macrosegregation data for Pb-15%Sn solidified opposite, (OG), and parallel, (PG), to gravity.

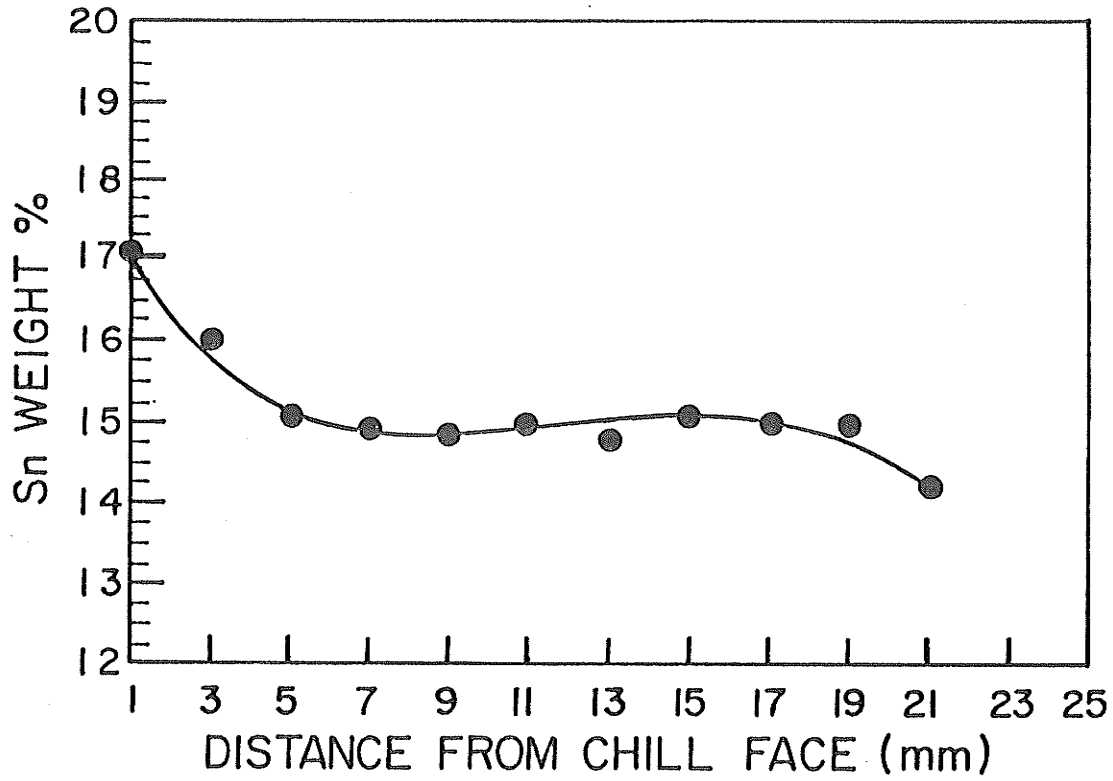


Figure 4-15: Chill face segregation in Pb-15%Sn. Ingot is directionally solidified after mechanical mixing.

Table 4-4 Macrosegregation in Sn-15%Pb ingots.

Distance from chill face(mm)*	Percent lead			
	SP-OG	SP-PG	SP-Quenched	SP-Mixed
0 (0-2)	19.32±0.13	12.07±0.06	17.56±0.19	15.82±0.07
2 (2-4)	18.59±0.12	12.93±0.19	22.62±0.10	14.89±0.20
4 (4-6)	18.56±0.15	13.79±0.19	17.59±0.12	14.96±0.07
6 (6-8)	17.31±0.09	13.74±0.06	14.27±0.13	13.34±0.24
8 (8-10)	16.33±0.21	14.84±0.09	14.01±0.22	12.91±0.20
10 (10-12)	14.60±0.07	14.51±0.18	13.75±0.18	12.26±0.11
12(12-14)	14.16±0.12	14.44±0.14	14.22±0.11	11.91±0.12
14 (14-16)	13.17±0.29	14.92±0.13	14.25±0.10	12.61±0.10
16 (16-18)	13.52±0.22	15.32±0.08	12.46±0.16	12.55±0.05
18 (18-20)	12.81±0.14	16.14±0.28	13.20±0.12	12.68±0.05
20 (20-22)	11.14±0.10	15.81±0.16	14.27±0.08	13.07±0.19
22 (22-24)	10.54±0.12	17.67±0.23	13.96±0.07	13.84±0.16
24 (24-26)		18.84±0.07	12.79±0.16	

\*Only for SP-mixed, sample has been analysed on longitudinal cross section, so the distance changes between (0-2) etc.

chill face inverse segregation found is of about the same magnitude as expected from the mechanism of inverse segregation.

In order to confirm the gravitational segregation of lead, a melt of Sn-15%Pb was kept stationary for 30 minutes in a stainless steel crucible using the same furnace set up

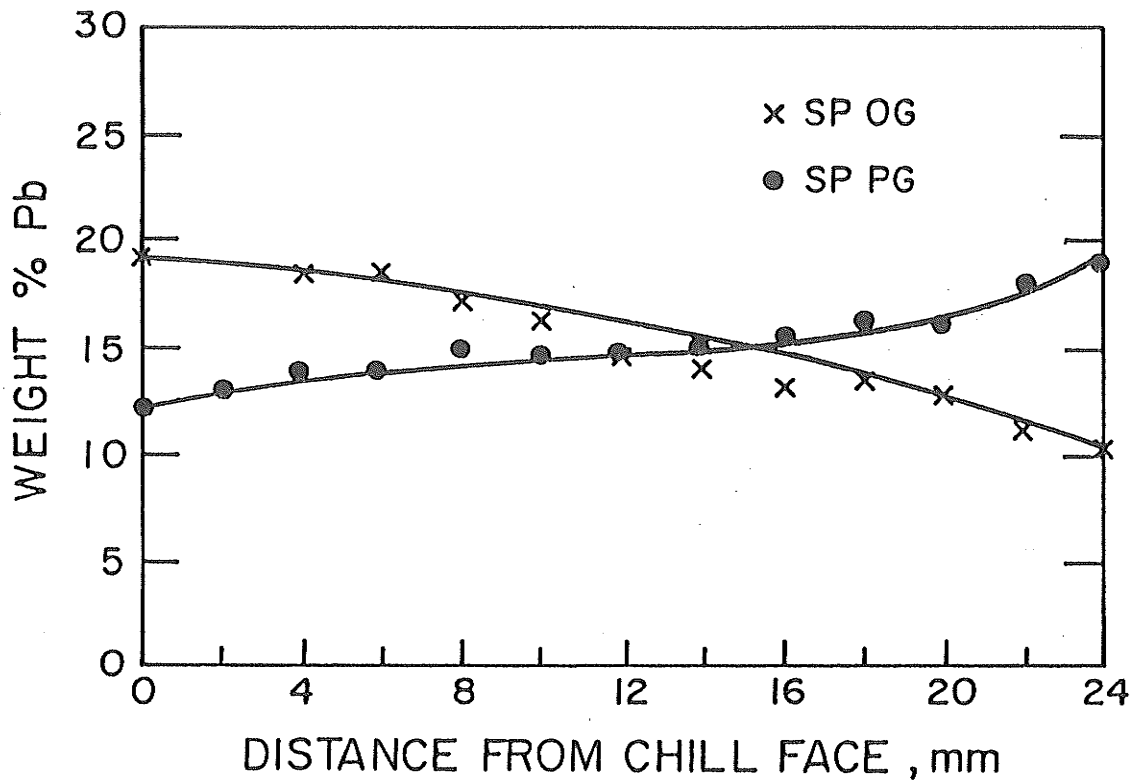


Figure 4-16: Macroseggregation data for Sn-15%Pb solidified opposite, (OG), and parallel, (PG), to gravity.



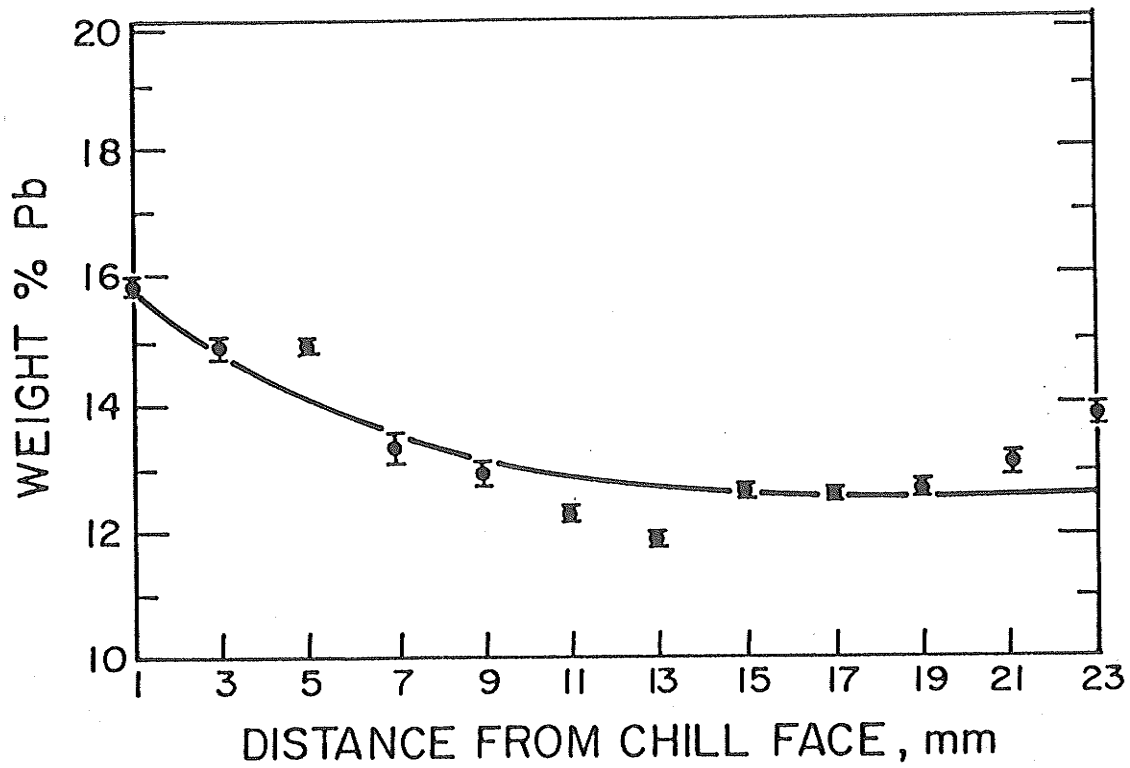


Figure 4-17: Inverse segregation in Pb-15%Sn. Ingot is directionally solidified after mechanical mixing.

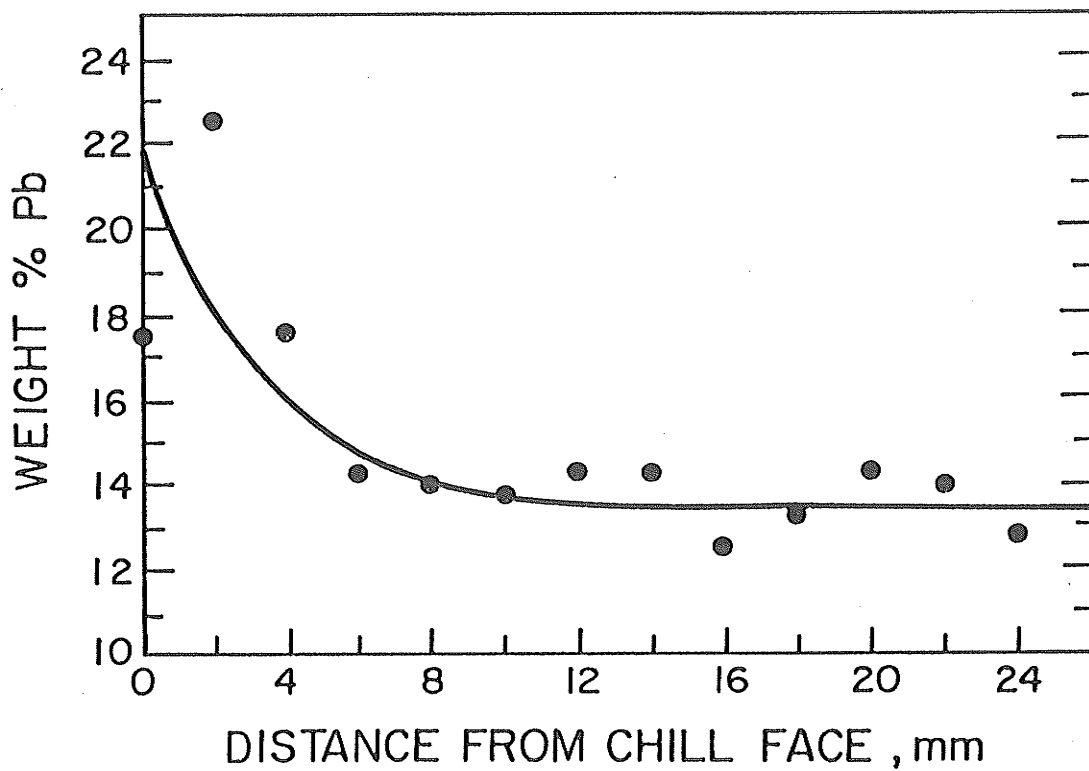


Figure 4-18: Gravity segregation in Sn-15%Pb. The molten ingot is quenched in iced brine.

and then quenched in iced brine. This would freeze any concentration gradients, if present in the melt since solidification occurs radially, rather than longitudinally. An EDS analysis of variation of lead away from the chill face was performed and the data is given in Figure 4-18. A high concentration of lead at the chill face is indicative of gravitational segregation of lead in such a system.

All EDS data for Sn-15% Pb ingots are Tabulated in Table 4-4.

#### 4-4 MICROSEGREGATION IN AL-4%CU ALLOY

The average minimum composition of two scans in three dendrites is summarised in Table 4-5. The distance of each spot from eutectic particles in each scan was measured on the photograph taken after the analysis (similar to Figure 3-4). Minimum composition was found on the curve showing the variation of composition with distance for each scan. The spot with the minimum amount of copper was considered to be the centre of the dendrite. Copper content of each spot located at 5 and 10 micrometer from the centre of dendrite in each side was averaged for all scans. Figures 4-19, 4-20, and 4-21 show the microsegregation analysis data for AC-OG, AC-PG and AC-15G ingots.

It is seen that neither the direction of the gravity vector, nor high gravity affect the microsegregation within the accuracy of the analysis technique used.

#### 4-5 PRIMARY AND SECONDARY ARM SPACINGS

The average primary arm spacing, measured from about twenty photomicrographs of each sample for AC-OG, AC-PG and AC-15G is summarised in Table 4-6.

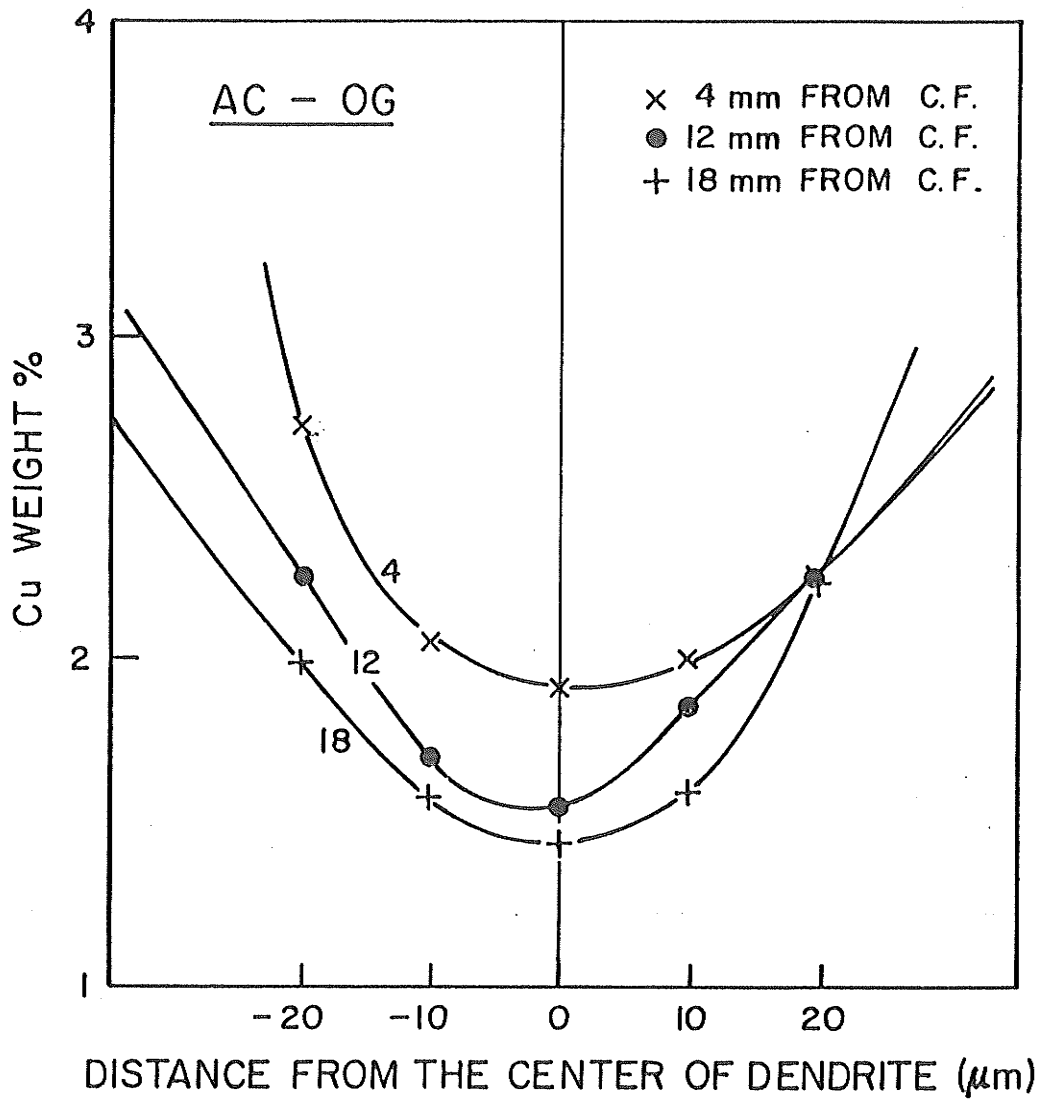


Figure 4-19: Microsegregation data of AC-OG ingot in three cross sections of 4, 12, and 18 mm from chill face.

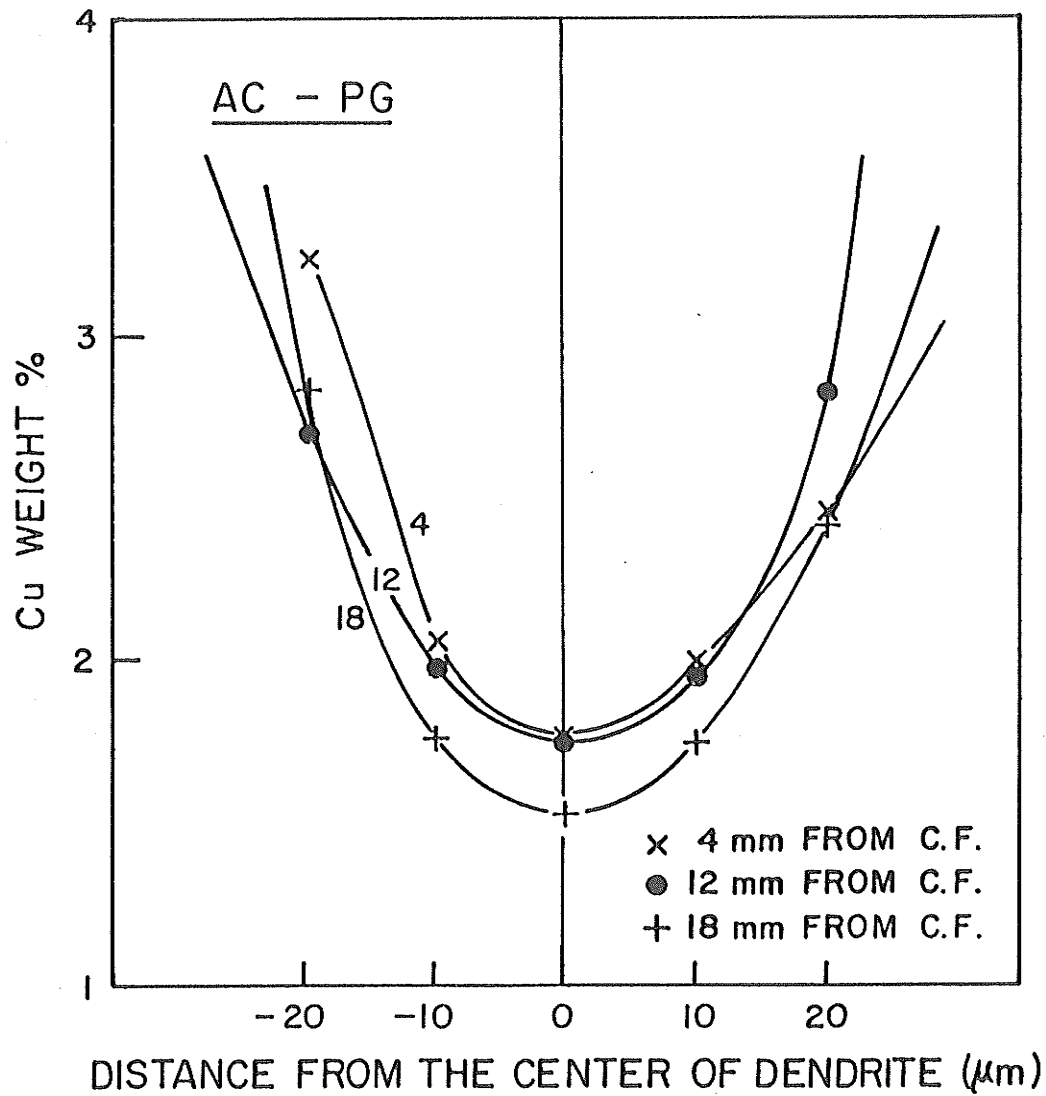


Figure 4-20: Microsegregation data of AC-PG ingot in three cross sections of 4, 12, and 18 mm from chill face.

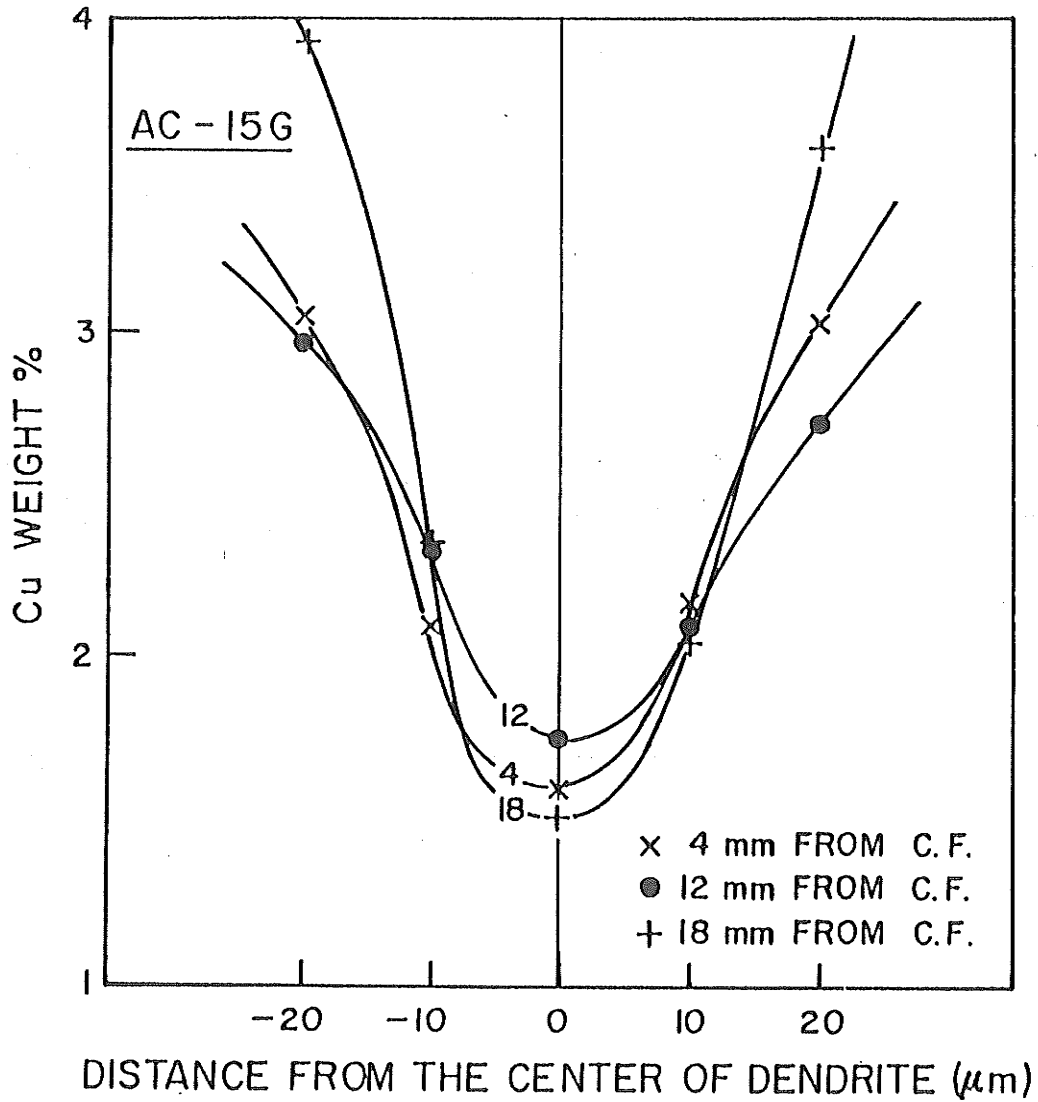


Figure 4-21: Microsegregation data of AC-15G ingot in three cross sections of 4, 12, and 18 mm from chill face.

In order to confirm the measurement of primary dendrite arm spacings, primary arm positions were marked on one of the photographs and the nearest neighbour spacing were measured directly. The average of over hundred measurements were very close to the results obtained by area counting method.

Table 4-5: Minimum composition of dendrites.

Sample	Distance from chill face (mm)	Average minimum composition (Percent copper)
AC-OG	4	1.90±0.13
	12	1.54±0.21
	18	1.44±0.21
	Average	1.59±0.25
AC-PG	4	1.77±0.16
	12	1.72±0.16
	18	1.57±0.14
	Average	1.69±0.18
AC-15G	4	1.60±0.22
	12	1.75±0.26
	18	1.51±0.07
	Average	1.62±0.22

The 95 percent confidence limit (CL) is calculated for each ingot using the following relationship [54]:

$$95\%CL = \frac{ts}{(N-1)^{1/2}}$$

where the value of t varies with N, the number of measurements, and S is the standard deviation.

Table 4-6: Primary arm spacings.

Sample	Distance from chill face (mm)	Primary arm spacing ( $\mu\text{m}$ )
AC-OG	4	183.16 $\pm$ 11.01
	12	197.37 $\pm$ 4.44
	14	205.81 $\pm$ 8.78
	Average	194.71 $\pm$ 7.52*
AC-PG	4	184.38 $\pm$ 33.64
	12	206.29 $\pm$ 7.55
	14	196.99 $\pm$ 13.76
	Average	196.56 $\pm$ 11.81*
AC-15G	4	184.54 $\pm$ 8.74
	12	177.83 $\pm$ 6.37
	14	160.58 $\pm$ 7.59
	Average	168.61 $\pm$ 5.27*

\*95%CL



Comparison of the results for the three slices of 4,12 and 18 mm from the chill face does not show specific change of primary arm spacings along all three ingots of AC-OG, AC-PG and AC-15G. However, the ingot solidified in high gravity shows smaller primary arm spacings.

Table 4-7 gives the results of secondary arm spacing measurements on longitudinal cross section. Since the cooling rate for high gravity sample was lower than the cooling rates for unit gravity ingots, (Table 4-1), high gravity sample shows higher secondary arm spacing.

Table 4-7: Secondary arm spacings.

Sample	Secondary arm spacing
AC-OG	36.51±1.61*
AC-PG	30.54±1.50*
AC-15G	42.90±2.49*

\*95%CL

## 4-6 KC-135 EXPERIMENTS

### 4-6-1 MACRO AND MICROSTRUCTURES

Three ingots solidified in zero, 1.8 and unit gravity were examined for directional solidification. Figures 4-22(a), (b) and (c) shows the longitudinal cross section of these ingots.

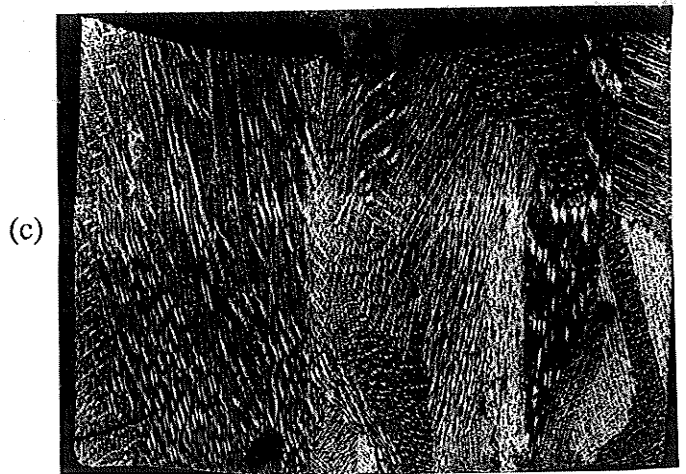
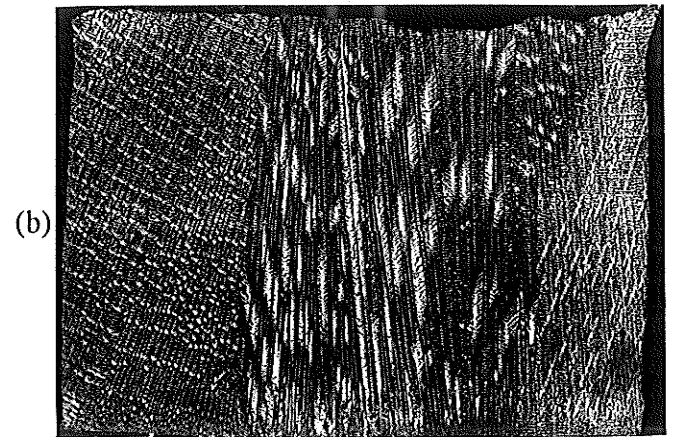
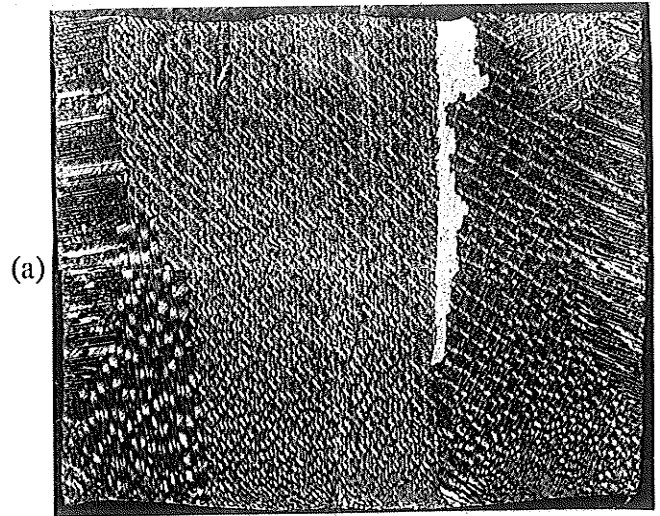


Figure 4-22: Longitudinal cross section of ingots solidified in, (a) zero, (b) unit and (c) 1.8 times gravity

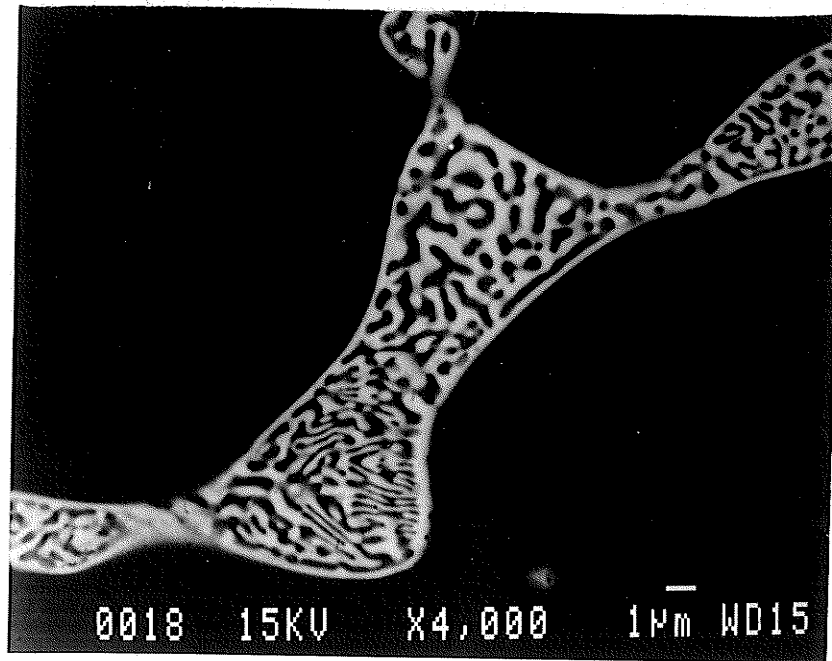
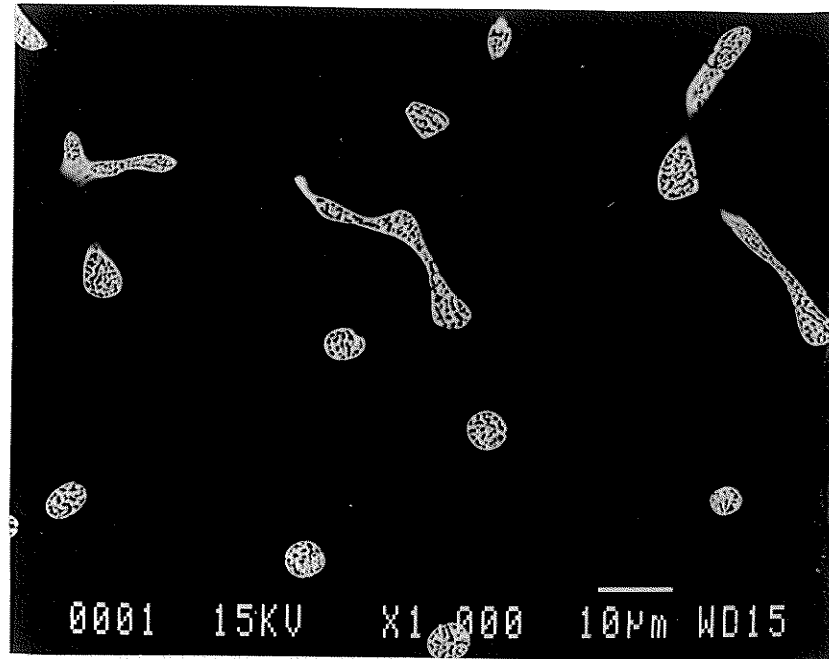


Figure 4-23: Microstructure of unit gravity ingot. Eutectic particles in the matrix of aluminium phase (dark phase).

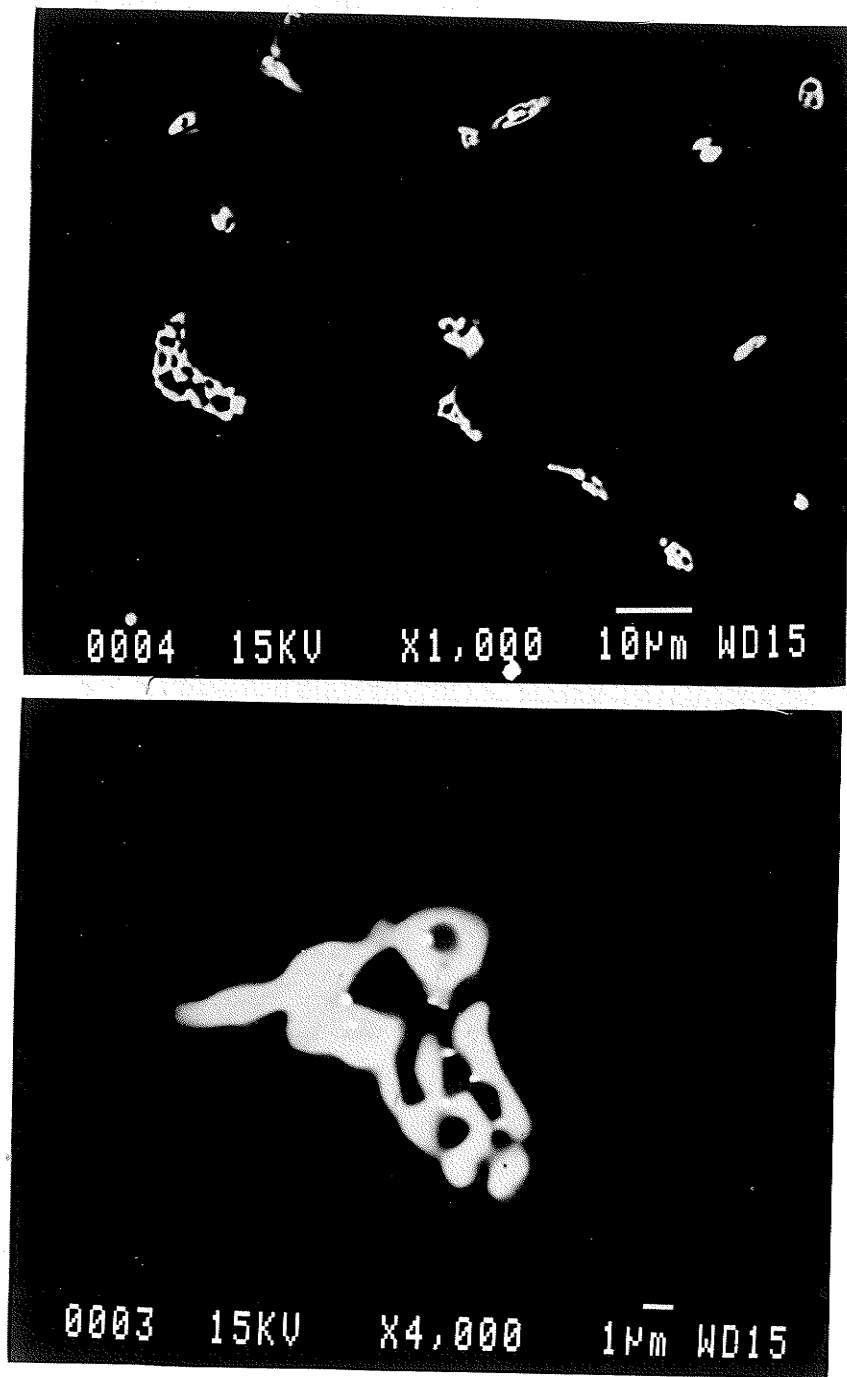


Figure 4-24: Microstructure of high gravity ingot. Larger interlamellar spacing for eutectic particles is evident.

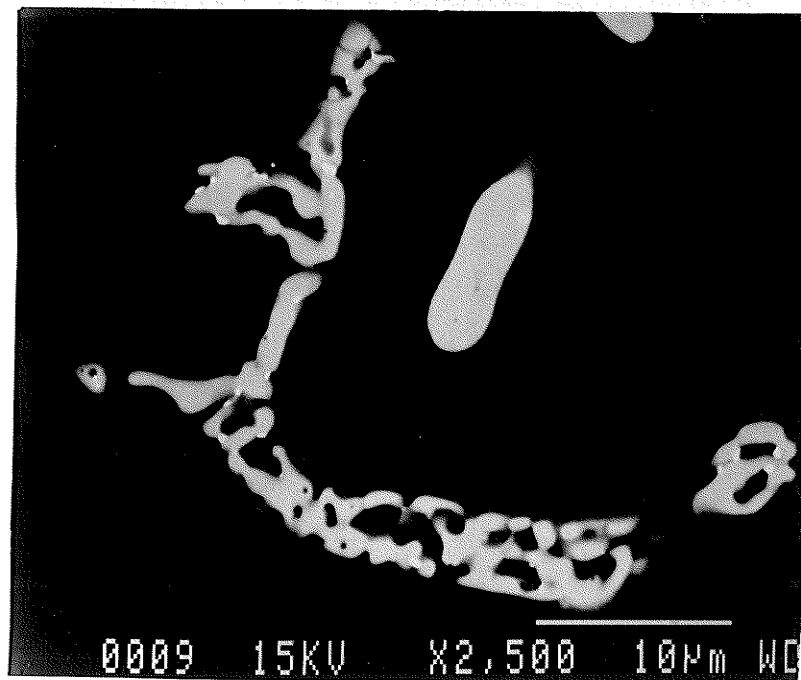
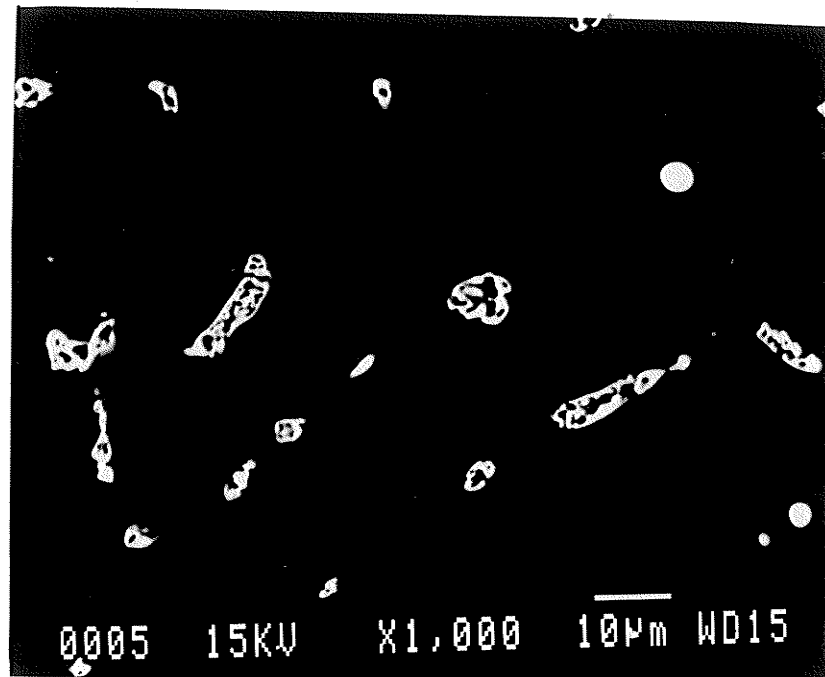


Figure 4-25: Microstructure of zero gravity ingot. Large interlamellar spacing in eutectic particles and some noneutectic  $\theta$  phase is evident.

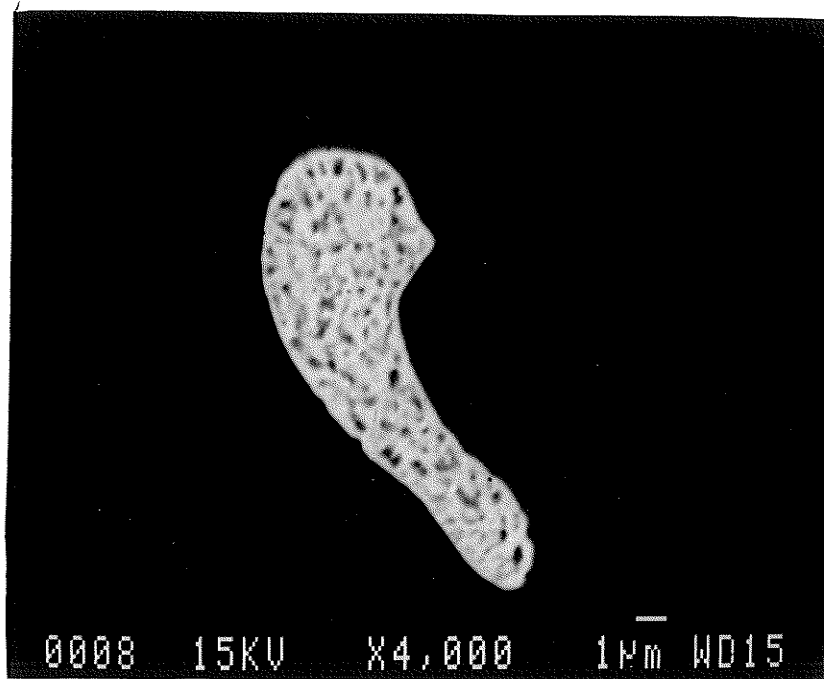


Figure 4-26: Eutectic particles with fine lamellar spacings in zero gravity ingot. Only a few percent of eutectic particles with fine spacing are present in this ingot.

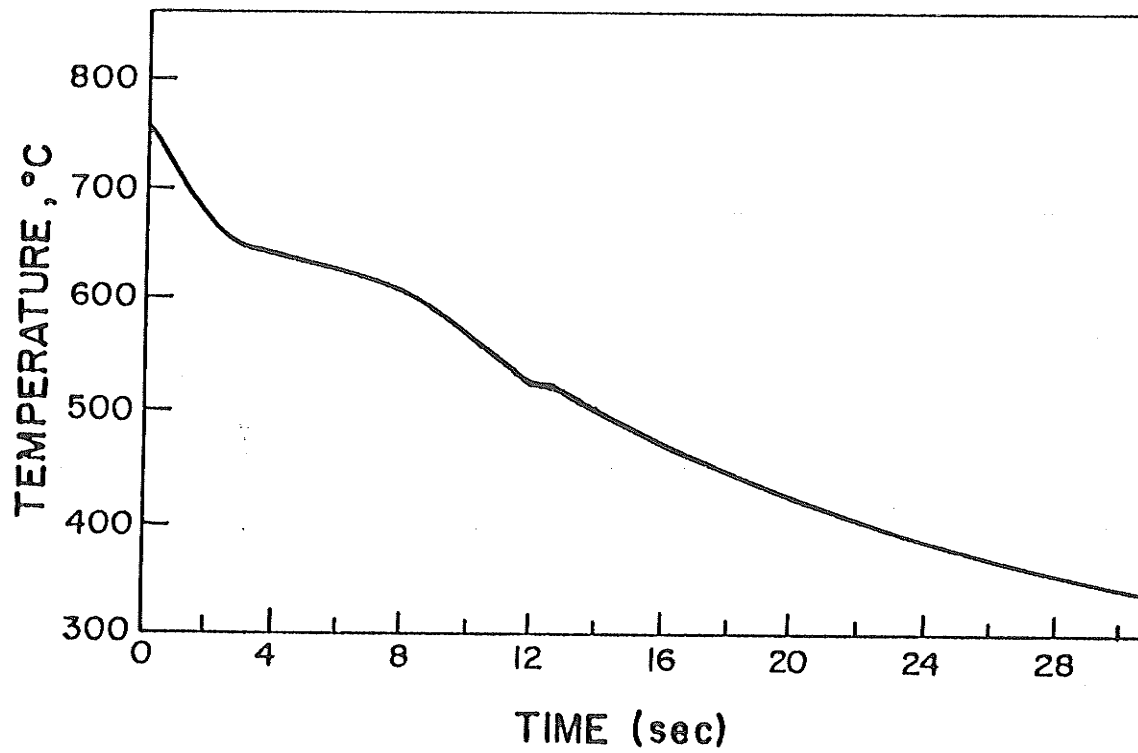


Figure 4-27: Cooling curve of KC-135 sample solidified in unit gravity.

Microstructure examination by SEM of the sample solidified in unit gravity (Figures 4-23 (a) and (b)), showed eutectic particles in the matrix of aluminium phase. In zero gravity and high gravity sample (Figures 4-24 and 4-25) the interphase spacing of eutectics are larger and some noneutectic  $\theta$  particles are evident. There were a few percent of eutectic particles with very fine interphase spacings in zero gravity sample as seen in Figure 4-26. Large amount of porosity and holes were present in all ingots.

#### 4-6-2 COOLING CURVE

A thermocouple was placed inside one of the samples solidified in unit gravity, to measure the temperature at a point half of the length from the chill face. Figure 4-27 gives the cooling curve recorded from this thermocouple.

The conditions for this test was kept the same as the ones during the flight. According to the curve solidification starts with the cooling rate of about  $7.4^{\circ}\text{K} / \text{sec}$ . Total solidification time was shown to be about 13 seconds.

#### 4-6-3 MACROSEGREGATION

The results of EDS analysis on three samples of Al-4%Cu solidified in Zero, 1.8 and unit gravity are illustrated in Table 4-8 and Figures 4-28, 4-29 and 4-30 respectively. The first two samples were solidified in KC-135 flight and the third one on ground.

Macrosegregation data in all three samples showed nearly uniform composition close to chill face up to about 1.5mm from the other end. A sudden increase in copper content close to the other end was also observed.



#### 4-6-4 MICROSEGREGATION

The Average of 2 scans on five dendrites was calculated for 0, 1.8 and 1 gravity samples (Table 4-9 and Figure 4-31). Calculations similar to the calculations for other AC samples were also carried out. Centre of the dendrite is considered to have the minimum copper content. Microsegregation data in all three samples shows the minimum copper content of about one percent.

Table 4-8: Macrosegregation data of KC-135 ingots.

Distance from chill face (mm)	Percent copper		
	0G	1G	1.8G
0-0.5	3.67±0.07	3.88±0.07	3.79±0.06
0.5-1	3.95±0.14	4.16±0.06	3.99±0.06
1-1.5	3.70±0.11	3.87±0.07	3.95±0.02
1.5-2	3.86±0.01	3.76±0.06	3.97±0.10
2-2.5	3.73±0.02	3.85±0.03	3.79±0.15
2.5-3	3.95±0.06	3.99±0.08	4.06±0.05
3-3.5	4.03±0.04	3.86±0.04	3.95±0.10
3.5-4	4.06±0.04	4.02±0.01	4.16±0.06
4-4.5	5.16±0.06	4.63±0.07	4.70±0.11
4.5-5	4.03±0.03	3.95±0.03	4.06±0.14

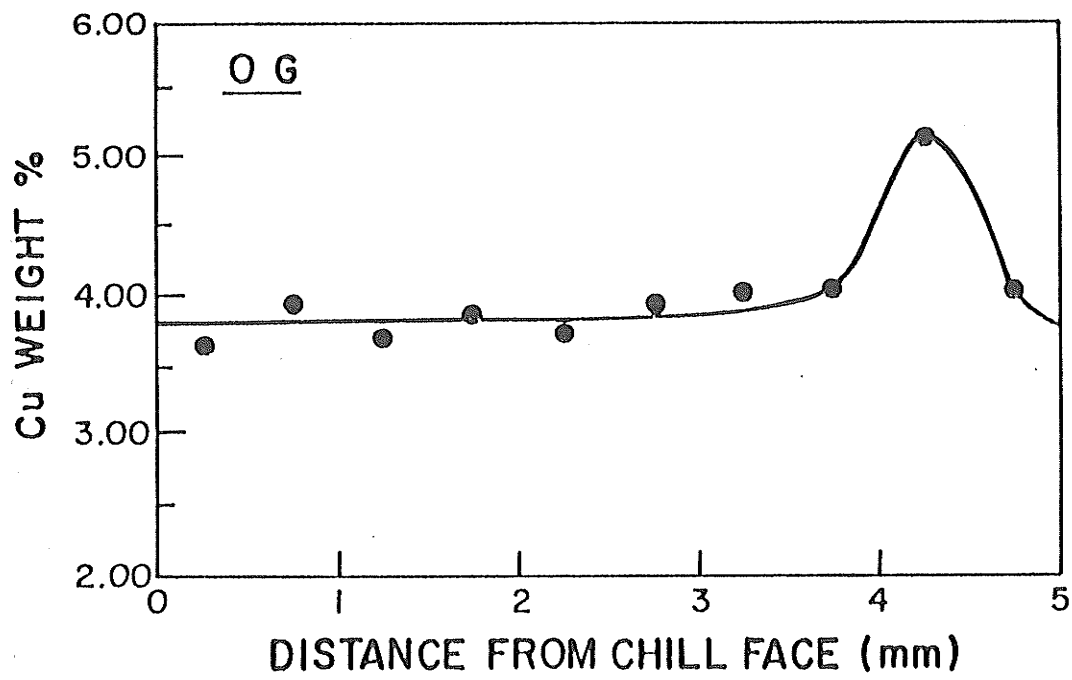


Figure 4-28: Macroseggregation in the ingot solidified in zero gravity.

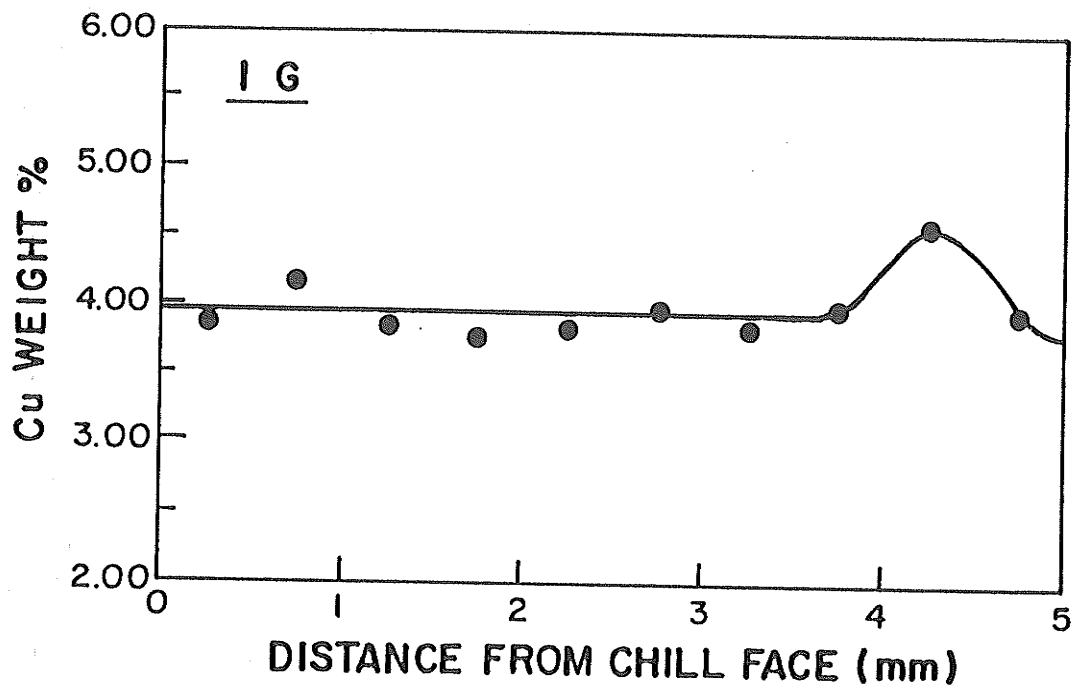


Figure 4-29: Macroseggregation in the ingot solidified in unit gravity.

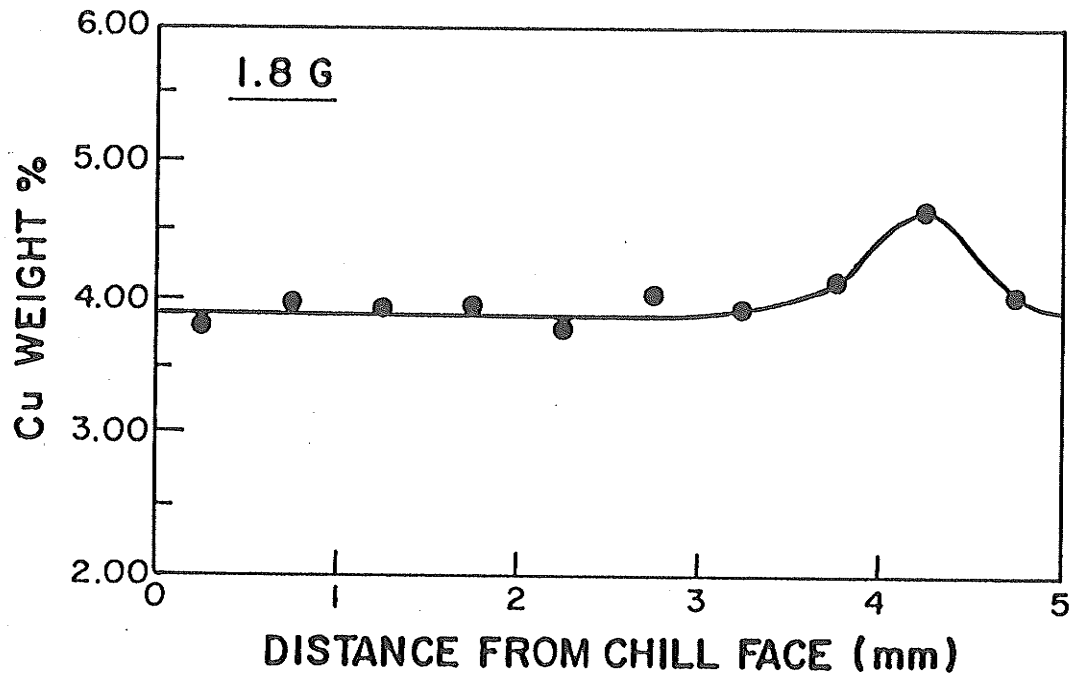


Figure 4-30: Macroseggregation in the ingot solidified in 1.8 times gravity.

Variation of gravity do not affect the microsegregation in these ingots, within the accuracy of analysis.

Table 4-9: Minimum composition of dendrites for KC-135 samples.

Sample	Average minimum composition (Percent copper)
0G	0.97±0.09
1G	1.19±0.10
1.8G	1.02±0.15

#### 4-6-5 DENDRITIC SPACINGS

The results of primary arm spacing measurements are summarised in Table 4-10. No difference in primary arm spacings was evident in the samples solidified in zero and 1.8 gravity. Table 4-11 illustrates the secondary arm spacings measured on longitudinal cross section of above samples.

Gravity did not affect the arm spacings in these samples solidified with a very fast cooling rate.

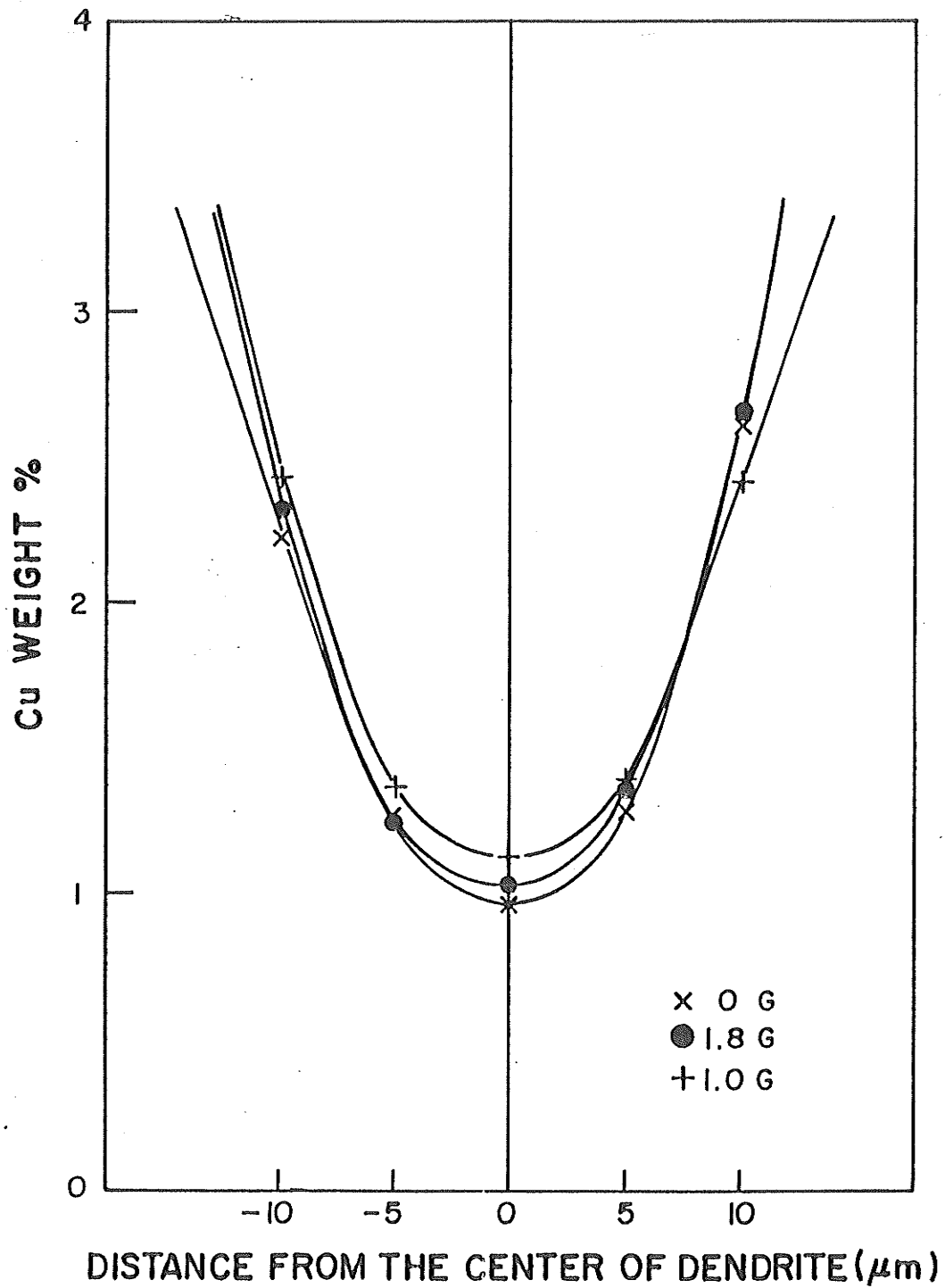


Figure 4-31: Microsegregation in the ingots solidified in zero, 1.8, and unit gravity.

Table 4-10: Primary arm spacings of KC-135 ingots.

Sample	Primary arm spacing ( $\mu\text{m}$ )
0G	$59.34 \pm 3.01^*$
1G	$75.66 \pm 1.87^*$
1.8G	$57.60 \pm 3.25^*$

\*95%CL

Table 4-11: Secondary arm spacings in KC-135 ingots.

Sample	Secondary arm spacing ( $\mu\text{m}$ )
0G	$22.54 \pm 0.54^*$
1G	$22.42 \pm 0.47^*$
1.8G	$24.17 \pm 1.60^*$

\*95%CL

## CHAPTER V

### DISCUSSION

#### 5-1 INVERSE SEGREGATION ALONG INGOTS

Inverse segregation of Al-4%Cu and Sn-15%Pb alloys have been theoretically calculated by a computer program [32] using equations (23)-(29) given in chapter II. The parameters for calculation of inverse segregation in the present ingots were taken from the cooling curves shown in Figures 4-7 and 4-8. According to the cooling curves, the dendrite tips reach the top of the ingot just as the base of the ingot is solidifying; i.e.  $L_1 = L_2 = R$  in Figure 2-10. The computer program for calculating segregation requires  $L_1 < L_2 < R$ , so the values were set at slightly less than the length of the ingot. The specific volume data for Al-4%Cu was taken from Ganesan and Poirier [55] and the phase diagram used was from Murray [56].

As illustrated in Figure 5-1, observed segregation agrees well with the theoretically calculated data for Al-4%Cu. However a similar comparison for Sn-15%Pb sample does not conform to inverse segregation, (Figure 5-2 (a) and (b) ), indicating the presence of gravitational segregation in these alloys. Mechanical mixing of such systems is essential for studying the effect of microgravity on macrosegregation and microstructure.

The observed chill face segregation of close to 0.4 percent also agrees well with the other experimental values summarised by Cahoon [27] in Figure 2-11, Chapter II.

No inverse segregation was observed in KC-135 samples within the accuracy of the analyses technique used. Macrosegregation is found to increase with decreasing cooling rates [35-37], The effect of cooling rate on segregation can be explained by comparing the magnitudes of velocities of interdendritic liquid to the magnitudes of the isotherm



velocities. With the slower cooling rate the magnitude of the velocity of the interdendritic liquid is less than that observed at a greater cooling rate, but relative to the velocity of the isotherms, there is substantially more flow at the slower cooling rate. Consequently, macrosegregation increases with decreasing cooling rate [37].

For faster cooling rates, inverse segregation occurs only near the extremities of the ingot with very little segregation in the middle portion [32]. For the small samples used in the KC-135 flights accurate analysis near the extremities is not possible and therefore the existence of any inverse segregation could go undetected.

In fact in high cooling rates the time available is not enough for solute flow to occur and compensate for the shrinkage. This can also be proved by the presence of porosity and holes in samples. In all three ingots solidified in zero, 1.8 and unit gravity, as it is shown in figure 5-3, shrinkage porosities can be observed.

The reason for the increase in concentration at the other end of the ingots is not clear, It may be explained by solute rejection at the liquid-solid interface which may cause a terminal transient zone at the end.

Comparison of the figures 4-11 and 4-13 shows that high gravity (up to 15G) had no significant effect on inverse segregation in Al-4%Cu ingots solidified at cooling rates of about 1°K/sec.

## 5-2 PARAMETERS AFFECTING MICROSEGREGATION

The numerical analysis technique described in section 2-2-1 (chapter II) and equations [13-15] were used to compute minimum copper content. The diffusion coefficient,  $D_{Cu}$ , was

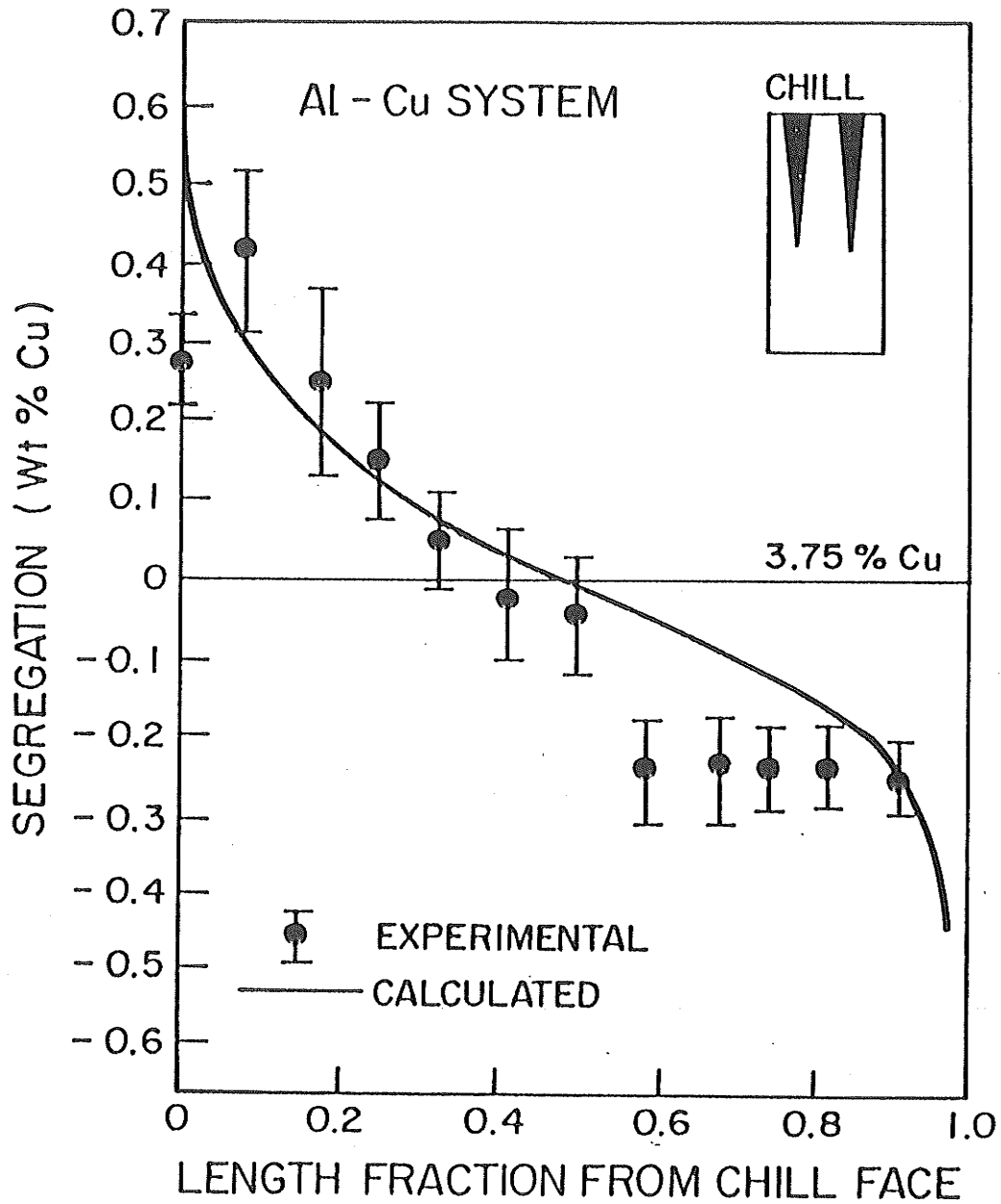
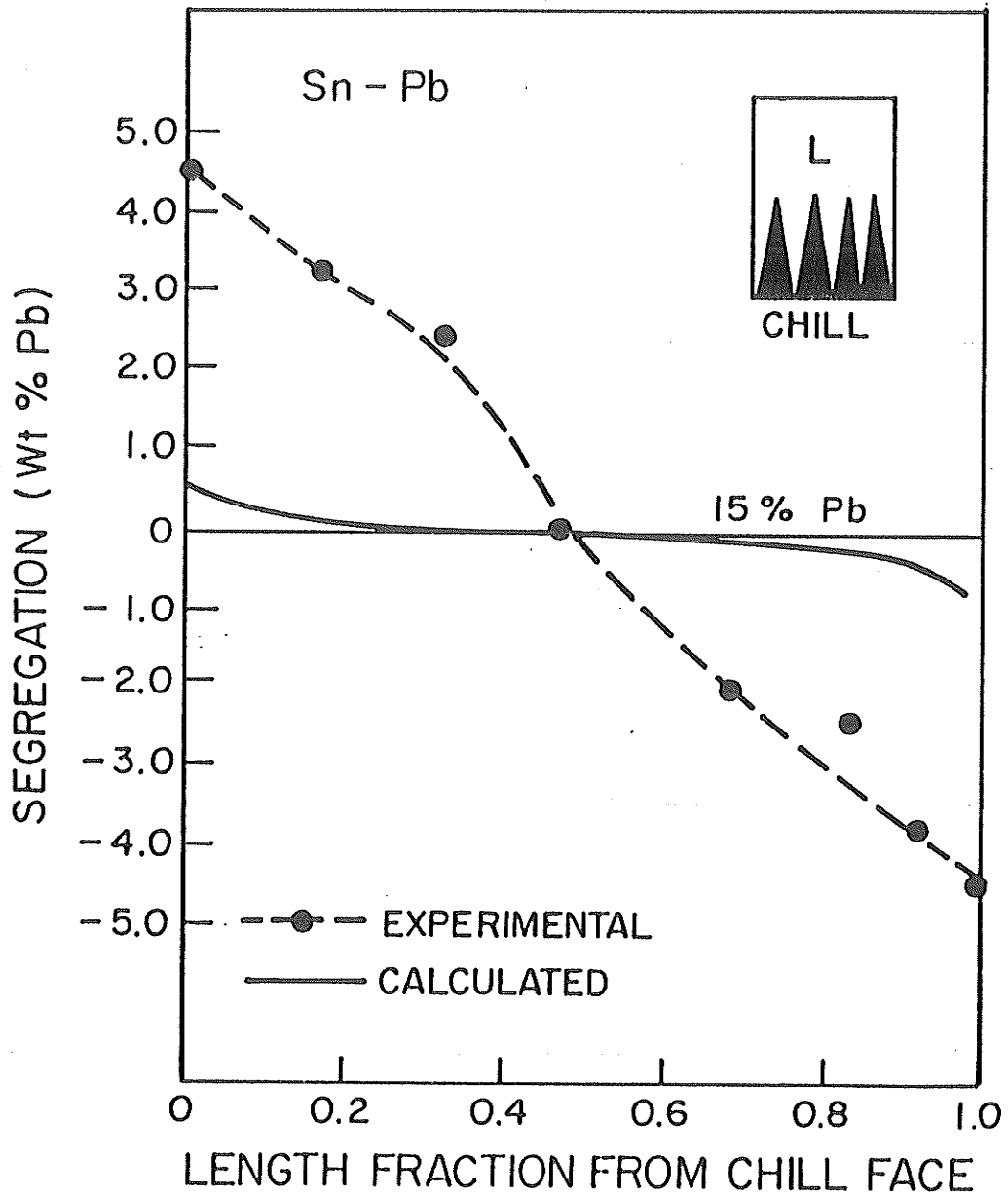
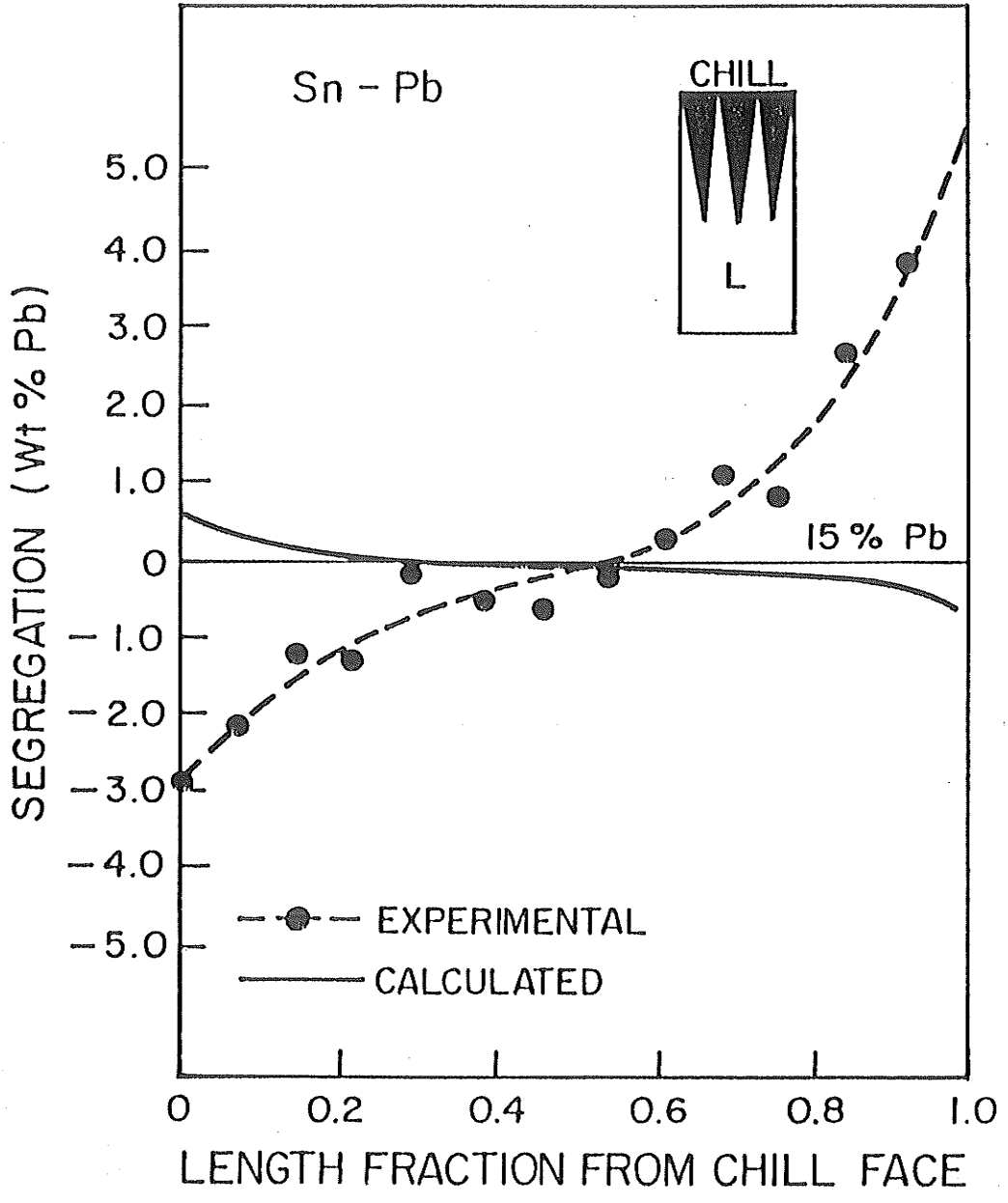


Figure 5-1: Observed inverse segregation in Al-4%Cu solidified parallel to gravity compared to theoretically calculated data.



(a)

Figure 5-2: observed segregation of Sn-15% Pb compared to theoretically calculated data. Sample solidified (a) opposite to gravity, (b) parallel to gravity.



(b)

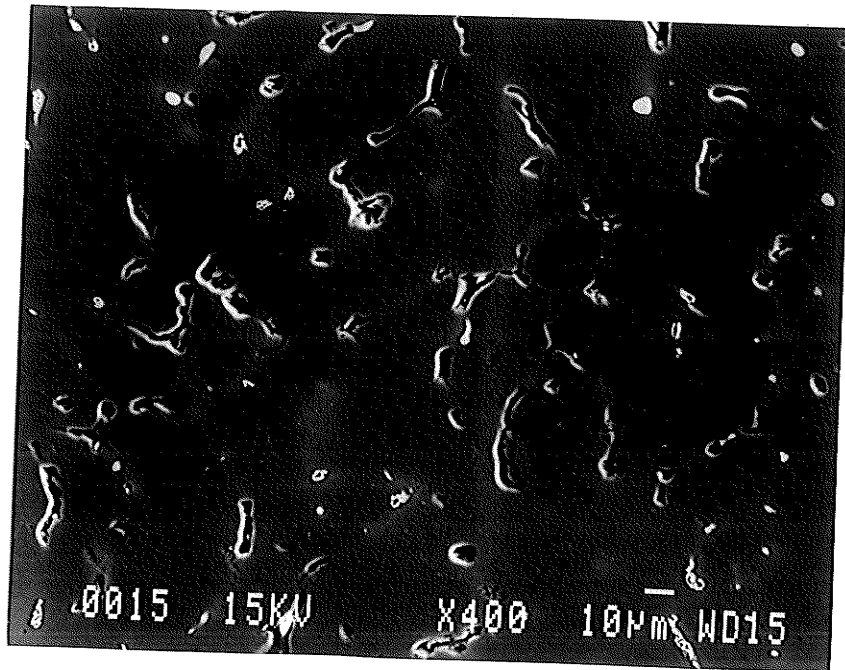


Figure 5-3: Porosity and holes caused by fast cooling

calculated at the mid-temperature between the liquidus and the eutectic temperature of the alloy (872° K) from the following equation [17]:

$$D_{Cu}=0.18 \exp\left(\frac{-30000}{RT}\right)$$

where R is the gas constant in cal./mole-° K and T is the temperature.

The variation of calculated solute content with the fraction of solid is shown in Figure 5-4. The copper content varies with the fraction of solid as follows:

$$\text{for AC-OG} \quad C_S=0.692 (1-0.9621f_S)^{-0.860}$$

$$\text{for AC-PG} \quad C_S=0.692 (1-0.9509f_S)^{-0.870}$$

$$\text{for AC-15G} \quad C_S=0.692 (1-0.9606f_S)^{-0.861}$$

$$\text{for KC-135-1G} \quad C_S=0.692 (1-0.9800f_S)^{-0.844}$$

A more accurate and complete description of solute redistribution is obtained by Brody and Flemings [15], using Fick's second law. As the alloy cools from the nonequilibrium solidus to room temperature, some homogenization occurs and the finite difference solution is extended to computation of the solid-state homogenization. Minimum copper content for Al-4.5%Cu. calculated as a function of:

$$\eta=\frac{4\theta_f}{\lambda^2}$$

by Brody and Flemings is shown in Figure 5-5 (where  $\theta_f$  is local solidification time and  $\lambda$  is dendrite spacing).

Assumptions in the analysis of solute redistribution are [15]:

- 1- negligible undercooling before nucleation of solid phase, or from kinetic or curvature effects;
- 2- no net flow of solute into or out of the "volume element", where the volume element is a small region, the order of a dendrite arm spacing,
- 3- complete diffusion in the liquid within the volume element;
- 4- a "Plate like" dendrite morphology.

Since growth morphology of the real dendrite is more complex than that assumed, as it is suggested by Bower et al [15], a correction factor should be applied to the dendrite arm spacing, such that

$$\lambda_c = g\lambda$$

where  $\lambda_c$  is "corrected dendrite arm spacing". Macrosegregation is then calculated using  $\eta_c$  in place of  $\eta$  where:

$$\eta_c = \frac{4\theta_f}{\lambda_c^2}$$

The correction factor used by Bower et al for all compositions and all solidification times is 0.32. Table 5-1 shows  $\eta_c$  values obtained by using the above correction factor. Minimum composition has been found from Figure 5-5, calculated by Brody and Flemings [15]. Comparison of the experimental and calculated values shows a good agreement.

All the experiments in the past have shown the solid content of more than  $kC_0$  and which is relatively constant over a wide range of cooling rates.

It should also be considered that, beside the diffusion in the solid during and after solidification, segregation can be influenced by mechanisms like: second phase reduction due to tip temperature depression, eutectic temperature depression, and supercooling prior to nucleation.

The minimum concentration of copper in the Al-4% Cu ingots was about 1.6%. This indicates an effective distribution coefficient,  $k_e$ , of about 0.4 or a concentration of 10% copper in the liquid at the solid-liquid interface. This is in agreement with the calculation of Cahoon [27] who suggested similar values of  $k_e$  for solidification of Al-Cu alloys.

Table 5-1 Microsegregation, comparison of experimental and calculated values.

Sample	Minimum composition (experimental) Copper percent	Secondary arm spacing ( $\mu\text{m}$ )	$\eta_c$ (sec./cm <sup>2</sup> )	Minimum composition (calculated)
AC-OG	1.59±0.25	36	2.10×10 <sup>8</sup>	1.4
AC-PG	1.69±0.18	30	3.04×10 <sup>8</sup>	1.6
AC-15G	1.62±0.22	42	2.21×10 <sup>8</sup>	1.45
KC-135-0G	0.97±0.09	22	---	---
KC-135-1G	1.19±0.10	22	1.05×10 <sup>8</sup>	1.05
KC-135-1.8G	1.02±0.15	24	---	---

The change in gravity level did not influenced the microsegregation. Experiments on superalloy PWA-1480 single crystals, [61], also indicates similar results.



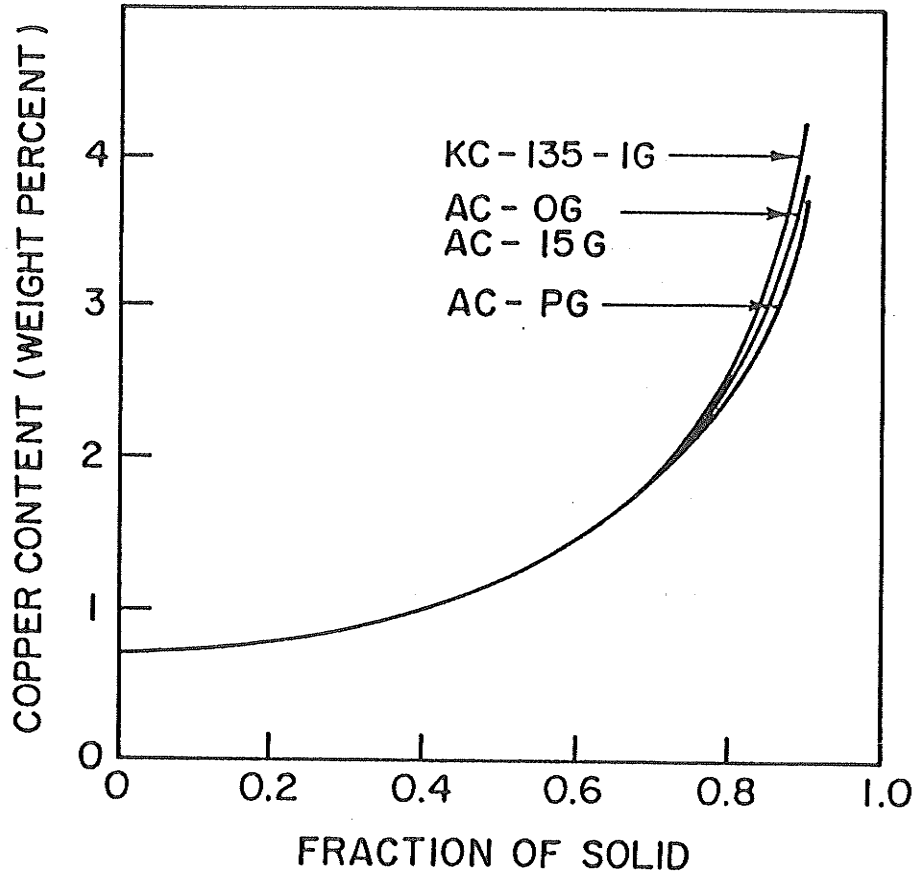


Figure 5-4: Variation of calculated solute content with fraction of solid.

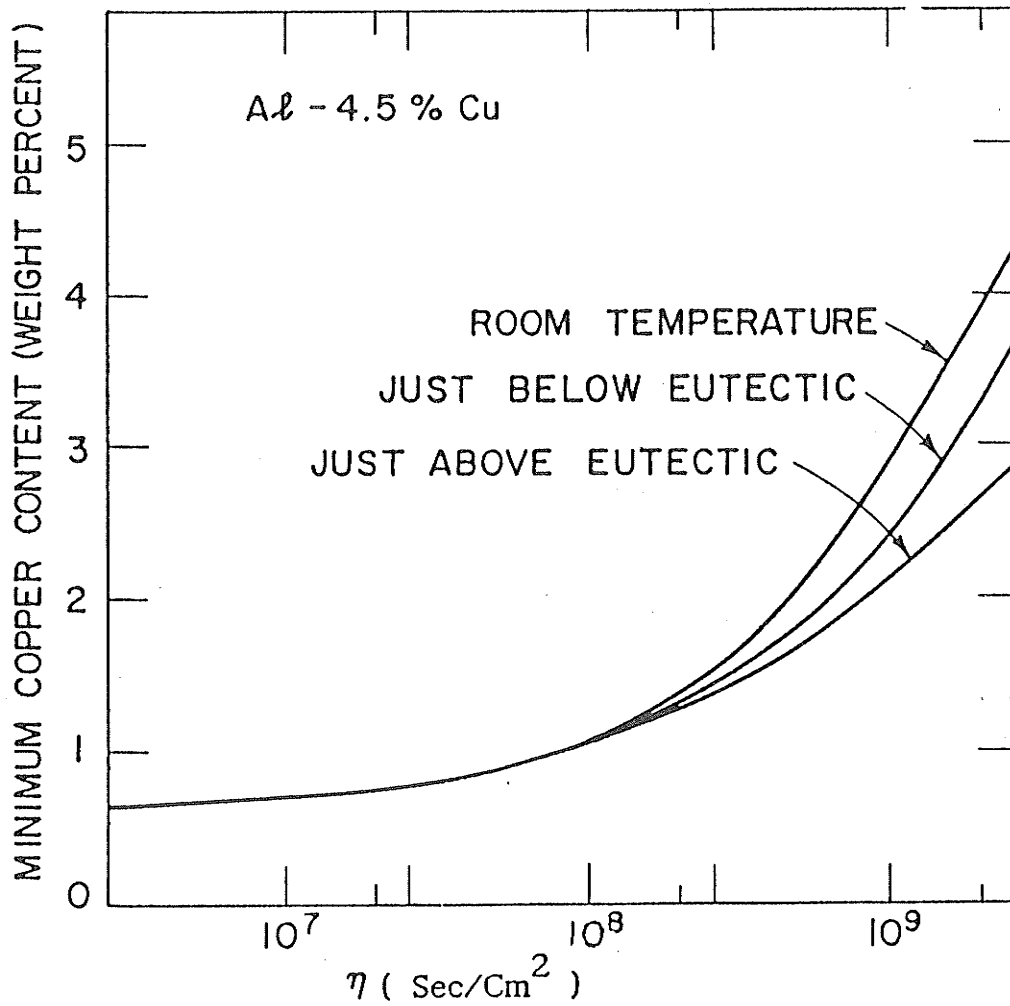


Figure 5-5: The minimum solute content of the solid phase calculated as a function of  $\eta$  for an Al-4.5% Cu alloy cooled to just above the eutectic, to just below the eutectic, and to room temperature. Finite difference method [15].

### 5-3 THE EFFECT OF GRAVITY ON DENDRITIC ARM SPACINGS

The primary arm spacings for AC-OG, AC-PG and AC-15G ingots were calculated by using empirical formula of  $\lambda = kG_L^a R^{-b}$  (equation 37, Chapter II). The constants evaluated by Young and Kirkwood [48] for Al-4.4%Cu ( $a=0.5$ ,  $b=0.36$  and  $k=3.05 \times 10^3$ ) were used for calculation. Table 5-2 shows experimental results as well as the calculated values.

The secondary arm spacings were calculated by using the equation  $\lambda_2 = \text{const. } \theta_f^{-0.39}$  as suggested by Bower et al [15] and Figure 2-19 in Chapter II. Solidification times have been measured from cooling curves. For AC-OG and AC-PG ingots solidification time was approximately 70 seconds, for AC-15G about 100, and for KC-135-1G about 13 seconds.

In all cases the experimental values of secondary arm spacings are very close to the calculated values. Comparison between experimental and calculated values of primary arm spacing gives similar results for AC-OG and AC-PG ingots. However for AC-15G sample, the calculated value is much higher.

Results of the experiments on ammonium chloride metal-model solution, [57], predicts steeper temperature gradient as the gravity reduces. This also agrees with the results in this work. The high gravity ingot shows lower temperature gradient (2.40°K/mm) as compared to the unit gravity samples (3.50 and 3.80 °K/mm, Table 4-1). Since the primary spacings are inversely proportional to temperature gradient and growth rate, one would expect the primary arm spacings to increase along with the gravity force. The experimental results contradict this and suggest that the theories do not consider all of the parameters that determine primary spacings.

As gravity increases, the convective flow of interdendritic fluid becomes more significant, thus concentration gradient, which causes coarsening, decreases. This produces slower coarsening rates and therefore, smaller spacing in high gravity.

As Klaren et al pointed out in their experiments [50], in lead-tin system the tin which is being rejected in solidification front is lighter than the bulk liquid and since the specimens were frozen vertically upwards this means that the density of the interdendritic liquid increases in the vertical direction. Therefore as it is also mentioned by Mc Cartney and Hunt [49] it seems possible that in these experiments convection currents occur in the liquid, that interact with the solute diffusion process and affect the dendrite spacings. As a result there should be agreement between their results and those obtained in alloys like Al-Cu in which a denser solute is being rejected at the interface. However as the growth velocity is increased, convection becomes less important in transporting solute, and as was shown by Klaren et al [50] there is a critical velocity below which the spacing becomes independent of velocity and at this stage convection becomes the dominant mass transfer mechanism. The fact that the influence of convection decreases by increasing velocity is also shown by Tensi [58] for Al-Si alloys.

In the experiments on ammonium chloride-water system, Burden and Hunt [59] have shown that ammonium chloride dendrite grown in the direction parallel to the gravity vector had a much coarser spacing than those grown in the direction opposite to the gravity vector. Similar experiment on Al-4%Cu in this work does not show any difference. This could be due to the fact that convection has less effect on solute transportation in higher growth velocities.

Table 5-2 Comparison of primary and secondary arm spacings.

Sample	Cooling rate (°K/sec.)	Primary arm spacing(μm)		Secondary arm spacing(μm)	
		Experimental	Calculated	Experimental	Calculated
AC-OG	1.16	194.71±7.52	187.99	36.51±1.61	≈30
AC-PG	1.10	196.56±11.81	202.12	30.54±1.50	≈30
AC-15G	0.80	168.61±5.27	244.08	42.90±2.49	≈40
KC-135-0G	---	59.34±3.01	---	22.54±0.54	---
KC-135-1G	7.40	75.66±1.87	---	22.42±0.47	≈20
KC-135- 1.8G	---	57.60±3.25	---	24.17±1.60	---

#### 5-4 VARIATION OF INTERLAMELLAR SPACING OF EUTECTIC PHASE

As mentioned in sections 4-1 and 4-6-1 the interphase spacing of eutectics has been found to be larger in high gravity as well as zero gravity samples as compared to unit gravity ingot. Interphase spacing is determined by the interaction of two opposing free energy considerations. One is that the transverse transfer of solute must occur over greater distances for thicker lamellae, and therefore a larger driving force is required. The other is that the free energy associated with the presence of the interphase boundaries increases as the lamellar width decreases [3]. Interphase spacing is also inversely proportional to the degree of undercooling.

In high gravity, Convective mixing can accelerate the solute transfer, and also it decreases the composition gradients at the interface and thus decreases supercooling. As a result the interphase spacing increases. On the other hand, as mentioned in section 2-3-1, experiments on Al -Cu and Al-Si alloys show that the thickness of diffusion layer in microgravity sample is much more than twice the layer thickness of the unit gravity experiment [45]. However in unit gravity, convective mixing will accelerate the solute transfer but it decreases the diffusion layer. As a result, combination of these two effects seems to decrease the interphase spacing of eutectic particles.

There is also a relationship between the growth rate of solid and interphase spacing and undercooling. By considering the solute diffusion between the periodic arrangement of lamellar, and the equilibrium of the surface forces at the three phase junction, a calculation of the undercooling,  $\Delta T_{E,C}$ , of the eutectic front as well as of the interphase spacing,  $\lambda$ , as a function of the growth rate,  $R$ , has been done and the following well known relationships have been obtained.

$$\lambda^2 R = \frac{K_r}{K_c}$$

$$(\Delta T_{E,C})^2 R = \frac{1}{4K_c K_r}$$

where the constants,  $K_c$  and  $K_r$  can be calculated from the properties of the alloy and arise from the solute diffusion and capillarity calculations respectively [58].

Since there is no data available from cooling characteristics of KC-135 samples, increase in interlamellar spacing might be because of difference in the growth rate of ingots solidified on the flight and on the ground. As it can be noted in table 5-2 the primary arm spacing of the ground sample has been found to be larger than the other two, as a result the cooling rates might be different.

Further experiments on hypo- and hyper-eutectic compositions as well as eutectic composition are necessary to investigate the effect of gravity on interphase spacings. This work is currently being done as an independent project.

## CHAPTER VI

### CONCLUSIONS

1- A good directional solidification of ingots is possible with the apparatus made and it can be used to study the segregation and microstructure of binary alloys in low gravity.

2- The experimentally observed data for the Al-4%Cu system agrees well with theoretically calculated macrosegregation. Such agreement, however, is not evident in Sn-15%Pb and Pb-15%Sn alloys. For the Tin-Lead and Lead-Tin systems, which tend to segregate due to gravity, evaluating inverse segregation and other microstructural parameters will be difficult unless these alloys are melted and solidified in microgravity to study the influence of convection on macrosegregation and microstructure.

3 -Changing the direction of gravity or increasing gravity (up to 15 times) did not affect the inverse segregation in Al-4%Cu alloy solidified with the cooling rates close to  $1^{\circ}\text{K/sec}$ .

4- No inverse segregation was observed in KC-135 samples because of the high cooling rate and the size of the samples.

5- Microsegregation of copper across dendrites in Al-4%Cu alloy did not change by changing the direction of gravity, decreasing or increasing gravity.

6- A good agreement exists between the experimentally observed and theoretically calculated microsegregation data for both AC and KC-135 samples, provided that the correction factor of 0.32 is used for dendrite arm spacing.

7- Primary dendrite arm spacing decreased by increasing the gravity, but changing the direction of gravity did not affect the dendrite arm spacings.



8- Primary and secondary arm spacings data obtained agrees well with the theoretical and experimental work in the past.

9- In both high gravity and low gravity experiments increase in lamellar spacing of eutectic phase has been observed which might be explained by increase in the thickness of diffusion layer in solid-liquid interface in low gravity; and solute transfer because of convection in high gravity.

## REFERENCES

1. Metals Handbook: 9th Edition, Vol. 15, American Society for metals, Metal Park, Ohio, (1988), pp. 101-158
2. I. Minkoff: Solidification and Cast Structure, John Wiley and Sons, New York, (1986).
3. Bruce Chalmers: Principles of Solidification, John Wiley and Sons Inc., New York, (1964).
4. Merton C. Flemings: Solidification Processing, Mc Graw Hill Inc., New York, (1974).
5. W.C. Winegard: An Introduction to the solidification of metals, Institute of Metals, London, (1964).
6. E. Scheil: Metallforschung, (1947), Vol.2, pp. 69-75.
7. R. Trivedi: Acta. Met., (1970), Vol 18, pp.287-296.
8. M.E. Glicksman, R.J. Schaefer, and J.D. Ayers: Metall. Trans., (1976), Vol. 7A, pp. 1747-1759.
9. S.C. Huang and M.E. Glicksman: Acta. Met. (1981), Vol. 29, pp. 701-715.
10. S.C. Huang and M.E. Glicksman: Acta. Met. (1981), Vol. 29, pp. 717-734.
11. W. Kurz and D. J. Fisher: Acta. Met., (1981), Vol. 29, pp. 11-20.
12. V. Laxmanan: Acta. Met., (1985), Vol 33, No. 6, pp. 1023-1035.
13. V. Laxmanan: Acta. Met., (1985), Vol.33, No. 6, pp. 1037-1045.
14. M.H. Burden and J.D. Hunt: J. Cryst. Growth, (1981), Vol. 22, pp. 109-116.
15. Harold D. Brody and Merton C. Flemings: Trans. AIME., (1966), Vol.236, pp.615-624.

16. T.F. Bower, A.D. Brody , and M.C. Flemings: Trans. AIME, (1966). Vol. 236, pp. 624-634.
17. T.W. Clyne and W. Kurz: Metall. Trans. A, (1981), Vol. 12A, pp.965-971.
18. J.A. Sarreal and G.J. Abbaschian: Metall. Trans. A, (1986), Vol. 17A, pp.2063-2073.
19. B. Giovanola and W. Kurz: Metall. Trans. A., (1990), Vol.21A. pp.260-263.
20. D.J. Allen and J.D. Hunt: Metall. Trans. A, (1979), Vol. 10A, pp. 1389-1397.
21. J. A. Burton, R. C. Brim, and W. P. Schlichter: J. Chem. Phy. (1953), Vol. 21, pp. 1987-1996.
22. J.S. Kirkaldy and W.V. Youdelis: Trans. AIME, (1958), Vol. 212, pp. 833-840.
23. W.V. Youdelis, J.V. Mac Ewan, and J.S. Krikaldy: Physical Chemistry of Process Metallurgy, (1961), Vol 8. Part 2, Interscience Publishers, New York and London, pp. 865-890.
24. M.C. Flemings and G.E. Nereo: Trans. TMS. AIME, (1967), Vol. 239, pp. 1449-1461.
25. W.V. Youdelis: Department of Mechanical Engineering, University of Windsor, Windsor, Ontario, Canada, Private Communication, (1972)
26. W. V. Youdelis, D. R. Colton: Trans. TMS-AIME, 1960, Vol. 218, pp. 628-631.
27. J.R. Cahoon, A Re-evaluation of inverse segregation in Al-Cu system, submitted for publication.
28. H. Kato and J.R. Cahoon: Metall Trans. A., (1985), Vol. 16A, pp. 579-587.
29. M.C. Flemings, R. Mehrabian, and G.E. Nereo: Trans. TMS-AIME, (1968), Vol. 242, pp.41-49.
30. M.C. Flemings and G.E. Nereo: Trans. TMS.AIME, (1968), Vol.242, pp. 50-55.

31. J.R. Cahoon and W. V. Youdelis: Trans. TMS.AIME, (1968), Vol. 242, pp. 757-759.
32. J.R. Cahoon and W.V. Youdelis: Trans TMS.AIME, (1964), Vol. 230, pp.1734.
33. N. Streat and F. Weinberg: Metall. Trans., 1974, Vol. 5, pp. 2539-2548.
34. L. Wand, V. Laxmanan and J.F. Wallace: Metall. Trans. A, (1988), Vol. 19A, pp.2687-2694.
35. R. Mehrabian, M. Keane and M.C. Flemings: Metall. Trans. (1970), Vol.1, pp. 1209-1220.
36. M.Simpson and M.C. Flemings: Metall. Trans., (1984), Vol. 15A, pp. 2095-2097.
37. A.L. Maples and D.R. Poirier: Metall. Trans. B, (1984), Vol. 15B, pp.163-172.
38. R.Jaanson and P.R. Sahn: Material Science and Engineering, (1984), Vol. 65, pp. 199-212
39. P.A. Curreri, D.M. Stefanescu and J.C. Hendrix: Directional solidification of flakes and nodular cast iron during KC-135 Low G Manoeuvres.
40. Heinz J. Sprenger: Proc. 6th European symposium on material science under microgravity conditions, Bordeaux, France, 2-5 December (1986)
41. B.K. Dhindaw, D.M. Stefanescu, A.K. Singh and P.A. Curreri: Metall. Trans. (1988), Vol. 19A, pp. 2839-2846.
42. S. Shah, R.N. Grugel, and B.D. Lichter: Metall. Trans. (1988), Vol. 19A, pp. 2677-2680.
43. F. Barlieri and C. Patuelli: Metall. Trans., (1988), Vol. 19A, pp.2659-2664.
44. Paul Pant; Fundamental studies on the Manganese-Bismuth system in microgravity, Proc. 6th European Symposium on material science under microgravity conditions, Bordeaux, France, 2-5 December (1986).

45. J.J. Favier, J. Berthier, Ph. Arragon, Y. Malmejac, V.T. Khryapov and I.V. Barmin: *Acta. Astranamica*, (1982), Vol. 9, No. 4, pp.255-259.
46. Hans. M. Tensi and Joachim J. Schmidt; *Mat. Res. Soc. symp. Proc.* , Vol. 87, (1967), Material Research society.
47. S.C. Huang and M. E. Glicksman: *Acta. Met.*, (1981). Vol. 29, pp. 717-734.
48. T.Z. Kattamis, J.C. Coughlin, and M. C. Flemings: *Trans. TMS.AIME*, (1967), Vol. 239. pp. 1504-1511.
49. K.P. Young and D.H. Kirkwood: *Metall. Trans.*, (1975). Vol. 6A, pp. 197-205.
50. D.G. Mc.Cartney and J.D. Hunt: *Acta. Met.*, (1981), Vol. 29, pp.1851-1863.
51. C.M. Klaren, J.D. Verhoeven: *Metall. Trans. A*, (1980), Vol. 11A, pp. 1853-1861.
52. P.A. Curreri, J.E. Lee and D.M. Stefanescu: *Metall. Trans. A*, (1988), Vol. 19A, pp. 2671-2676.
53. M.H. Mc.Cay, J.E. Lee and P.A. Curreri: *Metall. Trans.* (1986), Vol. 17A, pp.2301-2303.
54. M.H. Johnston, P.A. Curreri, R.A. Parr, and W.S. Alter: *Metall. Trans.*, (1985), Vol. 16A, pp.1683-1687.
55. G.F. Vander Voort: *Metallography, Principles and Practice* , Mc Graw Hill, 1984.
56. M. Rappaz: *International Materials Reviews*, (1989), Vol. 34, No. 3, pp. 93-123.
57. J.L. Murray: *International Metals Review*, (1985), Vol.30, pp. 211-233.
58. M.H. Johnston and R.B. Owen: *Metall. Trans.A*, (1983), Vol. 14A, pp. 2163-2167.
59. Hans M. Tensi: *Metall. Trans. A*, (1988), Vol.19A, pp. 2681-2686.
60. M.H. Burden and J.D. Hunt: *Metal. Sci.*, (1976), Vol. 10, pp.156
61. M. Vijayakumar, S.N. Tewari, J.E. Lee and P.A. Curreri, (1990), *CSME Mechanical Engineering Forum*.